Recoil Polarimetery in Meson Photoproduction Reactions

Mark Sikora

School of Physics and Astronomony

The University of Edinburgh

A thesis submitted for the degree of

Doctor of Philosophy

2011

For Dina.

Acknowledgements

I would like to thank my supervisor, Dan Watts, for giving me the opportunity to work on such a unique and interesting experiment and for his excellent guidance over the duration of my PhD. I am also indebted to Derek Glazier for all of his assistance with the analysis and from whom I learned much about programming.

I would like to express my gratitude to all of the students and post-docs in the Edinburgh Nuclear Physics Group for creating an enjoyable work environment. In particular, I want to thank the other students I have worked with as part of the photonuclear group, Daria Sokhan, Tom Jude, Jo McAndrew, and Pauline Hall-Barrientos, for all of the enjoyable experiences while working at Mainz and attending conferences.

I am grateful to the entire A2 collaboration and the MAMI staff for running the experiment and performing detector calibrations. I would like to thank my colleagues from the University of Glasgow, Ken Livingston, John Annand, David Hamilton, Jamie Robinson, Joe Mancell, and the Burger, for their support over the past four years.

A special thanks is due to Jane Patterson for her invaluable administrative assistance throughout my PhD. Her timely and effective support was always much appreciated.

I want to thank my family for always encouraging me. I could not have done this without the love and patience of my wife Dina, whose reassurances during stressful times have sustained me.

Abstract

A large acceptance polarimeter has been designed to measure recoil polarisation in pseudoscalar (J^{π}=0^{-}) meson photoproduction reactions. The device was installed at the MAMI facility at the Institut für Kernphysik in Mainz, Germany. A racetrack microtron provided a longitudinally polarised 1.5 GeV electron beam, which impinged on a 12 μm copper radiator, producing a beam of circularly polarised Bremsstrahlung photons with energies between 400-1400 MeV. The electrons were then momentum analysed in the Glasgow Photon Tagging Spectrometer to tag the photon energy with a resolution of $\sim$4 MeV. The photons were incident on a liquid hydrogen target, and the reaction products were detected using the Crystal Ball and TAPS detectors. The beam-recoil polarisation observable C_x, which describes the fraction of circular polarisation transferred from the photon beam to the recoiling nucleon, was measured in the reactions γp$\rightarrow$pπ^0 and γp$\rightarrow$pη from data taken in September-October 2008. The results for π^0 production give a significant expansion of the world data set and are shown to be consistent with the few previous measurements taken at Jefferson Lab, USA, while the results for the η channel are a world first. The observed values for C_x are compared to the current solutions from the two leading partial wave analyses, SAID and MAID, with wide angular coverage up to a photon beam energy of 1400 MeV. Significant discrepancies in the prediction of C_x can be resolved by the new data.

Declaration

The data presented in this thesis were obtained in an experiment carried out by the CB@MAMI collaboration in the A2 hall of the Institüt fur Kernphysik at the University of Mainz, Germany. I played a major role in the preparation and execution of the experiment, and the data analysis and interpretation are entirely my own work. Any contributions from colleagues in the CB@MAMI collaboration, such as diagrams or calibrations, are explicitly referenced in the text. This thesis was written by myself, and the work presented in it has not been submitted in support of another degree or qualification from this or any other university or institute of learning.

Mark Sikora

Contents

List of Figures

Chapter 1

Introduction

In the Standard Model, the strong nuclear interaction is described by 6 elementary particles, known as quarks, which have 3 colour charge states. The colour force between quarks is mediated by the exchange of 8 (colour) charged gluons, which consequently experience self-interactions. All of the hadrons observed thus far are colourless bound states of 2 or 3 quarks (mesons and baryons, respectively). Quantum Chromodynamics (QCD) describes the interactions of the quarks and gluons as a quantum field theory.

Despite the success in formulating a theory of the strong force, most of the properties of hadrons cannot be computed from first principles. The force coupling in QCD is not constant, as is the case in electrodynamics, but increases asymptotically as the distance of the interaction increases. As a result, calculations using perturbation theory are not possible on the scale of mesons and baryons. This has led to the development of various models and novel computational methods to describe the internal landscape of hadrons.

Interest in understanding the structure of the proton and neutron (nucleons) is especially strong because of their central role in nuclear physics. Disappointingly, the nucleon excitation spectrum, a fundamental property arising from the dynamics of its constituents, is not accurately reproduced by existing models. Such models do not properly account for even the lowest lying isospin-1/2 state, known as the Roper resonance. Moreover, the excitation spectrum itself remains poorly determined experimentally, with the masses, widths, and even the existence of many states not well established. A world-wide program of experiments is being conducted to improve this situtation and provide additional constraints

for theoretical predictions.

Intense, polarised photon beams are used to excite the nucleon into a resonant state, which can then be studied via the subsequent decay to a nucleon-meson final state. In the case of pseudoscalar (J^{π}=0^{-}) meson production, the transition matrix is a sum of 4 complex production amplitudes which contain information on the excitation spectrum. Taking bilinear combinations of these production amplitudes results in 16 real polarisation observables, corresponding to measurement of beam, target, or recoil nucleon polarisation. Measuring these quantities provides crucial experimental input in reaction models which determine resonance charateristics using partial wave analysis.

This thesis presents measurements of the recoil polarisation observable C_x for the reactions $\gamma p \rightarrow p\pi^0$ and $\gamma p \rightarrow p\eta$ over a photon energy range of 400 MeV $< E_\gamma <$ 1400 MeV. Recoil polarisation observables are essential in order to fully constrain the reaction amplitudes, permitting a model independent analysis of contributing resonances. Previous measurements of C_x in π^0 production are limited to a handful of data points, and C_x has never before been measured in the η channel. These results will greatly expand the world data set and provide valuable new constraints, particularly for the poorly understood Roper resonance.

A new recoil polarimeter was installed for use with the Crystal Ball detector and the energy tagged polarised photon beam available at the MAMI facility. The nearly 4π angular coverage provided by this arrangement provides a unique opportunity to measure recoil polarisation observables simultaneously across a broad range of energies and angles.

The following chapter discusses the quark model and current theoretical approaches to nucleon spectroscopy. Chapter 3 describes in detail the process of pseudoscalar meson photoproduction and the extraction of resonance information using partial wave analysis. The experimental facility is outlined in Chapter 5, with information on detector calibration given in Chapter 6. The experimental analysis is given in Chapter 8, while the results for C_x are shown in Chapter 9. Chapter 10 concludes with a discussion of the results.

Chapter 2

QCD and the Nucleon

2.1 Development of QCD

2.1.1 The 'particle zoo'

Experimental work on the atomic nucleus was pioneered by Rutherford in the early 20th century. By analysing the scattering of alpha particles, he concluded that atoms contained a positively charged nucleus occupying a small fraction of the atomic volume. Further research [1] led him to discover that the nucleus is composed of protons, and Chadwick later showed the existence of neutrons [2]. Heisenberg noted that the small mass difference between the proton and neutron suggests they are two states of the same particle, the nucleon, and introduced the isospin quantum number **I** to identify the two nucleons in the framework of quantum mechanics [3]. This isospin doublet results from the algebra of the group[1] $SU(2)_I$ of 2×2 unitary matrices with determinant 1. The two dimensional representation of SU(2) describes a particle of spin-1/2 and is the simplest non-trivial representation (higher occupancy multiplets correspond to higher dimensional representations). The three generators of SU(2), labeled t_1, t_2, and t_3, derive from the Pauli matrices

$$t_1 = \tfrac{1}{2}\sigma_1 = \tfrac{1}{2}\begin{pmatrix} 0 & 1 \\ 1 & 0 \end{pmatrix}$$
$$t_2 = \tfrac{1}{2}\sigma_2 = \tfrac{1}{2}\begin{pmatrix} 0 & -i \\ i & 0 \end{pmatrix}$$

[1] See Appendix A for more details about group theory.

$$t_3 = \tfrac{1}{2}\sigma_3 = \tfrac{1}{2}\begin{pmatrix} 1 & 0 \\ 0 & 1 \end{pmatrix}$$

and satsify the commutation relations

$$[t_1,t_2] = it_3 \qquad [t_2,t_3] = it_1 \qquad [t_3,t_1] = it_2$$

States in isospin space are labeled by the eigenvalues of generators which can be diagonalised. In the fundamental representation, these are obtained from t_3 to be $I_3 = \pm\, 1/2$. The two states of the nucleon are represented by the basis vectors $\begin{pmatrix} 1 \\ 0 \end{pmatrix}$ $(I_3 = 1/2)$ for the proton and $\begin{pmatrix} 0 \\ 1 \end{pmatrix}$ $(I_3 = -1/2)$ for the neutron. Since this algebra is invariant under rotations in isospin space, isospin is a conserved quantity in strong interactions.

In 1935, Yukawa [4] described the strong force with a potential of the form

$$V(r) \sim g^2 \frac{e^{-\lambda r}}{r} \tag{2.1}$$

He predicted that this short ranged force would be quantised by a particle with approximately 200 times the mass of the electron, anticipating the existence of the pion 12 years before its discovery. The time scale for transitions due to the strong force can then be estimated using the uncertainty principle

$$\Delta t \sim \frac{\hbar}{mc^2} \sim 10^{-23} s \tag{2.2}$$

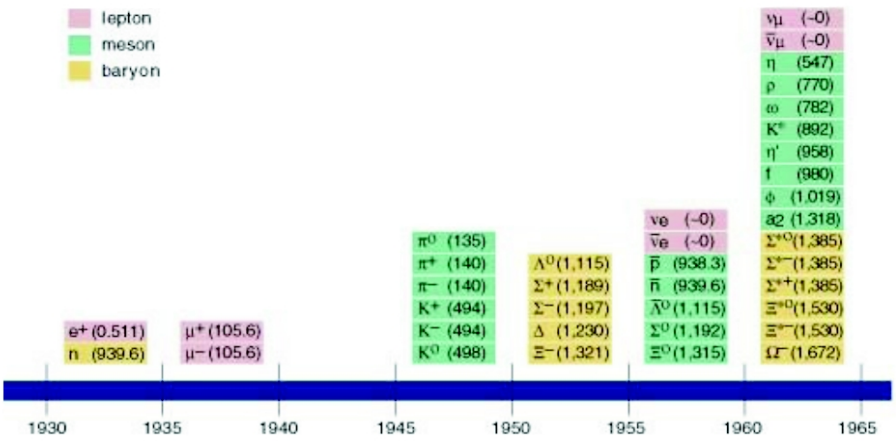

Figure 2.1: Expansion of the 'particle zoo'.

Throughout the 1940's and 1950's, experiments using cosmic rays and newly developed particle accelerators revealed a 'zoo' of new particles (Figure 2.1). A novel feature of many of these new particles was that their production rates were much greater than their decay rates, indicating that they are produced by the strong interaction but then decay weakly [5]. Building on the work of Pais [6], Gell-Mann [7] and Nishijima [8] independently proposed strangeness, S, as a new quantum number to account for this phenomenon which is conserved in strong interactions but not in weak processes. The quantum numbers for hadrons obey the Gell-Mann-Nishijima formula relating strangeness, isospin, baryon number (B), and electric charge (Q)

$$Q = I_3 + \frac{1}{2}(Y), \; Y = B + S \tag{2.3}$$

where the quantity of hypercharge, Y, has been introduced.

With this new degree of freedom, Gell-Mann [9] and Ne'eman each developed a classification scheme for the multitude of hadrons which the former termed the Eightfold Way. Using existing assignments of baryon number, spin, and isospin, the hadrons can be neatly arranged using S and Q. The B=0 pseudoscalar (J^π=0^-) and vector (J^π=1^-) mesons form nonets (Figure 2.2). Similarly, spin-1/2 and spin-3/2 baryons (B=1) form an octet and a decuplet (Figure 2.3).

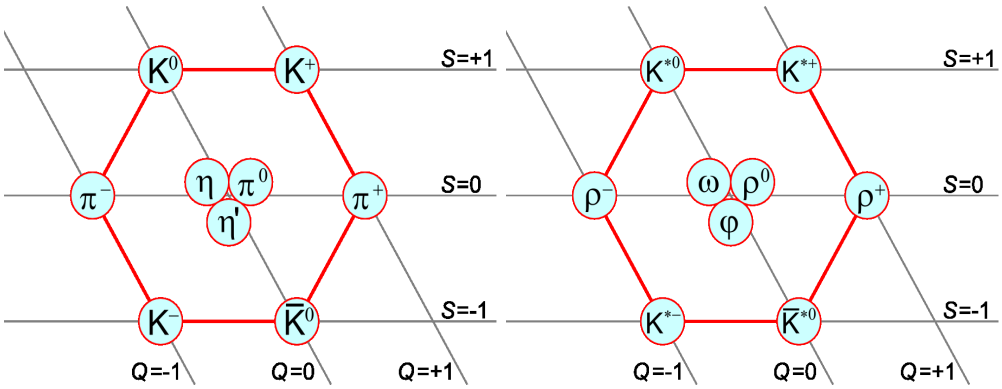

Figure 2.2: Pseudoscalar (left) and vector meson (right) multiplets in the Eightfold Way. Images from Wikimedia Commons.

Based on this classification scheme, Gell-Mann predicted the existence and the mass of the Ω^- baryon, the missing S=−3 state in the baryon decuplet. In 1964,

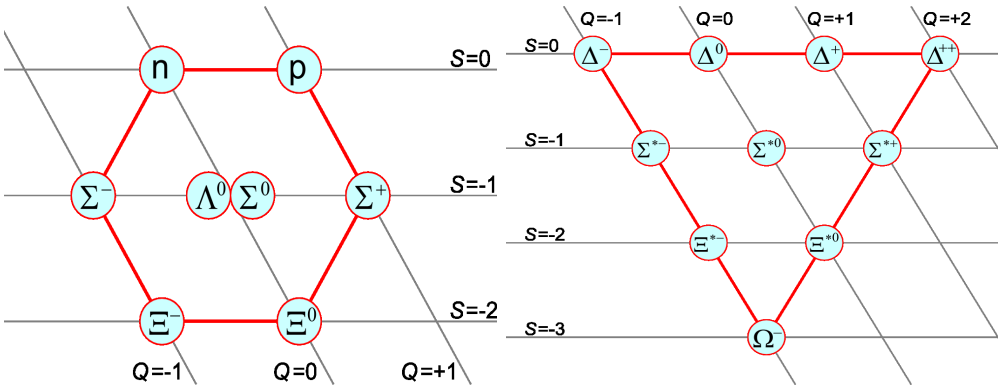

Figure 2.3: Octet of spin-1/2 baryons and decuplet of spin-3/2 baryons. Gell-Mann correctly predicted the existence of the Ω^- to complete the decuplet. Images from Wikimedia Commons.

an experiment at Brookhaven National Lab confirmed this prediction, providing compelling support for this apparent symmetry.

2.1.2 Flavour, Colour SU(3) Symmetry

The Eightfold Way is based on the group SU(3). Elements are generated from 8 matrices $t_i = \frac{1}{2}\lambda_i$, where λ_i are the Gell-Mann matrices

$$\lambda_1 = \begin{pmatrix} 0 & 1 & 0 \\ 1 & 0 & 0 \\ 0 & 0 & 0 \end{pmatrix} \quad \lambda_2 = \begin{pmatrix} 0 & -i & 0 \\ i & 0 & 0 \\ 0 & 0 & 0 \end{pmatrix} \quad \lambda_3 = \begin{pmatrix} 1 & 0 & 0 \\ 0 & -1 & 0 \\ 0 & 0 & 0 \end{pmatrix}$$

$$\lambda_4 = \begin{pmatrix} 0 & 0 & 1 \\ 0 & 0 & 0 \\ 1 & 0 & 0 \end{pmatrix} \quad \lambda_5 = \begin{pmatrix} 0 & 0 & -i \\ 0 & 0 & 0 \\ i & 0 & 0 \end{pmatrix} \quad \lambda_6 = \begin{pmatrix} 0 & 0 & 0 \\ 0 & 0 & 1 \\ 0 & 1 & 0 \end{pmatrix}$$

$$\lambda_7 = \begin{pmatrix} 0 & 0 & 0 \\ 0 & 0 & -i \\ 0 & i & 0 \end{pmatrix} \quad \lambda_8 = \frac{1}{\sqrt{3}} \begin{pmatrix} 1 & 0 & 0 \\ 0 & 1 & 0 \\ 0 & 0 & -2 \end{pmatrix}$$

which then satisfy a set of commutation relations. Note that the generators t_1, t_2, and t_3 are the three dimensional representations of the Pauli matrices. As in SU(2), where states are labeled by the eigenvalues of the diagonalisable $\sigma_3 = S_z$ Pauli matrix, states in SU(3) are labeled by the eigenvalues of the diagonalisable generators t_3 and t_8. This results in two quantum numbers for each state, the third component of isospin I_3 and hypercharge Y. In the fundamental representation, the basis vectors are

$$u = \begin{pmatrix} 1 \\ 0 \\ 0 \end{pmatrix} \qquad d = \begin{pmatrix} 0 \\ 1 \\ 0 \end{pmatrix} \qquad s = \begin{pmatrix} 0 \\ 0 \\ 1 \end{pmatrix}$$

These can be used to generate higher dimensional multiplets by taking direct products. To illustrate this process in a more familiar case, it is instructive to return to SU(2) and consider two spin-1/2 particles. These can be combined into a triplet of spin-1 configurations and a spin-0 singlet state. This is written as

$$\mathbf{2} \times \mathbf{2} = 3 + 1$$

All of the observed hadron multiplets are obtained from SU(3). The baryon multiplets result from the direct product $\mathbf{3} \times \mathbf{3} \times \mathbf{3}$, while the mesons combine as $\mathbf{3} \times \mathbf{3}^*$, where $\mathbf{3}^*$ denotes the complex conjugate of the fundamental representation. The identification of all the known baryons and mesons as higher dimensional representations of SU(3) implies that they are not elementary. In 1964 Gell-Mann [10] and Zweig independently postulated the existence of 3 'quarks' based on the dimension of the fundamental representation of SU(3). Baryons then are bound states of three quarks qqq while mesons are a quark-antiquark pair $q\bar{q}$. The quarks are labeled by *flavour*: up, down, and strange. Their properties are listed in Table 2.1

Flavour	Mass	Q	B	S	I	I_3	J^P
u	1.5-3.3 MeV/c^2	$\frac{2}{3}$e	1/3	0	1/2	+1/2	$\frac{1}{2}^+$
d	3.5-6.0 MeV/c^2	-$\frac{1}{3}$e	1/3	0	1/2	-1/2	$\frac{1}{2}^+$
s	80-130 MeV/c^2	-$\frac{1}{3}$e	1/3	-1	0	0	$\frac{1}{2}^+$

Table 2.1: Summary of quark quantum numbers.

It was not clear initially if quarks were real particles or just convenient mathematical constructs with no physical presence. That they were predicted to carry fractional electric charges was cited as evidence of the latter. However, data collected at SLAC in the late 1960's of deep inelastic electron-proton scattering [11] gave the first experimental evidence in support of the existence of quarks. The mathematical formulation of the scattering process includes two structure functions arising from the spatial extent of the proton. The observation that the structure functions do not vary much with the wavelength of the virtual photon exchanged in the scattering process was interpreted by Bjorken to indicate the

existence of charged, point-like scattering centers in the proton. Further analysis of inelastic scattering data revealed scaling violations in the structure functions that were much greater than could be accounted for by the electromagnetic interaction alone. This result indicated the presence of a strong interaction between quarks.

As spin-1/2 particles, quarks obey Fermi-Dirac statistics, which would prohibit baryon states like the spin- and flavour-symmetric sss (Ω^-). Consequently, Greenberg [12] introduced a new property of quarks known as colour which transforms under $SU(3)_C$, distinct from flavour $SU(3)_F$. Quarks then can have one of three colours: red, green, or blue (anti-red, anti-blue, or anti-green for anti-quarks). Each quark in a baryon has a unique colour assignment, leaving the baryon in an overall colour neutral (colour singlet) state. Similarly, mesons reside in the color singlet which results from the direct product $\mathbf{3} \times \mathbf{3}^*$ in $SU(3)_C$. All free particles are colour neutral, which leads to the conclusion that a free quark cannot be detected; quarks are always *confined* into colourless objects.

In contrast to $SU(3)_F$, $SU(3)_C$ is an exact symmetry. That $SU(3)_F$ symmetry is broken can be seen in the mass differences among members of the meson and baryon multiplets. Since $SU(3)_C$ symmetry holds, there is a conserved current and associated *charge*, which is the origin of the *colour field*. The gauge bosons are a set of 8 massless, colour charged *gluons* arising from the 8 generators of SU(3). Quarks interact with the colour field via gluon exchange. As a consequence of the non-Abelian nature of SU(3), the gluons themselves are charged and so also experience the colour force. The quark model description of hadrons as bound states of 2 or 3 quarks is incomplete. The vacuum plays a crucial role in determining the properties of hadrons. Surrounding the *valence quarks*, which determine the hadron quantum numbers, is a sea of virtual gluons and $q\bar{q}$ pairs (Figure 2.4). A range of lepton scattering experiments from the nucleon [13] have shown that the valence quarks only contribute about 50 % of the total nucleon momentum and 1/3 of the total spin; sea quarks and gluons provide the rest. Furthermore, most of the mass of the hadron is due to the interaction of the valence quarks with the sea and not from the rest masses of the bare valence quarks. The current most widely accepted picture of the structure of the nucleon is valence quarks with bare masses of a few MeV surrounded by a cloud of gluons and quark-antiquark pairs, producing a hadron with a mass of $\sim$1 GeV. The

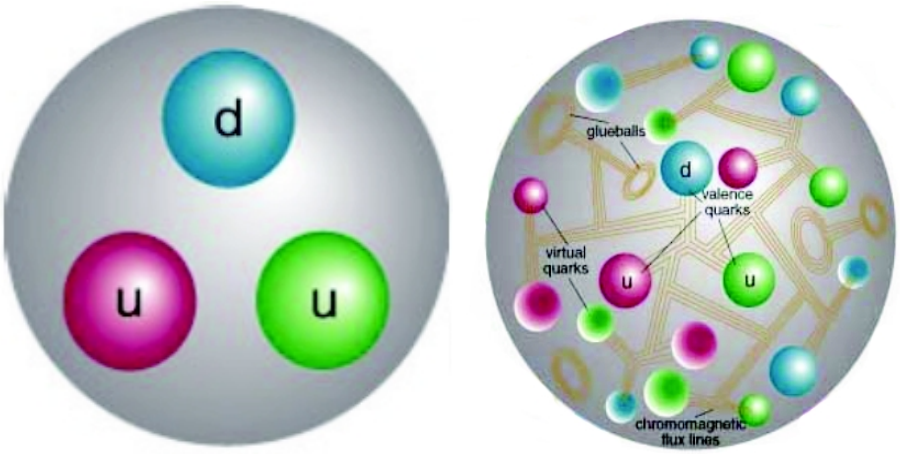

Figure 2.4: Quark model view of the proton, composed of 3 constituent quarks, on the left. A more realistic description is shown on the right: the vacuum gives rise to virtual quark and gluon pairs.

dynamic generation of mass is illustrated from the theoretical results presented in Figure 2.5, where the solid lines show predictions of the effective 'dressed' quark mass from interaction with the vacuum as a function of quark momentum.

A full mathematical description of the force between quarks and gluons can now be formulated.

2.1.3 Quantum Chromodynamics

The gauge invariant field theory resulting from local $SU(3)_C$ symmetry is known as Quantum Chromodynamics (QCD). The QCD Lagrangian is given by

$$\mathcal{L}_{QCD} = \sum_f \bar{q}_f[i\gamma_\mu(\partial^\mu + igA^\mu) - m_f]q_f - \frac{1}{2}Tr(F_{\mu\nu}F^{\mu\nu}) \qquad (2.4)$$

where q are the quark fields, m_f are the quark masses, A^μ are the gluon fields, g is the gauge coupling, and $F_{\mu\nu}$ is the field strength tensor. The sum runs over all quark flavours.

Equation 2.4 can in principle be used as the basis to calculate the properties of mesons and baryons using perturbation theory. However, a perturbative expansion is only possible if the coupling g is small. In 1973, Politzer [15], Gross and Wilczek [16] showed that the coupling varies as a function of 4-momentum

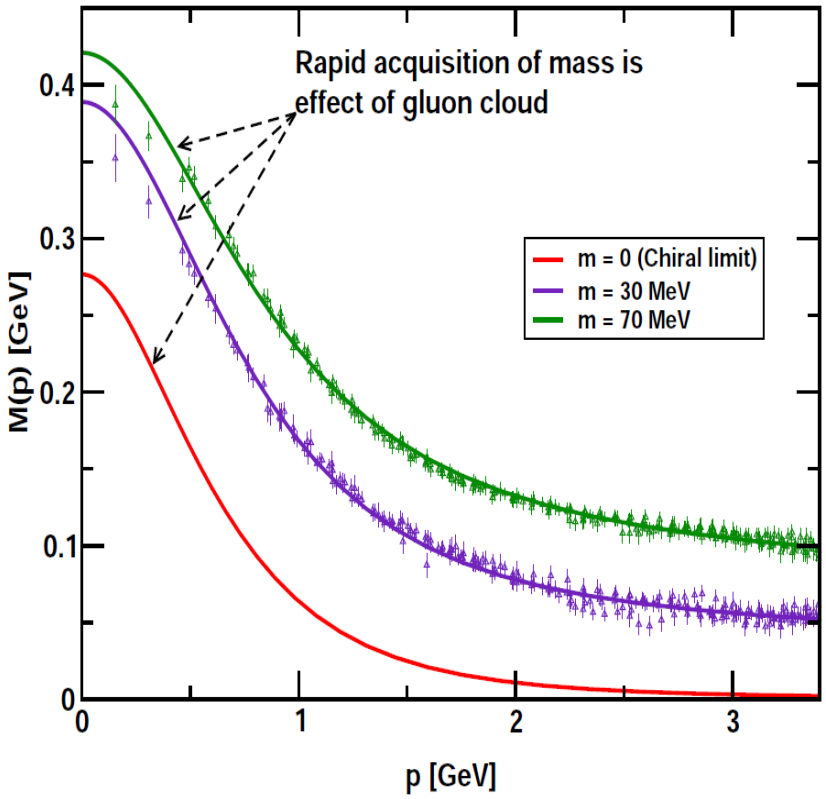

Figure 2.5: Effective quark mass as a function of momentum. The lines represent different bare quark masses. Even massless quarks can acquire an effective mass by accumulating a cloud of gluons [14].

transfer squared Q^2 as

$$g^2(Q^2) = \frac{4\pi}{\beta_0 \ln(Q^2/\Lambda^2_{QCD})}$$

where $\beta_0 > 0$ is a renormalization constant and $\Lambda_{QCD} \sim 200$ MeV, translating to a length scale of roughly the size of a hadron.

Figure 2.6 illustrates the behaviour of g. As $Q^2 \to \Lambda^2_{QCD}$, $g \to \infty$. Conversely, as $Q^2 \to \infty$, $g \to 0$. This critical feature of QCD is known as *asymptotic freedom*. As the distance between quarks decreases, the strength of the strong interaction decreases, allowing perturbative calculations to be performed. However, for $g > 1$, perturbation theory is no longer applicable, and Equation 2.4 is intractable. Calculations in this energy regime require model simplifications and novel computational methods. Understanding the structure of the nucleon necessitates the application of QCD in this non-perturbative regime.

2.2 The Nucleon in QCD

Several approaches to QCD in the non-perturbative region are outlined below. These generally fall into two categories: techniques of calculating QCD from first principles, and phenomenological models constructed around observed but unproven properties of QCD such as confinement.

2.2.1 Calculations

2.2.1.1 Lattice QCD

In 1974, Wilson [18] proposed a method of computing low energy QCD on a finite discretised space-time lattice using the Feynman path integral approach (Figure 2.7). Quarks reside on lattice sites, and gluons are the 'links' between them on a 4-dimensional (3 spatial + 1 time) hypercube. Calculations are performed using specified values of the coupling, quark masses, and lattice spacing. Lattice spacings are taken to be less than the ~ 1 fm diameter of a typical hadron. The results obtained approach the physical values as the lattice spacing decreases and realistic quark masses are used.

For a typical lattice size of 3 fm and lattice spacing of 0.1 fm, there are 32^4 sites and $4 \times 32^4 = 4194304$ links. The total number of configurations is then

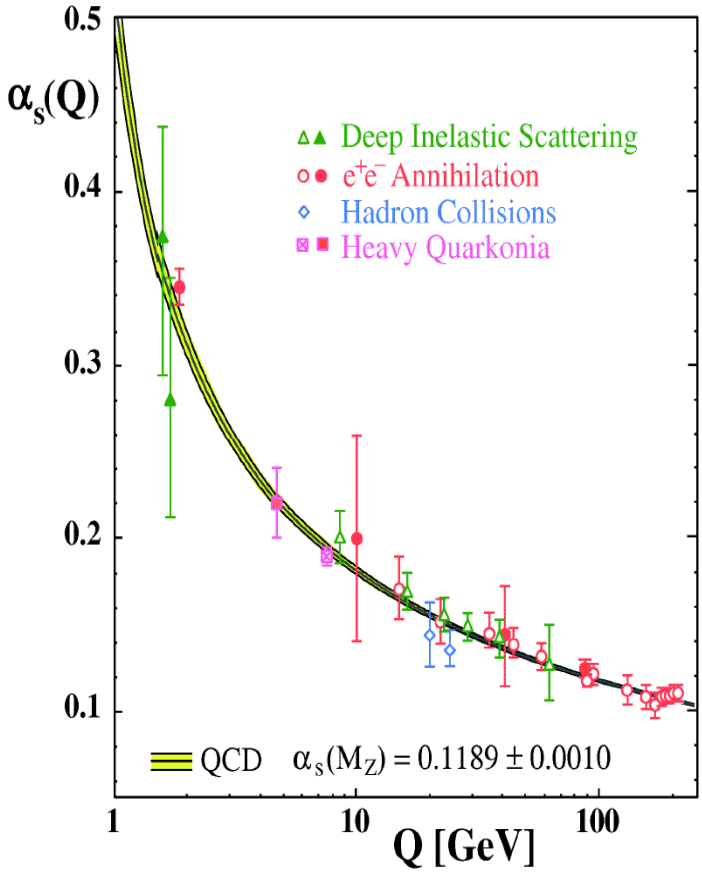

Figure 2.6: The strong coupling constant tends asymptotically to infinity as the length scale of the interaction increases. Shown here is the theoretical prediction of $g = \alpha_s(Q)$ plotted with experimentally determined values [17].

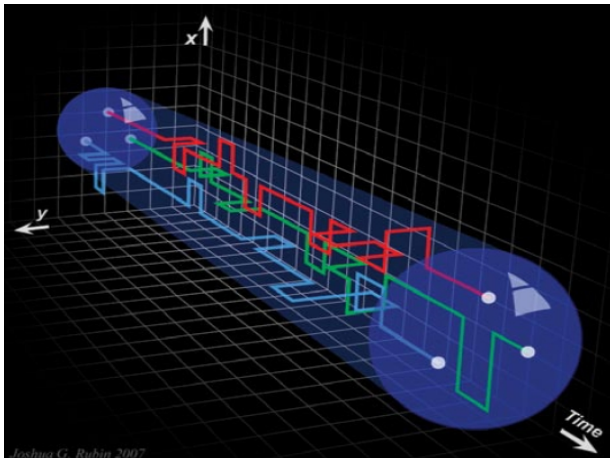

Figure 2.7: Image of a hadron propagating on the lattice [19].

$10^{4194304}$, ruling out a direct evaluation. Monte Carlo methods [20] are employed to approximate the large number of path integrals, though full calculations still require significant computing resources and are performed on supercomputers.

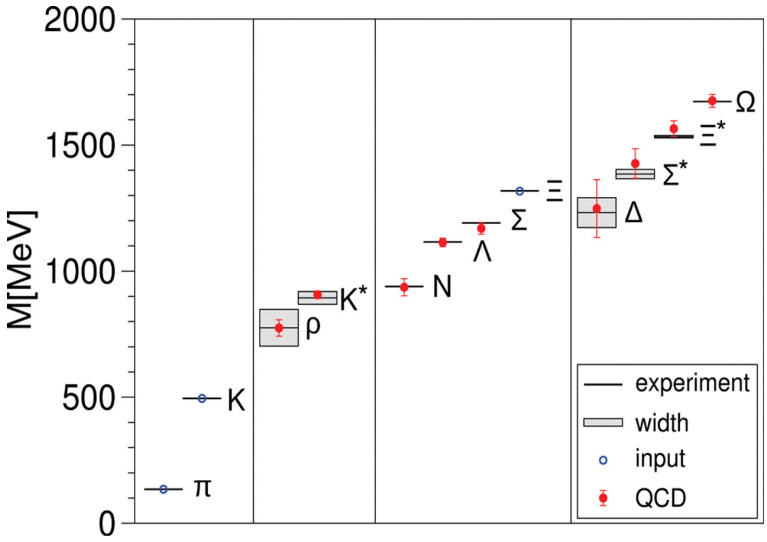

Figure 2.8: Lattice results for the ground state masses of several hadrons compared with experimental values [21].

The masses of several light hadrons has been computed on the lattice [21] and agree well with experimental values (Figure 2.8). Efforts are ongoing to calculate properties such as form factors and excitation spectra. Rapid advances in the

accuracy of lattice results are expected as the available computational power increases.

2.2.1.2 Holographic Dual of QCD

Holographic Dual QCD [22] is based on the similarity between SU(N) gauge theories and 10-dimensional string theory known as the anti-de Sitter/Conformal Field Theory (AdS/CFT) correspondence. This allows non-perturbative features of QCD to be investigated using the dual string theory, where the only parameter is the energy scale Λ_{QCD}. Hadron properties are extracted from string wave functions defined on an AdS space. This framework has had some success in reproducing the nucleon excitation spectrum [23] (Figure 2.9), though the lowest lying states are predicted at masses higher than experimental values. Interestingly, this approach uniquely predicts the existence of certain resonances, the experimental observation of which could help to validate the approach.

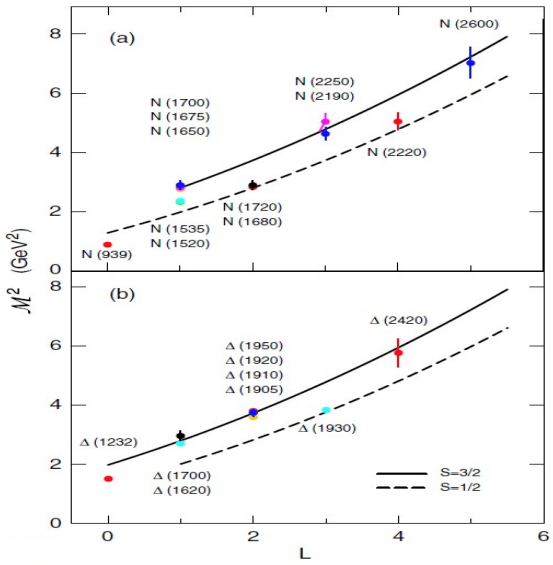

Figure 2.9: Results from a holographic dual of QCD [23] for nucleon (top) and Δ resonances. The x-axis is the orbital angular momentum.

2.2.1.3 Dyson-Schwinger Equations

Dyson-Schwinger equations [24] are an infinite set of coupled integrals describing the Euler-Lagrange equations of motion whose solutions are Green's functions. A truncation point n is chosen to limit the 'tower' of equations by only considering n-point Green's functions. The omitted functions are then treated with an Ansatz based on known symmetries of the field theory. This method has been applied to the calculation of the weak and strong form factors of the nucleon [25], and work is progressing on predictions for the nucleon excitation spectrum.

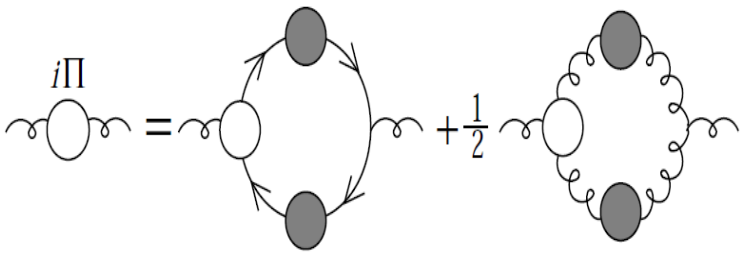

Figure 2.10: The Dyson-Schwinger equation for the gluon propagator [24].

2.2.2 Phenomenological Models

2.2.2.1 Soliton Models

In the late 1950's, Skyrme [26] presented a framework describing baryons as excitations (solitons) of a meson field, the sources of which were massless pions. Soliton solutions are obtained from the effective Lagrangian of the chiral symmetry group $SU(2)_L \times SU(2)_R$, where the subscripts refer to left- and right-handed particles. This model is able to account for the short-range repulsion of the nucleon-nucleon interaction, and nucleon properties such as masses, magnetic moments, and charge radii can be calculated to within 30% of experimental values [27].

2.2.2.2 MIT Bag Model

The MIT bag model [28] constrains massless quarks and gluons to exist inside a spherical region of space referred to as 'the bag'. Quarks interact via gluon exchange with a specified coupling α_C which is a model parameter. Quark wave functions are zero outside the bag, and conservation of energy and momentum imposes boundary conditions that prevent any colour flux across the bag's surface. Consequently the resulting hadrons must be colour singlet states. Quarks are kept inside by an external pressure with a constant energy per unit volume B of about 1 GeV/fm^3. The energy of the system is then given by

$$E_{Bag} = \frac{a}{V^{1/3}} + VB$$

where V is the volume of the bag, and a 0 is a constant. The $V^{-1/3}$ term is the kinetic energy of the quarks, and VB is the external pressure. This model met with some success in reproducing the spectrum of hadrons with a mass of less than 2 GeV and $J \leq \frac{3}{2}$ [29]. It was further refined to restore chiral symmetry by incorporating a pion cloud at the surface of the bag which couples to quarks [30], enabling a successful fit to πN scattering amplitudes in the delta resonance region.

2.2.2.3 Constituent Quark Model

As shown in Figure 2.5, most of the mass of a hadron is the result of the interaction of the valence quarks with the QCD vacuum. In particular, the valence quarks acquire an effective mass through spontaneous chiral symmetry breaking of the vacuum [31]. These *constituent* quarks with masses ~300 MeV (approximately 1/3 the mass of a nucleon) are the degrees of freedom of constituent quark models. Faiman and Hendry [32] modeled the nucleon as a 3 quark system in a harmonic oscillator potential using the Hamiltonian

$$H = \sum_j \frac{\mathbf{p}_j^2}{2M} + \frac{1}{2}M\omega^2 \sum_{i<j} (\mathbf{r}_i - \mathbf{r}_j)^2$$

for quarks with momenta $\mathbf{p}_i$ and positions $\mathbf{r}_i$. Calculations of nucleon excited states from this simplified view of the nucleon were in good agreement with the handful of observed resonances up to 2 GeV. Isgur and Karl [33, 34] modified this Hamiltonian by introducing an anharmonic perturbation and a hyperfine interaction with a strong $\vec{S} \cdot \vec{S}$ component to model gluon exchange. Figure 2.11

compares the predicted nucleon excitation spectrum with observed isospin-1/2 states [35]. Most of the known resonances emerge from the model, though the lowest lying $\frac{1}{2}^+$ state of mass 1440 MeV, known as the Roper resonance, is not predicted as the first excited state. Clearly, the constituent quark model predicts many more states than have been seen in experiment.

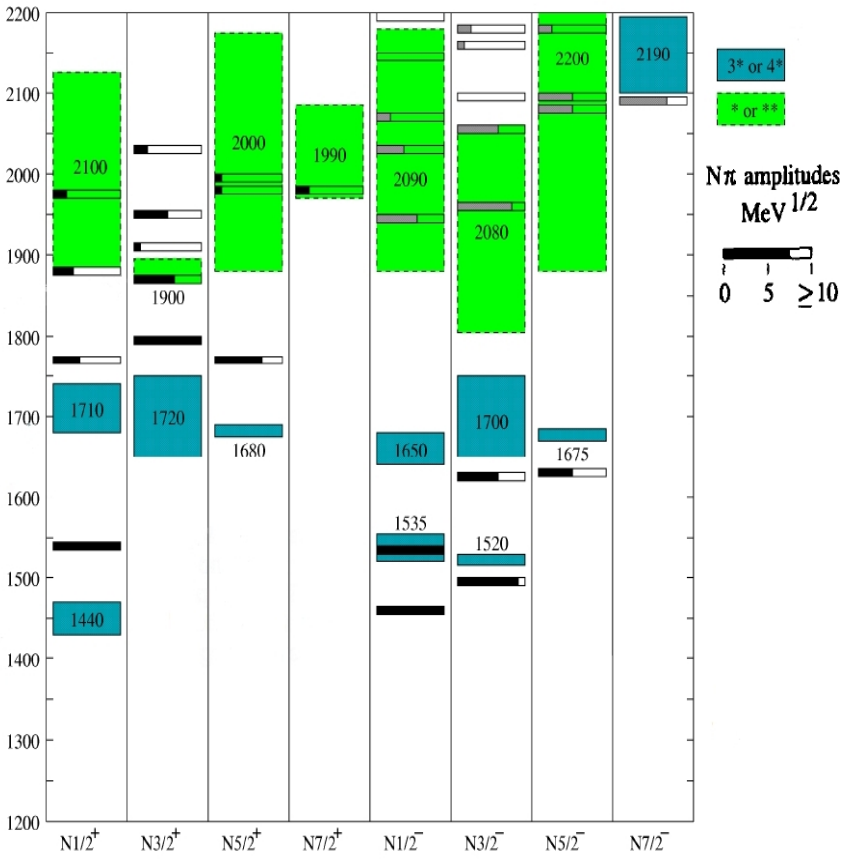

Figure 2.11: The I=1/2 nucleon resonance spectrum [35] comparing states predicted by the constituent quark model (bars) and resonances listed in the Particle Data Group (boxes). The width of the boxes gives the range of listed central values, and the colour coding refers to a classification system described in Section 2.3.

By coupling two constituent quarks together, the diquark model [36] reduces the total number of degrees of freedom and predicts fewer unobserved states [37], resulting in improved agreement with the currently established spectrum. Despite this advantage, evidence for this picture is challenged by results from lattice

QCD [38] and analysis of baryon resonance decays [39] which conclude that the short range force between quarks is not sufficiently strong to form diquarks.

2.3 Nucleon Spectroscopy

The excited states of the nucleon alluded to in the previous section arise due to its composite nature, and the spectrum provides critical insights into the dynamics of the interactions between quarks and gluons in the non-perturbative region of QCD. As demonstrated by the variety of models described previously, a full understanding of the appropriate degrees of freedom in the nucleon, a fundamental component of matter, has not yet been achieved. Phenomenological models and rapidly improving theoretical calculations crucially rely on accurate measurement of the excitation spectrum for further maturation.

Information on the excitation spectrum has mostly been acquired from scattering and the use of electromagnetic probes (photons and electrons). The full spectrum remains inadequately determined; the present situation is summarised by the Particle Data Group (PDG) in Figure 2.12 [40]. Resonances are labeled in terms of the orbital angular momentum (L), isospin, and total spin (J) as L_{2I2J}. States with isospin-1/2 (N*) are distinguished from isospin-3/2 states (Δ). The PDG has a rating system for resonances indicating the strength of the experimental evidence for the existence of each state, ranging from one star (poor) to four stars (certain). States with two or three stars appear inconsistently in partial wave analyses (discussed in detail in Section 3.3) of experimental data (Figure 2.13).

Furthermore, there are numerous 'missing' resonances predicted by constituent quark models for which there is no experimental evidence. These states may be hidden in the broad ($\sim$ 100 MeV) decay widths of neighboring states, they may decay via reaction channels which have not yet been measured, or they may simply not exist.

A particularly interesting resonance is the lowest lying N* state, the $P_{11}(1440)$ Roper resonance. While its existence is uncontroversial (four star rating), it is not accurately reproduced theoretically, leading to speculation about its structure. Efforts to incorporate this state as the first excited state of the nucleon in existing models require the use of many additional parameters and degrees of

			Status as seen in —						
Particle	$L_{2I\cdot 2J}$	Overall status	$N\pi$	$N\eta$	ΛK	ΣK	$\Delta\pi$	$N\rho$	$N\gamma$
$N(939)$	P_{11}	****							
$N(1440)$	P_{11}	****	****	*			***	*	***
$N(1520)$	D_{13}	****	****	***			****	****	****
$N(1535)$	S_{11}	****	****	****			*	**	***
$N(1650)$	S_{11}	****	****	*	***	**	***	**	***
$N(1675)$	D_{15}	****	****	*	*		****	*	****
$N(1680)$	F_{15}	****	****	*			****	****	****
$N(1700)$	D_{13}	***	***	*	**	*	**	*	**
$N(1710)$	P_{11}	***	***	**	**	*	**	*	***
$N(1720)$	P_{13}	****	****	*	**	*	*	**	**
$N(1900)$	P_{13}	**	**					*	
$N(1990)$	F_{17}	**	**	*	*	*			*
$N(2000)$	F_{15}	**	**	*	*	*	*	**	
$N(2080)$	D_{13}	**	**	*	*				*
$N(2090)$	S_{11}	*	*						
$N(2100)$	P_{11}	*	*	*					
$N(2190)$	G_{17}	****	****	*	*	*		*	*
$N(2200)$	D_{15}	**	**	*	*				
$N(2220)$	H_{19}	****	****	*					
$N(2250)$	G_{19}	****	****	*					
$N(2600)$	$I_{1\,11}$	***	***						
$N(2700)$	$K_{1\,13}$	**	**						
$\Delta(1232)$	P_{33}	****	****	F					****
$\Delta(1600)$	P_{33}	***	***	o			***	*	**
$\Delta(1620)$	S_{31}	****	****	r			****	****	***
$\Delta(1700)$	D_{33}	****	****	b		*	***	**	***
$\Delta(1750)$	P_{31}	*	*	i					
$\Delta(1900)$	S_{31}	**	**	d		*	*	**	*
$\Delta(1905)$	F_{35}	****	****	d		*	**	**	***
$\Delta(1910)$	P_{31}	****	****	e		*	*	*	*
$\Delta(1920)$	P_{33}	***	***	n		*	**		*
$\Delta(1930)$	D_{35}	***	***			*			**
$\Delta(1940)$	D_{33}	*	*	F					
$\Delta(1950)$	F_{37}	****	****	o		*	****	*	****
$\Delta(2000)$	F_{35}	**		r			**		
$\Delta(2150)$	S_{31}	*	*	b					
$\Delta(2200)$	G_{37}	*	*	i					
$\Delta(2300)$	H_{39}	**	**	d					
$\Delta(2350)$	D_{35}	*	*	d					
$\Delta(2390)$	F_{37}	*	*	e					
$\Delta(2400)$	G_{39}	**	**	n					
$\Delta(2420)$	$H_{3\,11}$	****	****						*
$\Delta(2750)$	$I_{3\,13}$	**	**						
$\Delta(2950)$	$K_{3\,15}$	**	**						

****	Existence is certain, and properties are at least fairly well explored.
***	Existence ranges from very likely to certain, but further confirmation is desirable and/or quantum numbers, branching fractions, *etc.* are not well determined
**	Evidence of existence is only fair.
*	Evidence of existence is poor.

Figure 2.12: Nucleon resonances listed by the PDG [40].

Resonance	Our estimate	Our rating	KH	CM	Kent	GWU	BnGa
$N_{1/2+}(1440)$	1450±32; 300±100	****	1410±12; 135±10	1440±30; 340±70	1462±10; 391±34	1485 ± 1; 284±18	1440±12; 335±50
$N_{3/2-}(1520)$	1522 ± 4; 115±10	****	1519 ± 4; 114 ± 7	1525±10; 120±15	1524 ± 4; 124 ± 8	1516± 1; 99± 3	1524 ± 4; 117 ± 6
$N_{1/2-}(1535)$	1538±10; 175±45	****	1526 ± 7; 120±20	1550±40; 240±80	1534 ± 7; 151±27	1547 ± 1; 188± 4	1535±20; 170±35
$N_{1/2-}(1650)$	1660±18; 165±25	****	1670 ± 8; 180±20	1650±30; 150±40	1659 ± 9; 170±12	1635 ± 1; 115 ± 3	1680±40; 170±45
$N_{5/2-}(1675)$	1675 ± 5; 153±22	****	1679 ± 8; 120±15	1675±10; 160±20	1676 ± 2; 159± 7	1674 ± 1; 147 ± 1	1678 ± 5; 177±15
$N_{5/2+}(1680)$	1683 ± 3; 126 ± 9	****	1684 ± 3; 128± 8	1680±10; 120±10	1684 ± 4; 139± 8	1680 ± 1; 128 ± 1	1685 ± 5; 117±12
$N_{3/2-}(1700)$	1725±50; 190±110	***	1731±15; 110±30	1675±25; 90±40	1737±44; 250±230	-	1730±40; 310±60
$N_{1/2+}(1710)$	1713±12;220±180	***	1723 ± 9; 120±15	1700±50; 90±30	1717±28; 480±330	-	1725±25;200±35
$N_{3/2+}(1720)$	1730±30; 320±210	****	1710±20; 190±30	1700±50; 125±70	1717±31; 380±180	1750 ± 5; 256±22	1770±100; 650±120
$N_{3/2-}(1860)$	1850±40; 260±170	**	-	1880±100; 180±60	1804±55; 450±185	-	1870±25;150±40
$N_{5/2+}(1870)$	1880±40; 270±180	$\overline{**}$	1882±10; 95±20	-	1903±87; 490±310	1818; 118	1910±50; 360±80
$N_{1/2+}(1880)$	1890±50; 210±100	*	-	-	1885±30; 113±44	-	1900±30; 300±40
$N_{3/2+}(1900)$	1940±50; 340±150	*	-	-	1879±17; 498±78	-	1960±30; 185±40
$N_{1/2-}(1905)$	1905±50; 250±150	*	1880±20; 95±30	-	1928±59; 414±157	-	-
$N_{7/2+}(1990)$	2020±60; 410±110	**	2005±150; 350±100	1970±50; 350±120	2086±28; 535±120	-	-
$N_{3/2-}(2080)$	2100±55; 310±110	$\overline{**}$	2080±20; 265±40	2060±80; 300±100	-	-	2160±35; 370±50
$N_{1/2-}(2090)$				2180±80; 350±100	-	-	-
$N_{1/2+}(2100)$	2090±100; 230±200	*	2050±20; 200±30	2125±75; 260±100	-	-	-
$N_{5/2-}(2200)$	2160±85; 350±50	**	2228±30; 310±50	2180±80; 400±100	-	-	2065±25; 340±40
			KH	CM	Kent	GWU	Hendry
$N_{7/2-}(2190)$	2150±30; 440±110	****	2140±12; 390±30	2200±70; 500±150	2127± 9; 550±50	2152±2; 484±13	2140± 40; 270± 50
$N_{9/2+}(2220)$	2260±60; 490±115	****	2205±10; 365±30	2230±80; 500±150	-	2316±3; 633±17	2300±100; 450±150
$N_{9/2-}(2250)$	2255±50; 420±150	****	2268±15; 300±40	2250±80; 400±120	-	2302±6; 628±28	2200±100; 350±100
$N_{11/2-}(2600)$	2630±120; 650±250	**	2577±50;400±100	-	-	-	2700±100; 900±100
$N_{13/2+}(2700)$	2800±160; 600±300	**	2612±45; 350±50	-	-	-	3000±100; 900±150
			KH	CM	Kent	GWU	BnGa
$\Delta_{3/2+}(1232)$	1232 ± 1; 118 ± 2	****	1232 ± 3; 116 ± 5	1232 ± 2; 120 ± 5	1231 ± 1; 118 ± 4	1233 ± 1; 119 ± 1	1230 ± 2; 112 ± 4
$\Delta_{3/2+}(1600)$	1615±80; 360±120	***	1522±15; 220±40	1600±50; 300±100	1706±10; 430±73	-	1640±40; 480±100
$\Delta_{1/2-}(1620)$	1626±23; 130 ± 45	****	1610 ± 7; 139±18	1620±20; 140±20	1672 ± 7; 154±37	1614 ± 1; 71 ± 3	1625±10; 148±15
$\Delta_{3/2-}(1700)$	1720±50; 370±200	****	1680±70; 230±80	1710±30; 280±80	1762±44; 600±250	1688 ± 3; 182 ± 8	1780±40; 580±120
$\Delta_{1/2+}(1750)$			-	-	1744±36; 300±120	-	-
$\Delta_{1/2-}(1900)$	1910±50; 190±100	**	1908±30; 140±40	1890±50; 170±50	1920±24; 263±39	-	-
$\Delta_{5/2+}(1905)$	1885±25; 330 ± 50	****	1905±20; 260±20	1910±30; 400±100	1881±18; 327±51	1856 ± 2; 321± 9	1870±32; 340±32
$\Delta_{1/2+}(1910)$	1935±90; 280±150	****	1888±20; 280±50	1910±40; 225±50	1882±10; 229±25	2068 ± 2; 543±10	-
$\Delta_{3/2+}(1920)$	1950±70; 260±100	***	1868±10; 220±80	1920±80; 300±100	2014±16; 152±55	-	1995±40; 360±50
$\Delta_{5/2-}(1930)$	1930±30; 350±170	$\overline{**}$	1901±15; 195±60	1940±30; 320±60	1956±22; 530±140	-	-
$\Delta_{3/2-}(1940)$	1995±60; 340±130	$\overline{**}$	-	1940±100;200±100	2057±110; 460±320	-	1995±40; 360 ± 50
$\Delta_{7/2+}(1950)$	1930±16; 285 ± 45	****	1913 ± 8; 224±10	1950±15; 340±50	1945 ± 2; 300 ± 7	1921± 1; 271 ± 1	1928±8; 290±14
$\Delta_{5/2+}(2000)$			2200±125;400±125	-	1752±32; 251±93	-	-
$\Delta_{1/2-}(2150)$			-	2200±100; 200±100	-	-	-
			KH	CM	Kent	GWU	Hendry
$\Delta_{7/2-}(2200)$	2230 ± 50; 420±100	**	2215±10; 400±100	2200±80; 450±100	-	-	2280±80; 400±150
$\Delta_{9/2+}(2300)$	2360±125; 420±200	**	2217±80; 300±100	2400±125; 425±150	-	-	2450±100; 500±200
$\Delta_{5/2-}(2350)$	2310 ± 85; 490±250	***	2305±26; 300 ± 70	2400±125; 400±150	-	2233±53; 773±187	-
$\Delta_{7/2+}(2390)$	2390±100; 300±200	*	2425 ± 60; 300 ± 80	2350±100; 300±100	-	-	-
$\Delta_{9/2-}(2400)$	2400±190; 530±300	**	2468±50;480±100	2300±100; 330±100	-	2643±141; 895±432	2200±100; 450±200
$\Delta_{11/2+}(2420)$	2462±120; 490±150	***	2416 ± 17; 340±28	2400±125; 450±150	-	2633±29; 692 ± 47	2400±60; 460±100
$\Delta_{13/2-}(2750)$	2720±100; 420±200	**	2794±80; 350±100	-	-	-	2650±100; 500±100
$\Delta_{15/2+}(2950)$	2920±100; 500±200	**	2990±100; 330±100	-	-	-	2850±100; 700±200

Figure 2.13: Masses and widths, in MeV, of nucleon resonances as seen in several partial wave analyses [41]. Two and three star resonances are observed inconsistently.

freedom [42]. The excitation is generally described as a breathing mode of the nucleon. Additional experimental input is essential to provide further constraints on the nature of this state.

2.3.1 Possible New Narrow Resonance

QCD requires hadrons to have no net colour. The simplest quark structures satisfying this condition are $q\bar{q}$ and qqq, and all known hadrons have one of these configurations. There are however other quark combinations which can produce colour singlets, such as a $qqqq\bar{q}$ pentaquark, which are not *a priori* forbidden by QCD. These 'exotic' states would have quantum numbers not possible in a two- or three-quark system, and would appear in a $J^P=\frac{1}{2}^+$ antidecuplet [43]. In Figure 2.14, the elements of the S=−2 quadruplet and S=1 singlet are exotic, while the remaining particles are three quark states. A series of experiments [44] in the late 1990's and early 2000's using photon beams incident on nucleon targets provided evidence for the Θ^+, though later experiments with improved statistics refuted claims that a pentaquark had been observed.

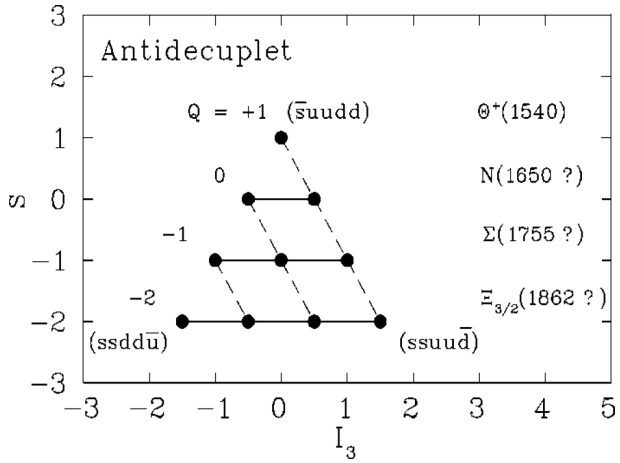

Figure 2.14: Theorised antidecuplet, containing states with exotic quantum numbers [45].

Partial wave analysis [45] of πN elastic scattering data suggests a new nucleon resonance with a mass of 1680 MeV and a maximum width of $\sim$ 30 MeV as a non-strange member of the antidecuplet. It is predicted to couple more strongly to the $N\eta$ decay channel than to $N\pi$. Recent data on η photoproduction off

the neutron [46, 47] (Figure 2.15) have been interpreted by some [48] as giving a signal for this state. However, a more comprehensive set of measurements is needed to provide a convincing body of evidence in support of its existence.

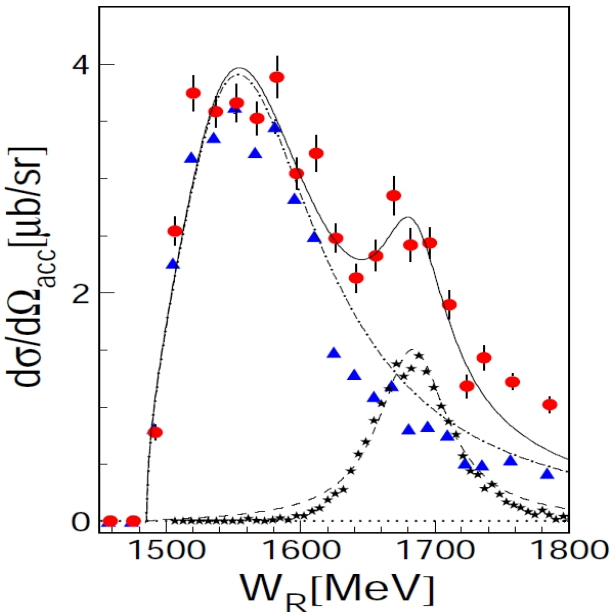

Figure 2.15: Cross-section measurement for η photoproduction off the proton (blue) and the neutron (red) [46]. A bump in the neutron cross-section at a system energy of W=1680 MeV was observed. Some have taken this structure as evidence of a new narrow resonance. The dot dashed line is a Breit-Wigner curve for the well-established $S_{11}(1535)$ resonance, and the star line is a delta-resonance centred at W=1680 MeV, smeared by the detector resolutions.

2.4 Summary

QCD is the $SU(3)_C$ gauge theory of the strong interaction with quarks and gluons as the fundamental fields. Two key features of the theory are the confinement of quarks into colour neutral objects and the asymptotic behaviour of the strong coupling. As the distance of the interaction increases, the coupling tends to infinity, precluding the application of perturbation theory. As a result, various theoretical techniques and phenomenological methods have been developed to make predictions in the non-perturbative realm of QCD. The nucleon excitation

spectrum is a reflection of the intricate interactions among quarks and gluons in this non-perturbative regime. No model has been able to accurately reproduce the entire spectrum, highlighting the difficulty in identifying the relevant degrees of freedom. Novel methods of computing the spectrum from first principles are progressing steadily, though even the lowest lying isospin-1/2 resonance is not well described. The world data set of nucleon excited states remains incomplete, and the existence of several states is still in doubt. There is a clear need to improve the experimental determination of the excitation spectrum to test the validity of the many theoretical approaches and achieve a better understanding of the structure of the nucleon.

Chapter 3

Meson Photoproduction

Photoproduction reactions offer an appealing mechanism to study the excitation spectrum because the interaction proceeds via the well-understood electromagnetic interaction (QED), the photon is able to probe the entire volume of the nucleon, and the production of intense, polarised photon beams is possible. The meson photoproduction process can proceed via a number of mechanisms. The main one of interest to this work is when photon beams incident on a nucleon target excite a resonance, which then decays strongly to a nucleon-meson final state. However, background processes also occur and must be accounted for in the theoretical framework. The formalism of pion photoproduction, and how it is used to access the excitation spectrum, is described here in detail.

3.1 Reaction Mechanism

3.1.1 Kinematics

The photon-nucleon interaction is shown schematically in Figure 3.1, where the labels $\mathbf{k}$, $\mathbf{p}_i$, $\mathbf{q}$, $\mathbf{p}_f$ denote the 4-momenta of the incoming photon, target nucleon, meson, and recoiling nucleon with energies E_γ, E_i, E_π, E_f. It follows from conservation of 4-momentum that

$$\mathbf{k} + \mathbf{p}_i = \mathbf{q} + \mathbf{p}_f \tag{3.1}$$

and only three of the 4-vectors are independent. These can be chosen as $\mathbf{k}$, $\mathbf{q}$, and $\mathbf{P} = \frac{1}{2}(\mathbf{p}_i + \mathbf{p}_f)$. It is useful to introduce the Mandelstam variables s, t, and

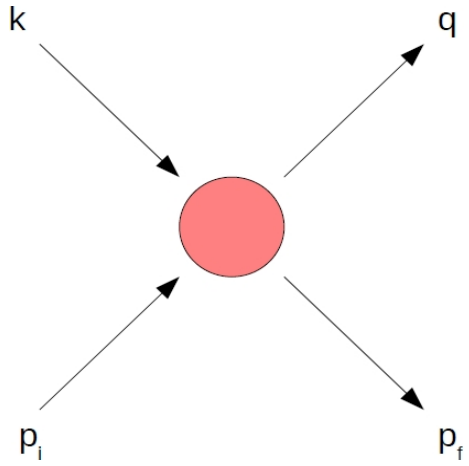

Figure 3.1: Two body reaction between a photon and a nucleon ($\mathbf{k}$ and $\mathbf{p}_i$ respectively) resulting in a final state of a meson ($\mathbf{q}$) and a recoiling nucleon ($\mathbf{p}_f$).

u, defined as

$$s = (\mathbf{k} + \mathbf{p}_i)^2, \qquad t = (\mathbf{p}_i - \mathbf{p}_f)^2, \qquad u = (\mathbf{p}_i - \mathbf{q})^2 \tag{3.2}$$

These are a set of Lorentz invariant scalars whose sum is related to the masses of all four particles

$$s + t + u = \sum_{i=1}^{4} m_i^2 \tag{3.3}$$

Note that $s = W^2$ is the centre of mass energy, and $t = Q^2$ is the momentum transfer of the reaction. The probability amplitude to go from an initial state $|i\rangle$ to a final state $|f\rangle$ as drawn in Figure 3.1 is given by the scattering matrix, expressed in the convention of Bjorken and Drell [49] as

$$S_{fi} = \langle f|S|i\rangle = \delta_{fi} - \frac{i}{4\pi^2}\delta^4(p_f + q - k - p_i)\left(\frac{M^2}{4E_f E_\pi E_\gamma E_i}\right)^{1/2} T_{fi} \tag{3.4}$$

where M is the mass of the nucleon and T_{fi} is the transition matrix element. The T-matrix is calculated from the photon polarisation vector ε_μ and the nucleon electromagnetic current J_μ^{fi} by

$$T_{fi} = \varepsilon_\mu J_\mu^{fi} \tag{3.5}$$

and is related to the differential cross-section [50] by

$$\frac{d\sigma}{d\Omega} = \frac{q}{k}\sum\left|\frac{M}{4\pi W}T_{fi}\right|^2 \tag{3.6}$$

where the summation encompasses all photon polarisations and all magnetic quantum numbers of the nucleon states.

3.1.2 Reaction Amplitudes

Chew, Goldberger, Low, and Nambu [51] wrote the nucleon electromagnetic current as a function of the nucleon spin matrices σ and the photon and pion unit vectors $\hat{\mathbf{k}}$ and $\hat{\mathbf{q}}$ as

$$\mathbf{J} = \frac{4\pi W}{M}(i\sigma\mathcal{F}_1 + (\sigma\cdot\hat{\mathbf{k}})(\sigma\times\hat{\mathbf{q}})\mathcal{F}_2 + i\tilde{\mathbf{k}}(\tilde{\sigma}\cdot\hat{\mathbf{q}})\mathcal{F}_3 + i\tilde{\mathbf{k}}(\sigma\cdot\hat{\mathbf{k}})\mathcal{F}_4) \tag{3.7}$$

where $\tilde{\sigma} = \sigma$ - $(\sigma\cdot\hat{\mathbf{q}})\hat{\mathbf{q}}$ and $\tilde{\mathbf{k}} = \mathbf{k}$ - $(\mathbf{k}\cdot\hat{\mathbf{q}})\hat{\mathbf{q}}$. The objects $\mathcal{F}_1$-$\mathcal{F}_4$ are complex-valued functions of s and t refered to as CGLN amplitudes, within which are contained the dynamics of resonance production. These can be expanded in a multipole series of partial waves as

$$\mathcal{F}_1(\theta) = \sum_{l=0}^{\infty}(lM_{l+} + E_{l+})P'_{l-1}(\cos\theta) + ((l+1)M_{l-} + E_{l-})P'_{l-1}(\cos\theta) \tag{3.8}$$

$$\mathcal{F}_2(\theta) = \sum_{l=0}^{\infty}((l+1)M_{l+} + lM_{l-})P'_{l}(\cos\theta) \tag{3.9}$$

$$\mathcal{F}_3(\theta) = \sum_{l=0}^{\infty}(E_{l+} - M_{l+})P''_{l+1}(\cos\theta) + (E_{l-} + M_{l-})P''_{l-1}(\cos\theta) \tag{3.10}$$

$$\mathcal{F}_4(\theta) = \sum_{l=0}^{\infty}(M_{l+} - E_{l+} - M_{l-} - E_{l-})P''_{l}(\cos\theta) \tag{3.11}$$

where θ is the center of mass angle, l is the angular momentum of the pion, and E/M refer to electric or magnetic multipoles. The subscripts indicate how the nucleon spin couples to the angular momentum; $l\pm$ indicates that the total angular momentum is given by $J = l \pm 1/2$. The parity P of the intermediate state is determined by the type of electromagnetic transition and the momentum of the incoming photon J_γ. For electric multipoles, $P = (-1)^{J_\gamma}$ and for magnetic multipoles, $P = (-1)^{J_\gamma+1}$. Inspecting the quantum numbers of the nucleon resonances reveals which partial waves contribute to each excited state. For example, the

N(1440) resonance with $J^P=\frac{1}{2}^+$ is produced by the M_{1-} multipole (J_γ=1), while the N(1520) state ($J^P=\frac{3}{2}^-$) results from both the E_{2-} (J_γ=1) and M_{2-} (J_γ=2) multipoles.

Unlike the strong interaction, isospin is not a conserved quantity in electromagnetic transitions; the Hamiltonian has an isoscalar component ($|\Delta I|$=0) and an isovector component ($|\Delta I|$=0,±1). The photon has I=0, giving the initial state an isospin of 1/2 due to the nucleon. The isoscalar term will produce a final state with I=1/2 with amplitude A^0, and the the isovector term can give a final state isospin of I=1/2 or I=3/2 with amplitudes A^1 and A^3 respectively [52]. Thus the production amplitudes for each of the reactions

$$\gamma + p \rightarrow \pi^0 + p$$
$$\gamma + p \rightarrow \pi^+ + n$$
$$\gamma + n \rightarrow \pi^0 + n$$
$$\gamma + n \rightarrow \pi^- + p$$

have three components. As a result, each partial wave in Equation 3.11 requires twelve multipoles [50]

$$E^{(0)}_{l\pm}, \qquad E^{(1)}_{l\pm}, \qquad E^{(3)}_{l\pm}, \qquad M^{(0)}_{l\pm}, \qquad M^{(1)}_{l\pm}, \qquad M^{(3)}_{l\pm}$$

Separating the different isospin components requires measurement of all the reaction channels listed above.

3.2 Polarisation Observables

Analytic discussions of photoproduction often proceed in terms of s-channel helicity amplitudes, which can be written as a linear combination of the CGLN amplitudes. The photon and nucleon each have two helicity states. This results in four helicity amplitudes, labeled S_1, S_2, N, and D, which correspond to two single helicity flips, no helicity flip, and double helicity flip transitions respecitively [53]. In this framework, the differential cross-section is given by

$$\frac{d\sigma}{d\Omega} = |S_1|^2 + |S_2|^2 + |N|^2 + |D^2| \tag{3.12}$$

Equivalently, the set of transversity amplitudes is defined as

$$\begin{aligned} b_1 &= \frac{1}{2}[(S_1 + S_2) + i(N - D)] \\ b_2 &= \frac{1}{2}[(S_1 + S_2) - i(N - D)] \\ b_3 &= \frac{1}{2}[(S_1 - S_2) - i(N + D)] \\ b_4 &= \frac{1}{2}[(S_1 - S_2) + i(N + D)] \end{aligned}$$

Taking bilinear combinations of these complex-valued amplitudes results in sixteen real, and therefore measurable, quantities known as *polarisation observables*, summarised in Table 3.1. The differential cross-section is grouped with three single polarisation observables which require experiments with known polarisation of the photon beam, target, or recoiling nucleon. The remaining twelve observables are grouped into three quartets of double polarisation observables, corresponding to simultaneous measurement of beam-target, beam-recoil, and target-recoil polarisations. Measurement of these observables requires combinations of circularly and linearly polarised photon beams, transversely and longitudinally polarised targets, and determination of the transverse and longitudinal polarisation components of the recoiling nucleon.

In the transversity representation, the single polarisation observables constrain the moduli of the reaction amplitudes, and the double polarisation observables constrain the phases. The sixteen observables are not all independent. A 'complete measurement' allowing an unambiguous determination of the reaction amplitudes requires knowledge of at least eight well-chosen observables [54]. These must include five double polarisation observables chosen from each of the beam-target, beam-recoil, and target-recoil sets. Double polarisation experiments are technically challenging to perform; a secondary scatter is needed to measure recoil polarisation, and workable polarised targets which do not significantly reduce the angular acceptance for emitted particles have only recently been developed. Consequently, the world database of polarisation observables remains incomplete, and determination of the amplitudes and their resonance composition is not fully constrained by data, leading to model dependencies and large inconsistencies between analyses based on different models.

The observable measured for this thesis, C_x, is a double polarisation observable in the beam-recoil set where the polarisation transferred from a circularly

polarised photon beam to the recoiling proton is measured. The technique used to measure recoil polarisation is described in Chapter 7.

3.3 Partial Wave Analysis

The measurement of polarisation observables does not directly provide information on the nucleon excitation spectrum. A partial wave analysis is necessary to obtain the multipole decomposition of the reaction amplitudes. Further analysis of these amplitudes is necessary to extract the resonance spectrum.

In addition to s-channel resonance excitations, the amplitudes include all other processes which tranform a γN initial state to a nucleon+meson final state. The energy dependant T-matrix of the interaction going from initial state a to final state b has a resonant and non-resonant contribution [55]

$$T_{a,b}(E) = T^{bg} + T^{R} \tag{3.13}$$

Of the various partial wave analyses which have been developed, the two most widely used models for photoproduction are MAID and SAID. Each model uses a different method of parameterising the background and resonant terms of the T-matrix. Model parameters are extracted via a fit to experimental data, and solutions provide a form of the reaction amplitudes which can be compared to measured values of polarisation observables. The defining characteristics of these models are summarised here.

3.3.1 MAID

The unitary isobar model MAID [56, 57] only considers the πN channel. The non-resonant background is attributed to Born terms arising from t-channel vector meson exchange and a mixed pseudoscalar-pseudovector πNN coupling. A sharp 450 MeV cutoff separates the low energy regime of pseudovector coupling from the pseudovector dominance at higher energies [55]. Five parameters are used to model these effects.

The resonance terms are parameterised using Breit-Wigner forms as

$$T^{R} = \sum_{N_i^*} T^{N_i^*}_{\pi N,\gamma N} \tag{3.14}$$

Usual symbols	Helicity representation	Transversity representation	Experiment required[a]
σ/t	$\|N\|^2+\|S_1\|^2+\|S_2\|^2+\|D\|^2$	$\|b_1\|^2+\|b_2\|^2+\|b_3\|^2+\|b_4\|^2$	$\{-;-;-\}$
Σ	$2\Re(S_1^*S_2 - ND^*)$	$\|b_1\|^2+\|b_2\|^2-\|b_3\|^2-\|b_4\|^2$	$\{L(\frac{\pi}{2},0);-;-\}$ $\{-;y;y\}$
T	$2\Im(S_1N^* - S_2D^*)$	$\|b_1\|^2-\|b_2\|^2-\|b_3\|^2+\|b_4\|^2$	$\{-;y;-\}$ $\{L(\frac{\pi}{2},0);0;y\}$
P	$2\Im(S_2N^* - S_1D^*)$	$\|b_1\|^2-\|b_2\|^2+\|b_3\|^2-\|b_4\|^2$	$\{-;-;y\}$ $\{L(\frac{\pi}{2},0);y;-\}$
G	$-2\Im(S_1S_2^* + ND^*)$	$2\Im(b_1b_3^* + b_2b_4^*)$	$\{L(\pm\frac{\pi}{4});z;-\}$
H	$-2\Im(S_1D^* + S_2N^*)$	$-2\Re(b_1b_3^* - b_2b_4^*)$	$\{L(\pm\frac{\pi}{4});x;-\}$
E	$\|S_2\|^2-\|S_1\|^2-\|D\|^2+\|N\|^2$	$-2\Re(b_1b_3^* + b_2b_4^*)$	$\{c;z;-\}$
F	$2\Re(S_2D^* + S_1N^*)$	$2\Im(b_1b_3^* - b_2b_4^*)$	$\{c;x;-\}$
O_x	$-2\Im(S_2D_2^* + S_1N^*)$	$-2\Re(b_1b_4^* - b_2b_3^*)$	$\{L(\pm\frac{\pi}{4});-;x'\}$
O_z	$-2\Im(S_2S_1^* + ND^*)$	$-2\Im(b_1b_4^* + b_2b_3^*)$	$\{L(\pm\frac{\pi}{4});-;z'\}$
C_x	$-2\Re(S_2N^* + S_1D^*)$	$2\Im(b_1b_4^* - b_2b_3^*)$	$\{c;-;x'\}$
C_z	$\|S_2\|^2-\|S_1\|^2-\|N\|^2+\|D\|^2$	$-2\Re(b_1b_4^* + b_2b_3^*)$	$\{c;-;z'\}$
T_x	$2\Re(S_1S_2^* + ND^*)$	$2\Re(b_1b_2^* - b_3b_4^*)$	$\{-;x;x'\}$
T_z	$2\Re(S_1N^* + S_2D^*)$	$2\Im(b_1b_2^* - b_3b_4^*)$	$\{-;x;z'\}$
L_x	$2\Re(S_2N^* - S_1D^*)$	$2\Im(b_1b_2^* + b_3b_4^*)$	$\{-;z;x'\}$
L_z	$\|S_1\|^2+\|S_2\|^2-\|N\|^2-\|D\|^2$	$2\Re(b_1b_2^* - b_3b_4^*)$	$\{-;z;z'\}$

[a] Notation is $\{P_\gamma; P_T; P_R\}$ where:
P_γ = polarisation of beam,
$L(\theta)$ = beam linearly polarised at angle θ to scattering plane,
C = circularly polarised beam;
P_T = direction of target polarisation;
P_R = component of recoil polarisation measured.

Table 3.1: Helicity and transversity representations of polarisation observables [54]. The * indicates complex conjugation.

where

$$T^{N_i^*}_{\pi N,\gamma N} = f^i_{\pi N}(E)\frac{\Gamma_{tot} M_i e^{i\Phi}}{M_i^2 - E^2 - iM_i\Gamma^{tot}} f^i_{\gamma N}(E)\overline{A^i}$$

The terms $f^i_{\pi N}(E)$ and $f^i_{\gamma N}(E)$ are the form factors of the N_i^* decays, Γ^{tot} is the total decay width, M_i is the pole mass of the resonance, and $\overline{A^i}$ is the strength of the $\gamma N \rightarrow N_i^*$ excitation. A choice must be made of which nucleon resonances to include in the sum in Equation 3.14. Only the thirteen resonances classified as four star states by the Particle Data Group play a role in the MAID analysis. By allowing a choice of which resonances to use in the fitting procedure, MAID is able to examine the effect of an individual resonance to the overall χ^2 of the fit. A total of 52 variables are needed for the parameterisation.

3.3.2 SAID

SAID [58, 59] is a multichannel analysis which makes no assumptions concerning which resonances are present. Contributing resonances are deterimined via a fit to the world database of πN scattering. The T-matrix is written as

$$T_{\gamma N,\pi N} = A_I(1 + iT_{\pi N,\pi N}) + A_R T_{\pi N,\pi N} \tag{3.15}$$

where A_I is the background term and A_R is the resonant term. The background consists of pseudoscalar Born terms and the exchange of ρ and ω vector mesons [55]. The resonant term A_R is a function of the pion and photon momenta k_0 and q_0, the angular momentum l, and the pion energy E_π

$$A_R = \frac{m_\pi}{k_0}\left(\frac{q_0}{k_0}\right)^l \sum_{n=0}^{N} p_n \left(\frac{E_n}{m_\pi}\right)^n$$

where p_n is a free parameter. After determining p_n, the full amplitude of Equation 3.15 is fit near a resonance position to obtain the resonance properties.

3.4 Summary

The process of pseudoscalar meson photoproduction is described by four complex reaction amplitudes which contain the properties of the nucleon resonance spectrum. The amplitudes can be written as a sum of multipoles with distinct

assignments of angular momentum, parity, and isospin. Sixteen polarisation observables provide experimentally measurable constraints for these amplitudes. Data are interpreted with reaction models in the form of partial wave analyses, which separate resonant and background production mechanisms and extract the properties of resonances. This analysis is still model dependant, however, measurement of eight suitably chosen observables enables a 'complete experiment' and will largely eliminate model ambiguity in the amplitude extraction. Current and planned experiments will measure the required set of double polarisation observables across a broad kinematic range spanning the resonance region. The recoil polarisation data analysed for this thesis provide a unique and necessary input to the current world effort.

Chapter 4

Previous Measurements of C_x

4.1 Experimental Setup

The previous measurement of C_x in the MAMI energy region was performed in 2002 in Hall A at Jefferson Lab [60] (Figure 4.1) for the reaction $\gamma p \rightarrow p\pi^0$. Circularly polarised photons with a maximum energy of 4.1 GeV were produced by impinging a 30μA 70% polarised electron beam on a copper radiator, with the resulting photon polarisation calculated as a function of energy. The helicity of the electron beam, and hence the photon beam, was flipped at a rate of 30 Hz. The photon beam interacted with a 15 cm long liquid hydrogen target located 73 cm downstream from the radiator.

The detector system used was the High Resolution Hadron Spectrometer [61]. In contrast to MAMI, the photon beam was not energy tagged, and thus had to be inferred from kinematic considerations. The spectrometer was first set at a particular lab angle with respect to the target. The choice of lab angle fixes the momentum of recoiling protons deflected by the magnetic field of the spectrometer into the detector stack (Figure 4.2), and thus each alignment corresponds to a specific photon energy and center of mass angle.

Vertical Drift Chambers were used to measure scattering angles, momentum, and the vertex of the interaction. Čerenkov counters provided a veto for background $\pi^+ n$ events. The scintillators S1 and S2 were used for particle identification via time-of-flight, and a signal in both elements defined an event trigger. The scattering material is a series of five carbon plates giving a total thickness

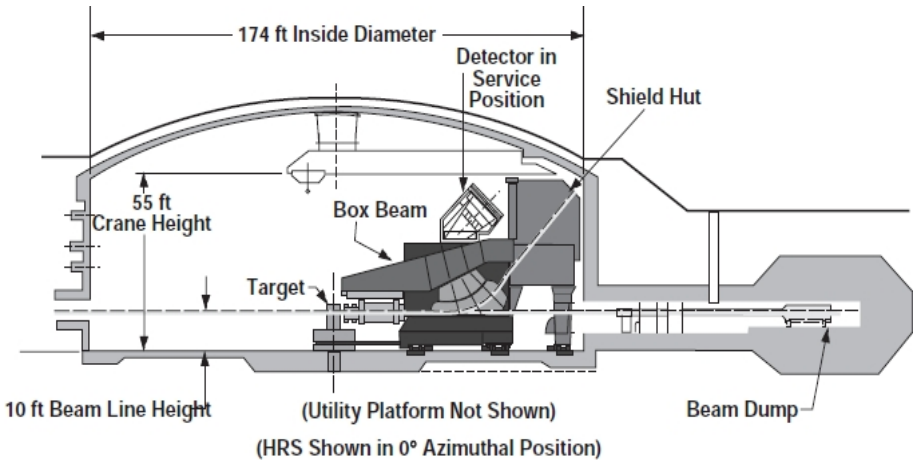

Figure 4.1: Schematic of the interior of Hall A at Jefferson Lab [61].

of 51.4 cm. The proton position entering and exiting the analyser was measured by straw chambers, allowing accurate determination of the scattering angles.

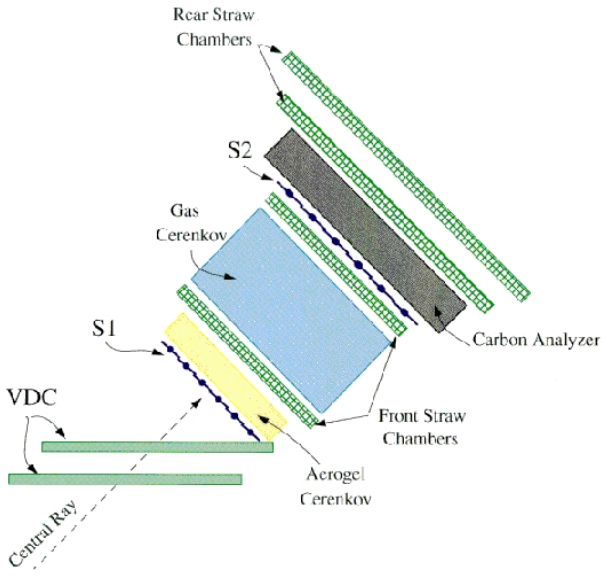

Figure 4.2: The detector stack, showing the Vertical Drift Chambers (VDC) and scintillators S1 and S2. Image from the Jefferson Lab Hall A Photo Archive.

4.2 Analysis

A cut of between 5° and 20° was imposed on the measured scattering angle, θ_{sc}. The lower bound rejected unscattered events in the analyser, while both the analysing power and efficiency decline sharply beyond the upper bound. The analysing power could be measured directly by removing the radiator and analysing elastic $\overrightarrow{e}p$ scattering, a reaction with a well established polarisation transfer. The resulting analysing powers, averaged over the accepted range of θ_{sc}, closely match the values obtained by McNaughton [62] (Figure 4.3). The analysing power of higher energy data were interpolated from previous measurements of ep elastic scattering.

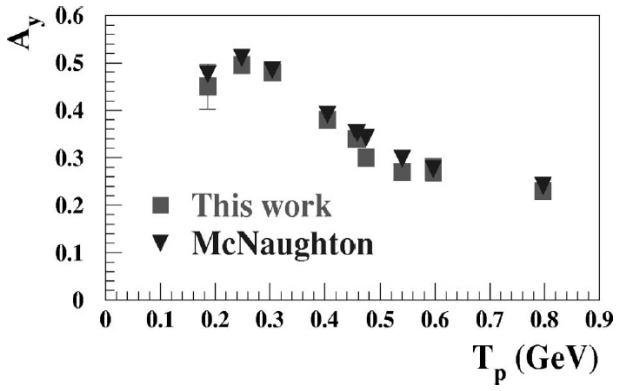

Figure 4.3: Angle averaged analysing power as a function of proton kinetic energy. The results are in close agreement with the McNaughton values [62].

The azimuthal scattering angle distributions allowed determination of transverse components of the proton polarisation at the polarimeter, $\hat{x}_{fpp}$ and $\hat{y}_{fpp}$, by considering the sum and difference of the helicity states, shown in Figure 4.4 (see Chapter 9 for an explanation of this procedure). It is important to note the effect of the magnetic field of the spectrometer on these components. The various magnetic fields of the quadrupole and dipole magnets of the spectrometer precess the proton spin through an angle χ given by

$$\chi = \frac{g-2}{2}\sqrt{\frac{1}{1-\beta^2}}\theta_{bend} \tag{4.1}$$

where g is the proton gyromagnetic ratio, β=v/c, and θ_{bend} is the bend angle of the spectrometer. The polarisation components at the target are thus rotated

upon reaching the polarimeter. This rotation can be calculated from a 3×3 spin transport matrix which depends on the angle and momentum of the proton trajectory through the spectrometer. The precession of the proton spin mixes the $x, y,$ and z components of the spin at the *target* into $\hat{x}_{fpp}$ and $\hat{y}_{fpp}$ by amounts given by the matrix elements of the transport matrix S_{ij}. The azimuthal scattering distribution at the polarimeter therefore enables determination of the spin transfer observables C_x, C_z, and the induced polarisation P as measured at the target. The absence of a magnetic field at MAMI to precess the proton spin prevents measurement of C_z.

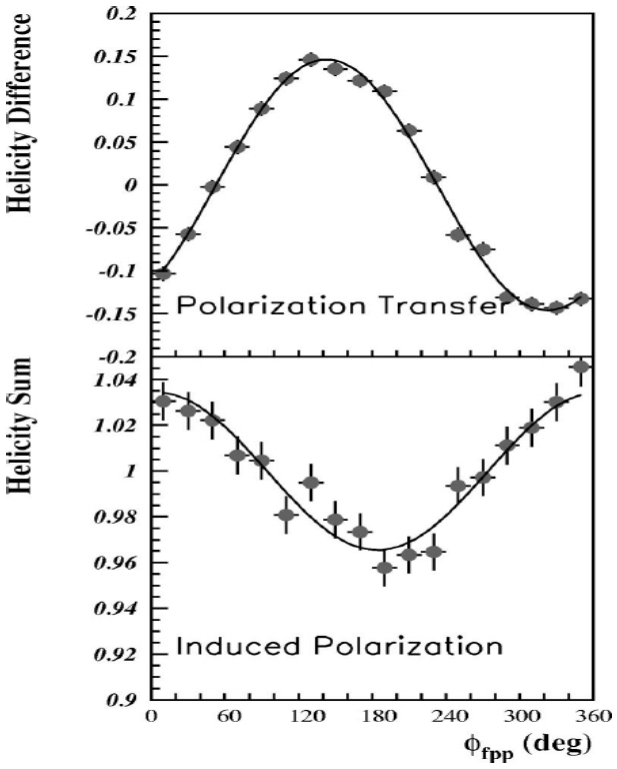

Figure 4.4: Sum and difference of helicity states for 0.86 GeV protons at θ_{CM}=135°.

Reference Frames

In the present discussion of the reaction reference frames, the following conventions apply: the centre of mass frame is distinguished from the lab frame by

the subscript c.m., while primed (') axes refer to the frame in which the recoil polarisation is measured. In the centre of mass frame, the axes are

$$\hat{z}_{c.m.} = \hat{k}_{\gamma}, \qquad \hat{y}_{c.m.} = \frac{\hat{z}_{c.m.} \times \hat{k}_{\pi^0}}{\left|\hat{z}_{c.m.} \times \hat{k}_{\pi^0}\right|}, \qquad \hat{x}_{c.m.} = \hat{y}_{c.m.} \times \hat{z}_{c.m.} \tag{4.2}$$

where $\hat{k}_{\gamma}$ and $\hat{k}_{\pi^0}$ refer to unit vectors in the direction of the incoming photon and outgoing pion respectively, while the polarisation axes in the c.m. frame are

$$\hat{z}'_{c.m.} = \hat{k}_{\pi^0}, \qquad \hat{y}'_{c.m.} = \hat{y}_{c.m.}, \qquad \hat{x}'_{c.m.} = \hat{y}'_{c.m.} \times \hat{z}'_{c.m.} \tag{4.3}$$

The observables P, C_x, and C_z listed in Chapter 3 were defined with respect to these axes.

The coordinate system used in the Hall A measurement, shown in Figure 4.6, was defined in the *lab* frame as

$$\hat{z}' = \hat{k}_{proton}, \qquad \hat{y}' = \frac{\hat{k}_{\gamma} \times \hat{k}_{\pi^0}}{\left|\hat{k}_{\gamma} \times \hat{k}_{\pi^0}\right|}, \qquad \hat{x}' = \hat{y}' \times \hat{k}_{\pi^0} \tag{4.4}$$

where $\hat{k}_{proton}$,is a unit vector in the direction of the recoil proton. Note that this coordinate system is left-handed. This choice of axes effectively rotates $\hat{z}'_{c.m.}$ and $\hat{x}'_{c.m.}$ around $\hat{y}'_{c.m.}$, as depicted in Figure 4.5. The axes $\hat{x}'$ and $\hat{z}'$ are each a mixture of $\hat{x}'_{c.m.}$ and $\hat{z}'_{c.m.}$, while $\hat{y}'_{c.m.}$ is unchanged. Consequently, the transfer observables measured with respect to the axes defined in Equation 4.4 are in fact a mixture of C_x and C_z as listed in Chapter 3.

4.3 Results

Figures 4.7-4.9 display the results for P, C_x, and C_x as a function of photon energy for several values of the centre of mass angle. The solutions from several partial wave analyses are compared to the data. The small uncertainties in the reported values were achieved due to the accurate measurement of the scattering angles from the straw chambers and the high electron beam current. Because the resulting photon beam was not energy tagged, the photon flux was not limited by the electronic readout rate of a tagging system, enabling an electron beam current 3 orders of magnitude higher than MAMI. The kinematic coverage of the

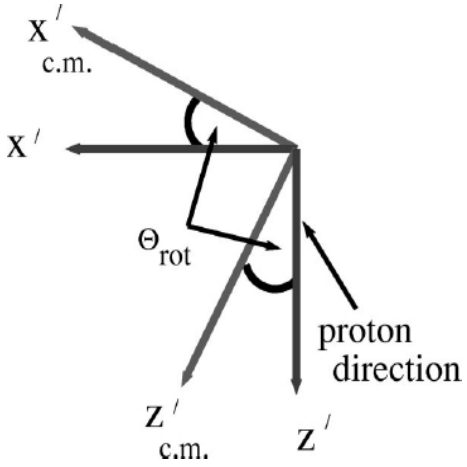

Figure 4.5: The frame in which the recoil polarisation is measured is a rotation of the primed centre of mass frame around $\hat{y}'_{c.m.}$.

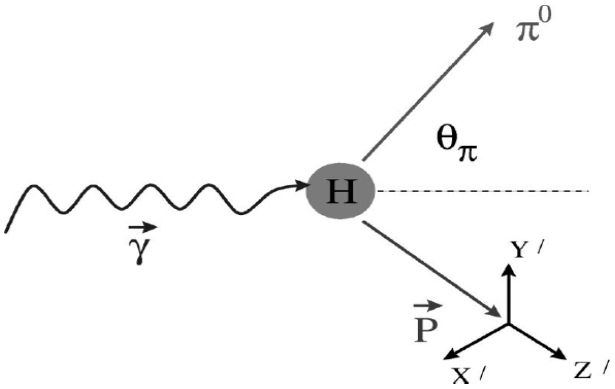

Figure 4.6: Schematic of the reaction in the lab frame [60]. The choice of axes used to measure the recoil polarisation is a left-handed coordinate system defined in terms of the outgoing proton momentum $\overrightarrow{P}$, the photon momentum $\overrightarrow{\gamma}$, and the pion momentum.

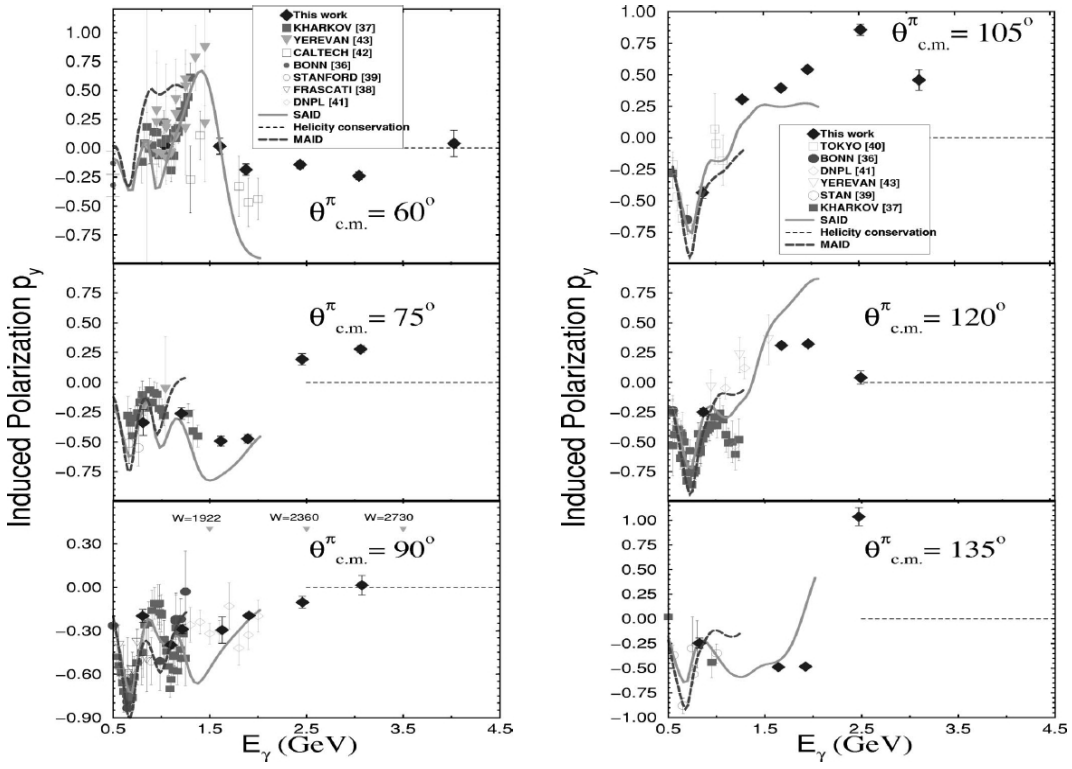

Figure 4.7: Results from Hall A for the recoil observable P [60].

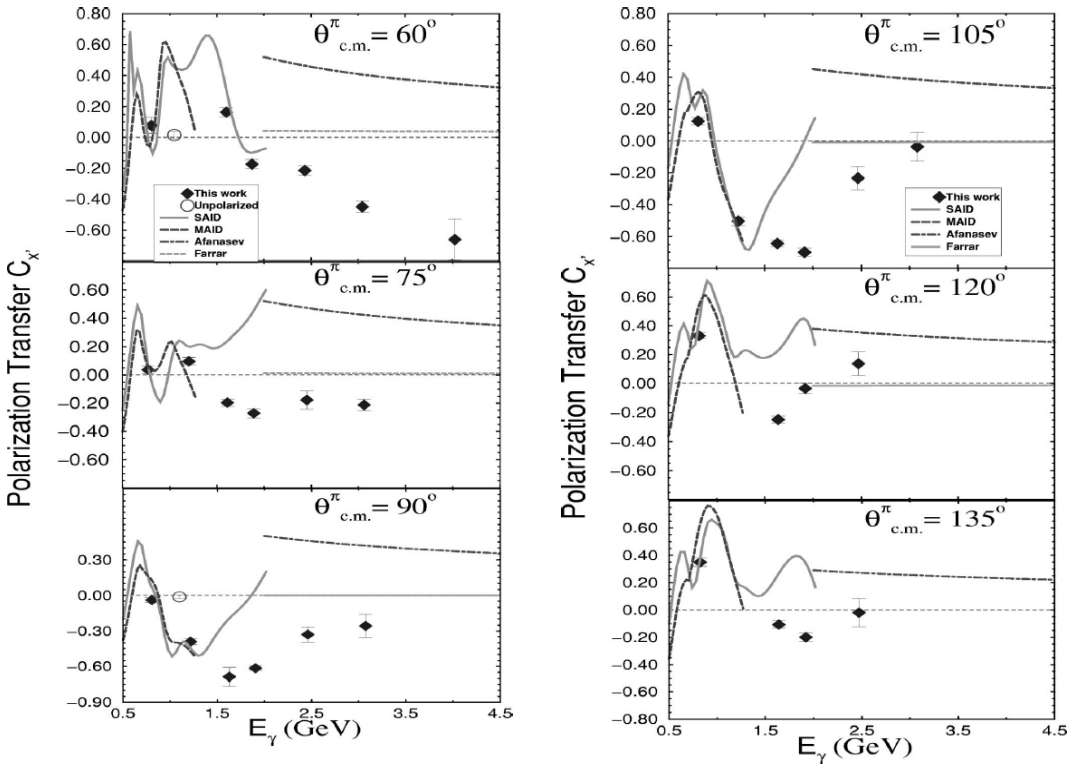

Figure 4.8: Results from Hall A for the beam-recoil observable C_x [60].

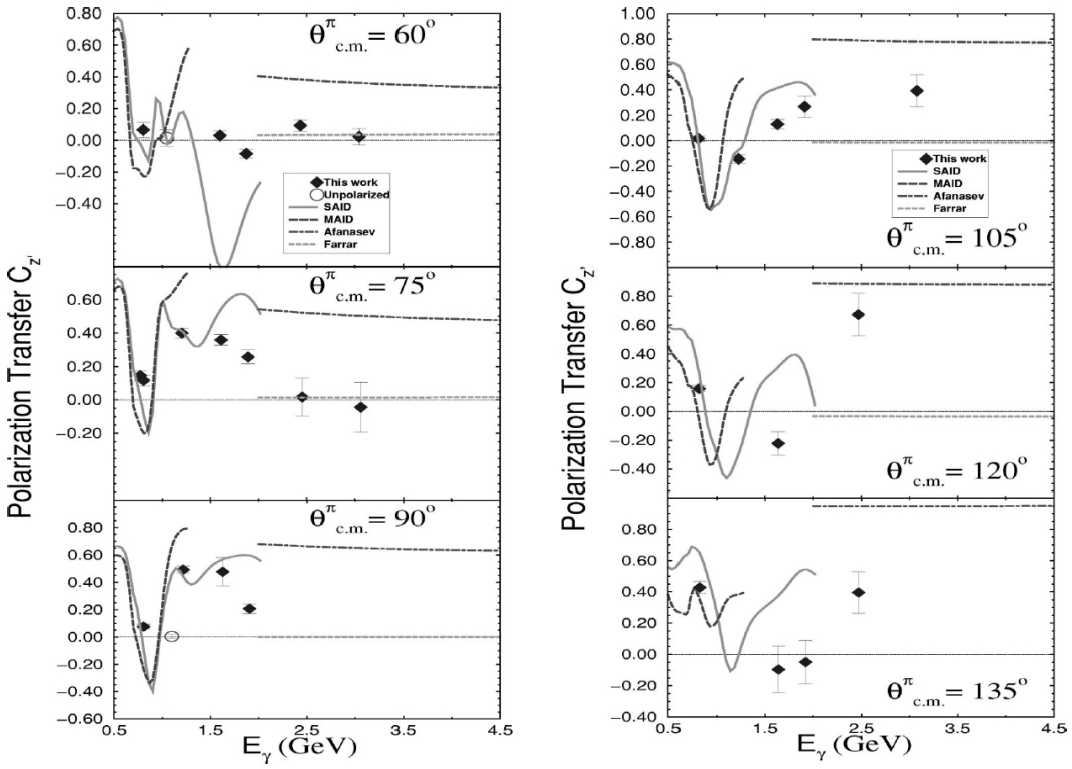

Figure 4.9: Results from Hall A for the beam-recoil observable C_z [60].

Hall A setup is limited by the need to shift the position of the spectrometer for each combination of photon energy and center of mass angle.

Up to 1.4 GeV E_γ, the maximum energy achieved at MAMI, only one or two data points have been measured for each reported centre of mass angle. The nearly 4π solid angular coverage of the Crystal Ball and recoil polarimeter at MAMI enables simultaneous data taking across the entire phase space covered by the detector system. The new values of C_x will provide a check of existing measurments and will greatly expand the the available data set in the 0.4-1.4 GeV E_γ range.

Chapter 5

Experimental Apparatus

The experimental work for this thesis took place in September-October 2008 at the Mainz Microtron (MAMI) at Johannes Gutenberg Universität in Mainz, Germany (Figure 5.1).

MAMI [63, 64] accelerates polarised electrons to an energy of 1.5 GeV, which are then incident on a thin metal radiator, producing a beam of Bremsstrahlung photons. The photon energy is determined by momentum analysing the recoiling electrons in the Glasgow Photon Tagging Spectrometer. The photon beam impinges on a liquid hydrogen target, yielding the photoproduction reactions $\gamma p \rightarrow p\pi^0$ and $\gamma p \rightarrow p\eta$. In the processes of interest, the mesons subsequently decay electromagnetically to two photons, and the recoiling protons scatter in the Edinburgh Recoil Polarimeter. Surrounding the target is the Particle Identification Detector, which provides a ΔE signal for charged particles. All reaction products are detected in the Crystal Ball and TAPS detectors, which are highly segmented calorimeter arrays. This chapter summarises the technical parameters of the accelerator, detectors, and data acquisition.

5.1 MAMI

5.1.1 Design

By the mid 1970's, the use of pulsed electron accelerators in nuclear physics experiments was well established. All such experiments detected only one final state particle, since measuring multiple reaction products would have been complicated by a high background resulting from uncorrelated events being detected within

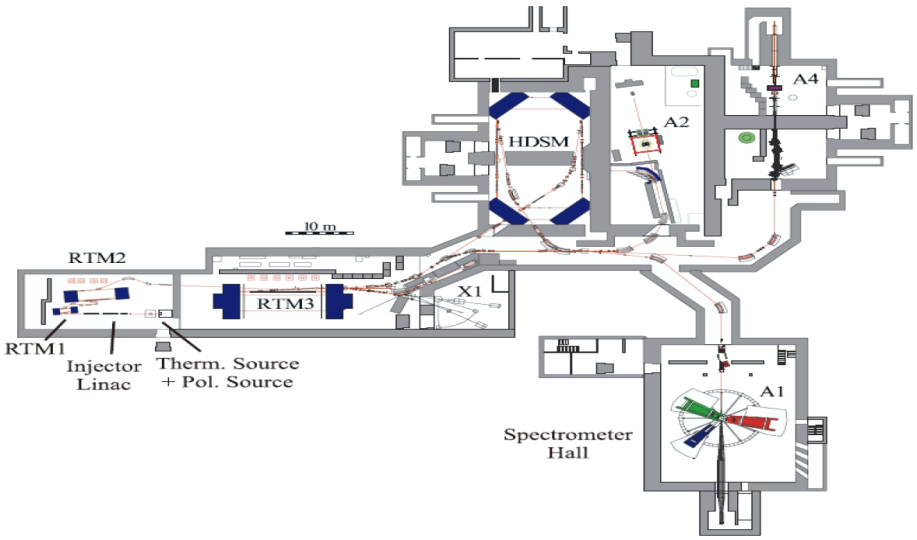

Figure 5.1: Layout of the MAMI facility. A series of microtrons (RTM1, RTM2, RTM3, HDSM) accelerate the electron beam, which is then delivered to one of four experimental halls (X1, A1, A2, and A4). Image from [65]

the timing resolution of the apparatus [66, 67]. This limitation could be overcome by reducing the time interval between beam pulses; new high duty-factor accelerators that produce continuous beams were necessary to reduce the probability of random coincidences.

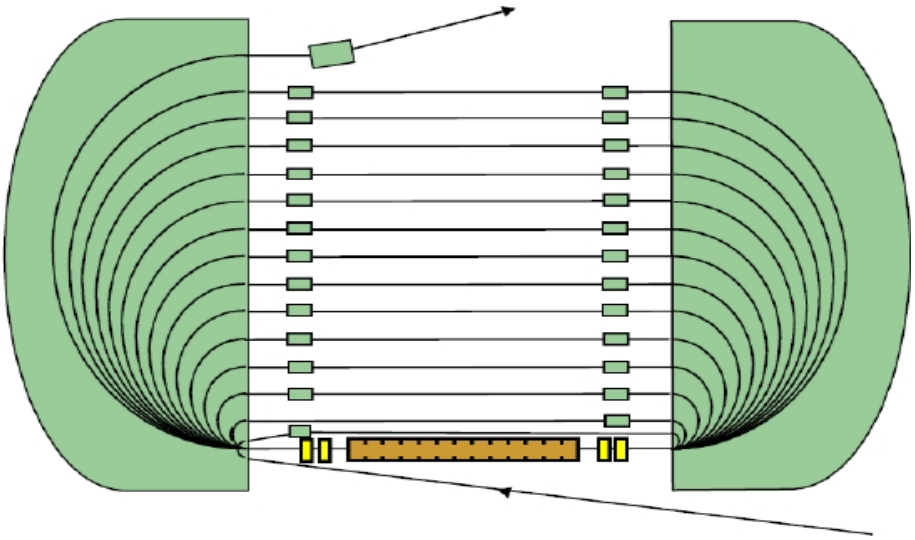

Figure 5.2: Basic design of a racetrack microtron. Image from [68].

A new accelerator design known as the racetrack microtron (RTM) was developed to provide this capability (Figure 5.2). A continuous wave linear accelerator (linac) is placed between two D-shaped magnets. An electron beam traverses the linac multiple times as it is recirculated by the field of the dipoles in increasingly larger orbits, gaining energy with each pass. This process continues until a maximum energy has been reached and the beam is ejected.

MAMI was initially designed as a series of RTMs with the goal of producing an 855 MeV electron beam. Three separate RTMs were planned in order to keep the magnet size and the number of recirculation tracks manageable [69]. At the injection stage of the microtron, a longitudinally polarised electron beam is produced via photoemission by illuminating a strained GaAs crystal with a circularly polarised Ti:Sapphire laser [70]. A linac injects the electron beam at 3.5 MeV into the first RTM, where it is ramped up to 14 MeV. The beam attains an energy of 175 MeV after 51 turns in RTM2 before reaching the desired energy of 855 MeV in RTM3, after which it can be delivered to one of the three experimental halls. The first two stages are referred to as MAMI A, and the entire configuration, compeleted in 1990, is known as MAMI B.

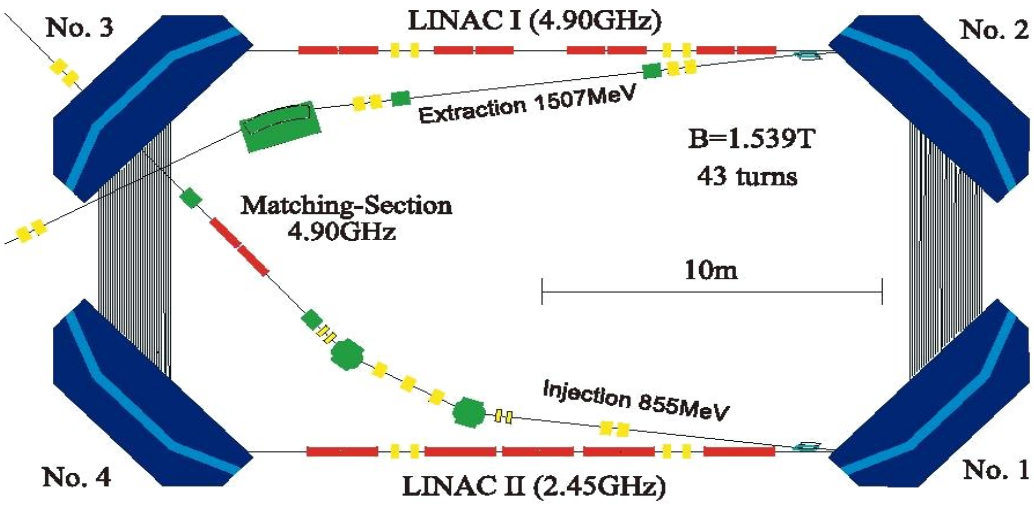

Figure 5.3: Schematic of the Harmonic Double Sided Microtron, with the four dipole magnets in blue. Image from [65]

In the late 1990's, a proposal to increase the beam energy to 1500 MeV was accepted. Adding a fourth RTM was impractical, as each end magnet would have

required 2400 tons of iron [65]. A modified RTM design comprising two linacs and four smaller 90° dipole magnets was chosen instead (Figure 5.3). One linac is operated at 4.90 GHz, while the second linac is driven at 2.45 GHz in order to minimise longitudinal defocussing due to phase shifts in the linac frequencies. This led to the system being named the Harmonic Double Sided Microtron. In December 2006, the newly christened MAMI C successfully delivered a 1508 MeV electron beam.

5.1.2 The Polarised Photon Beam

Experiments in the A2 hall do not directly use the beam from MAMI to induce reactions. Instead, the electron beam impinges on a thin metal radiator to produce photons via bremsstrahlung. Due to the polarisation of the incident electron beam, the resulting photon beam can be either circularly or linearly polarised. If the radiator has an amorphous atomic substructure, bremsstrahlung results in photons with cicular polarisation. The degree of polarisation can be calculated directly from Quantum Electrodynamics by

$$P^{\odot} = \frac{P_{MAMI} \times E_{\gamma} \times (E_{MAMI} + \frac{1}{3}(E_{MAMI} - E_{\gamma}))}{E_{MAMI}^2 + (E_{MAMI} - E_{\gamma})^2 - \frac{2}{3}E_{MAMI} \times (E_{MAMI} - E_{\gamma})} \tag{5.1}$$

where E_{γ} is the photon energy and E_{MAMI} is the MAMI energy of 1508 MeV. The upper limit of P_{MAMI} is the maximum polarisation of the MAMI electron beam. The helicity of the photon beam was switched at a frequency of 1 Hz during production running by changing the polarity of the voltage at the source of the polarised Ti:Sapphire laser which produces the electron beam.

Conversely, materials with a lattice atomic arrangement, such as a diamond, can produce linearly polarised photons by a process known as coherent bremsstrahlung. This occurs when the lattice vector is properly aligned with the polarisation vector of the incoming electron beam. The data collected for this thesis used both circularly and linearly polarised photons produced from a 12 μm copper foil and a diamond radiator respectively. This analysis is only concerned with the data taken with circular photon polarisation.

5.2 Glasgow Photon Tagger

Bremsstrahlung photons produced from a mono-energetic electron beam are emitted with a range of energies. The Glasgow tagger [71, 72] determines the energy of each outgoing photon using a magnetic spectrometer and the Focal Plane Detector (FPD), a series of 353 plastic scintillators (Figure 6.4). An electron with

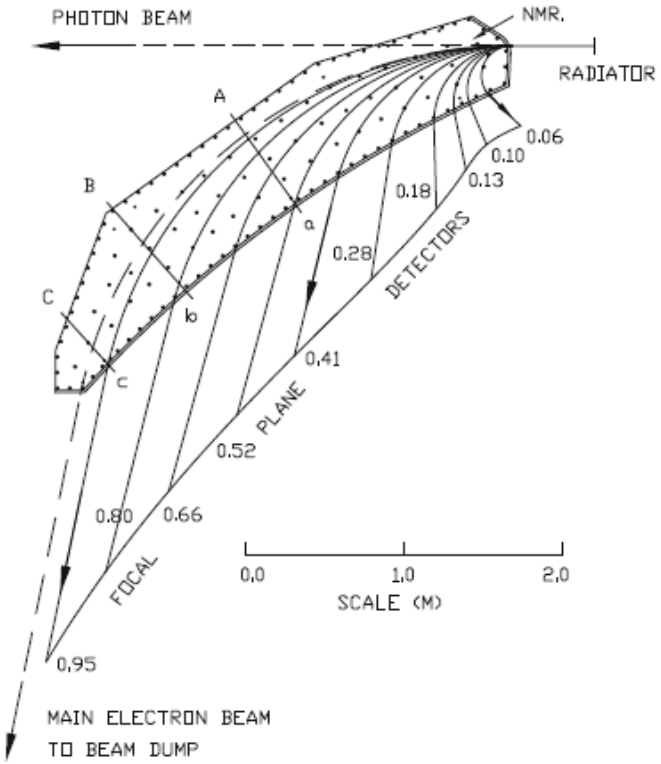

Figure 5.4: The tagger system. Electrons encounter the magnetic field of the spectrometer after traversing the radiator. The position of a hit in the Focal Plane Detector determines the electron energy. The trajectories of electrons with various energies, expressed as a fraction of the beam energy, are shown above. Image from [72]

intial energy E_{beam} undergoes bremsstrahlung, producing a photon of energy E_γ. The scattered electron is then momentum analysed in the 1.8 T magnetic field of

the spectrometer and detected in the FPD, where its energy E_f is inferred from the position of the hit in the focal plane. The photon energy is then 'tagged' by the energy of the scattered electron according to

$$E_\gamma = E_{beam} - E_f \tag{5.2}$$

The elements of the FPD are 80 mm long, 2 mm thick, and vary in width from 9-32 mm, with narrower elements placed further along the focal plane to keep the energy width of each channel constant at $\sim$ 4 MeV. The scintillators are arranged so that neighboring elements overlap by about half of their width, and this overlap region defines each channel. Consequently, a tagging electron produces a hit in adjacent scintillators, a requirement which reduces random coincidences from multiply scattered electrons. Each EJ200 scintillator is wrapped in aluminised Mylar to reduce cross talk and connected to a Hamamatsu Photonics R1635 photomultiplier tube (PMT). The PMTs are shielded from stray magnetic fields by 0.7 mm steel plates installed on either side. This system is capable of processing a flux of $10^8\gamma$'s/second, tagged over an energy range of 80-1400 MeV.

5.3 Crystal Ball

The Crystal Ball [73, 74, 75] calorimeter was designed and built at SLAC in the 1970s to study the newly discovered J/ψ meson. After use at DESY and Brookhaven National Lab, the Crystal Ball was transferred to its current location in the A2 hall in Mainz in 2002.

5.3.1 Geometry

The detector is composed of 720 NaI(Tl) crystals arranged on the surface of an icosahedron, a regular 20 sided polyhedron (Figure 5.5). The crystals are grouped in 4 minor triangles of 9 elements on each of the 20 major triangular faces to make the shape as spherical as possible. Due to its initial use in colliding beam experiments, 48 crystals were removed to create two entry points. The remaining 672 crystals cover a solid angular region of 93% of 4π. The crystal shape is a truncated pyramid (Figure 5.6) 40.6 cm long, corresponding to 15.7 radiation lengths for photons. Equilateral triangles of sides 5.1 cm and 12.7 cm form the base and apex respectively. The crystals are optically isolated by wrapping each

element in aluminised mylar and viewed with their own SRC L50 B01 PMT. They are arrayed in two hermetically sealed hemispheres of inner radius 25.3 cm and outer radius 66.0 cm to preserve the hygroscopic crystals.

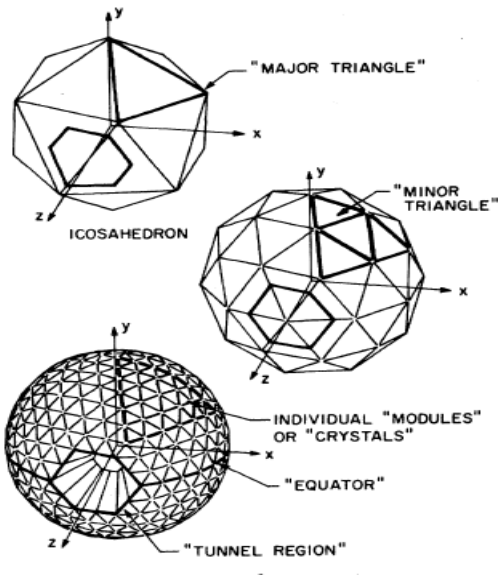

Figure 5.5: The geometry of the Crystal Ball. Image from [74]

Photons entering the calorimeter dominantly interact by producing electron-positron pairs. These particles then produce additional photons via bremsstrahlung or positron annihilation with another electron, and the process repeats. Such electromagnetic showers typically spread over a group of several crystals. An algorithm forms a cluster based on a crystal which fired by checking the energy of all adjacent crystals. A crystal is included in the cluster if it recorded an energy greater than the 2 MeV threshold, and the algorithm then checks the neighbours of this newly included crystal, and so on. The measured energy is then the sum of the energy of each crystal in the cluster, and the threshold for forming a cluster was set at 30 MeV. The position of the hit $\overrightarrow{\mathbf{r}}$ is determined from the center of mass of the inidividual crystal energies

$$\overrightarrow{\mathbf{r}} = \frac{\sum_N \overrightarrow{\mathbf{r}_i}\sqrt{E_i}}{\sum_N \sqrt{E_i}} \tag{5.3}$$

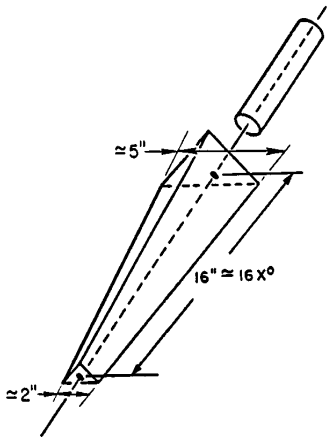

Figure 5.6: The shape of each NaI crystal. Image from [75]

where $\overrightarrow{\mathbf{r}_i}$ and E_i are the position and energy of the i^{th} crystal. The full geometry achieves photon resolutions of $\frac{\sigma_E}{E} \approx \frac{1.7\%}{E(GeV)^{0.4}}$ in energy and angular resolutions of $\sigma_\theta \sim 2-3^\circ$ in the polar angle and $\sigma_\phi \sim 2/\sin\theta$ in the azimuthal angle.

5.4 Liquid Hydrogen Target

The target cell is a cylinder 4.8 cm long and 4.0 cm in diamater contained in a 125μm thick kapton housing at the center of the Crystall Ball. During the experiment, the system was kept at a pressure of 1080 mBar and a temperature of 20 K. Gaseous hydrogen from a storage tank is compressed, liquified, and then supplied to the target. During operation, the temperature is continually monitored and adjusted by addition of more liquid or evaporation using two 4W heaters.

5.5 Particle Identification Detector (PID)

Surrounding the target is the PID [76], a segmented barrel of 24 plastic scintillators 108 mm in diameter (Figure 5.7). Each 500 mm long, 4 mm thick element is connected via a shaped perspec lightguide to a Hamamatsu H3164-10 PMT at the upstream end.

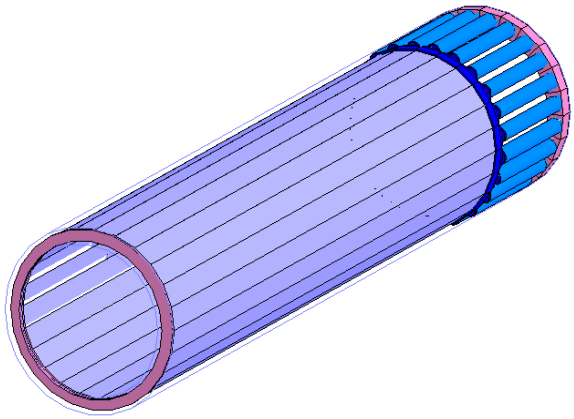

Figure 5.7: The Edinburgh PID.

As a charged particle traverses the scintillator, it deposits a small amount of energy ΔE. A hit in the PID is then correlated with a hit in the Crystal Ball if the measured azimuthal angles are within 15°, the angle subtended by each PID element. The ΔE from the PID can then be compared to the full particle energy measured in the Crystal Ball, allowing identification of protons and charged pions. The installation of the polarimeter required a new method of particle identification using the Crystal Ball and the PID, discussed in Section 8.2.

5.6 Recoil Polarimeter

Recoiling protons are deflected by the polarimeter into the Crystal Ball or TAPS. The analysing material is a 20.75 cm long graphite cylinder with inner radius 6.95 cm and outer radius 9.25 cm surrounding the PID together with a 7.25 cm long disc with inner radius 2.00 cm and outer radius 9.25 located 35 cm upstream from the target (a schematic of the setup is shown in Chapter 8). These were contained in a 0.5 cm thick polyvinyl support pipe with a 20 cm diameter oriented along the beam axis. A Geant4 rendering of the experimental setup is shown in Figure 5.8. The liquid hydrogen target, shown in yellow, is located at the center of the Crystal Ball. Surrounding the target is the PID (blue) and the graphite polarimeter (magenta), with the upstream cap covering the exit hole leading to TAPS.

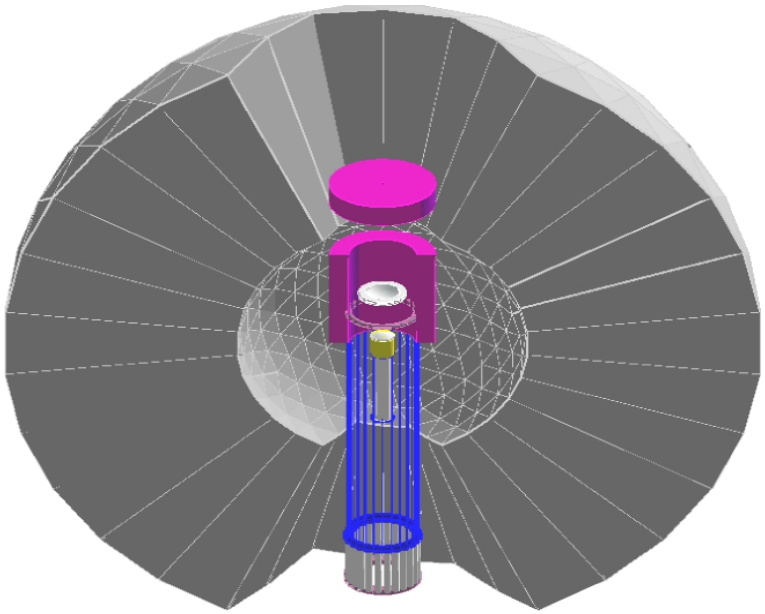

Figure 5.8: The experimental setup. The liquid hydrogen target (yellow cylinder) is surrounded by the PID (blue) and the 2.25 cm thick graphite polarimeter. The upstream cap is 35 cm away from the target. The PID was flush with the upstream cap during data acquisition, however for this picture, the PID has been shifted for clarity.

5.7 The Two Arm Photon Spectrometer (TAPS)

The TAPS detector [77], an array of 384 BaF_2 crystals, covers the kinematically important region missed by the Crystal Ball due to the downstream opening (Figure 5.9).

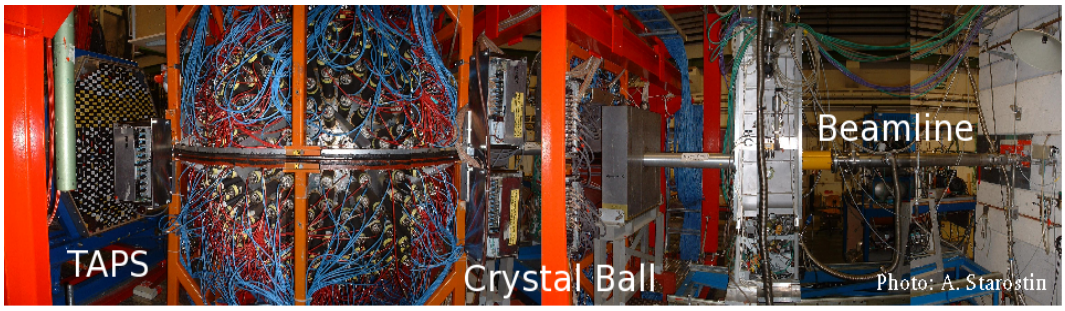

Figure 5.9: Photograph of the beamline, showing the Crystal Ball and TAPS. The photon beam is incident from the right.

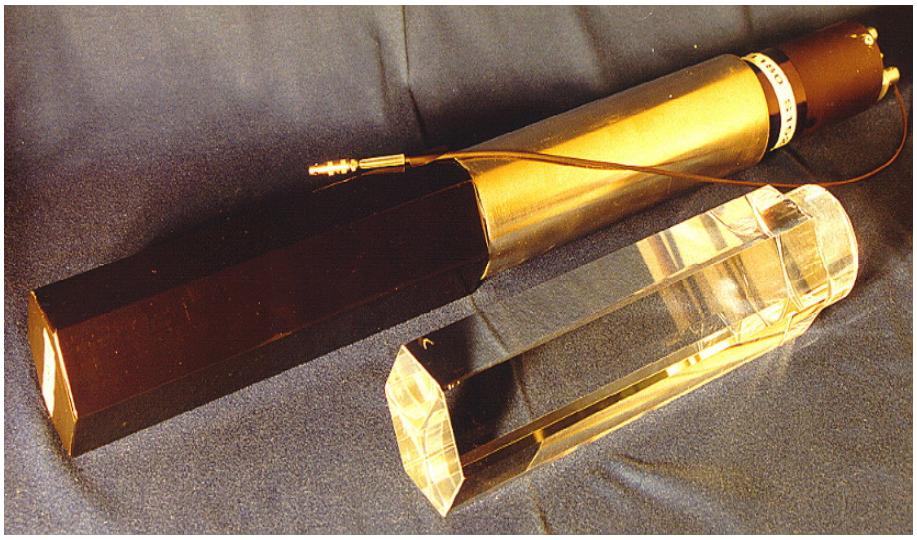

Figure 5.10: TAPS BaF_2 crystal.

Each 25 cm long crystal (12 radiation lengths) is read by a Hamamatsu R2059-01 PMT (Figure 5.10). A 5 mm NE102A scintillator read out via 2 wavelength shifting fibres is placed in front of each crystal face as a veto for charged particles, enabling identification from the ΔE-E method used with the Crystal Ball and PID

with an energy resolution σ_E of

$$\frac{\sigma_E}{E} \approx \frac{0.59\%}{E_\gamma(GeV)^{1/2}} \tag{5.4}$$

Additional features available from the TAPS detector system, but not used in this analysis, are time of flight measurements for neutral particles and pulse shape analysis. The latter technique exploits the scintillation response of BaF_2, which has a fast component (0.6 ns) and a slow component (620 ns), by comparing the former with the total light output to perform particle identification.

5.8 Data Acquisition

The scintillation light produced by a particle in a given detector element is collected by a photomultiplier tube, which outputs an electric pulse proportional to the energy measured in the detector. This signal is digitised using ADCs (analogue to digital converters), QDCs (charge to digital converters), and TDCs (time to digital converters) depending on the specific detector. A brief description of these electronic devices is given here. The calibration of each detector to convert the digitised output from these devices to useful physical quantities (energy, time) is discussed in Chapter 6.

5.8.1 Tagger Electronics

The readout from each of the 352 PMTs reading each focal plane detector element is fed to an amplifier/discriminator card. The PMT output signal is first amplified by a factor of 10 and then passed to a constant fraction discriminator chosen due to the small sensitivity of timing to the pulse height of the signal. The logic pulse output of the discriminator, accurately timed to the PMT output signal and therefore to the detected focal plane hit, is read by multi-hit CATCH TDCs based on the design used for the COMPASS experiment at CERN [78]. FASTBUS QDCs are used to record scalers.

5.8.2 Crystal Ball Electronics

Each Crystal Ball PMT output signal is first fed into an active splitter (Figure 5.11), which accepts input from groupings of 16 crystals. The splitter produces

three output branches for each input signal. One output branch is an analogue sum which can be used as a fast trigger based on the total energy measured in the detector. The second output is sent to multihit CATCH TDCs, which give a timing signal based on the timing of the pulse. The third output is read by flash ADCs which sample the pulse at a high frequency (40 MHz). The shape of the signal is not readout due to resulting effects on the deadtime of the detector. The ADCs calculate three integral values: the integral of the entire pulse over 1 μs, the integral over 100 nsec before the main pulse (known as the pedestal), and the integral over the first 300 nsec of the pulse (used to distinguish between overlapping events).

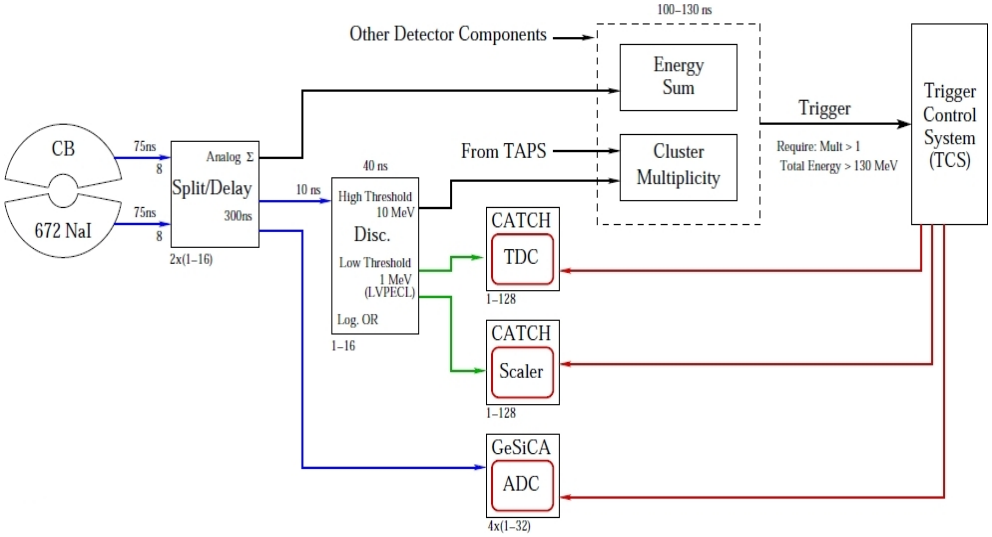

Figure 5.11: Schematic of the Crystal Ball electronics.

5.8.3 TAPS Electronics

The TAPS signal processing utilises the slow and fast scintillation components in the scintillator, with the charge and timing of these components measured separately. The signal from a TAPS PMT is sent to a constant fraction discriminator (CFD), which gives accurate timing of the pulse; two leading edge discriminators (LEDs), the outputs of which are used for flexible event selection; and four charge-to-amplitude converters (QACs) [79]. The CFD gives the main timing signal for the QACs, which integrate over the total pulse (2 μs) and the

fast component (20 ns). This is done with both a high and low gain in order to perform pulse shape analysis.

5.8.4 Trigger

This experiment used an energy sum of 150 MeV to trigger the data acquisition system to save an event. The energy sum was applied to an analogue sum of all the output signals in the Crystal Ball. For the latter run period in the experiment this was increased to 300 MeV to further reduce dead time in the data acquisition and to improve the event rate in the region of interest.

5.9 The A2 Simulation

A detailed simulation of the detector geometry in the Geant4 program was used extensively in this analysis. The Geant4 toolkit [80] is based on a suite of C++ classes which model the passage of a particle through various materials. A phase space event generator provided a file of events containing 4-vectors of the photon beam, recoil nucleon, and the two decay photons of a given photoproduction reaction, as well as the vertex of the interaction in the target. This information could then be input to the Geant4 simulation, which tracks the passage of each particle. As a particle traverses a detector, the deposited energy is calculated in a series of steps according to databases of measured cross-sections of the various physics processes. This analysis required supplemental routines written ad-hoc to simulate the polarised scattering of protons in the polarimeter, which are described in Chapter 7.

Chapter 6

Detector Calibrations

Each of the detectors used in the experiment required a calibration to convert the digital electronic output to measurements of time and energy. Much of this work was done by collaborators with responsibility for particular detector components. The calibration procedures for each detector are described here.

6.1 Timing Alignments

Accurate timing of detector hits is essential to the analysis of recorded data. Detector times are critical to determining the tagger beam energy of each event and to the clustering algorithms in the Crystal Ball and TAPS. Timing alignments for the Crystal Ball, TAPS, TAPS veto, and PID were done with the same procedure, so the process is illustrated by considering just the Tagger.

A relative time alignment is achieved by fitting a Gaussian to the Tagger coincidence time peak for each element in the focal plane (Figure 6.1). The calibrations of each element were then offset so as to align the means of each fit function at an arbitrary time, using the 0.117 ns/channel width of the TDCs. A window of 90-110 nanoseconds around the coincidence peak is then used to associate the tagger hit with an event.

Crystal Ball Time Walk Correction

The slow response time (250 ns) of NaI results in time walk effects in the recorded TDC times. Pulses with different heights cross the threshold of the leading edge discriminator at different times due to the longer rise time of the signal with the

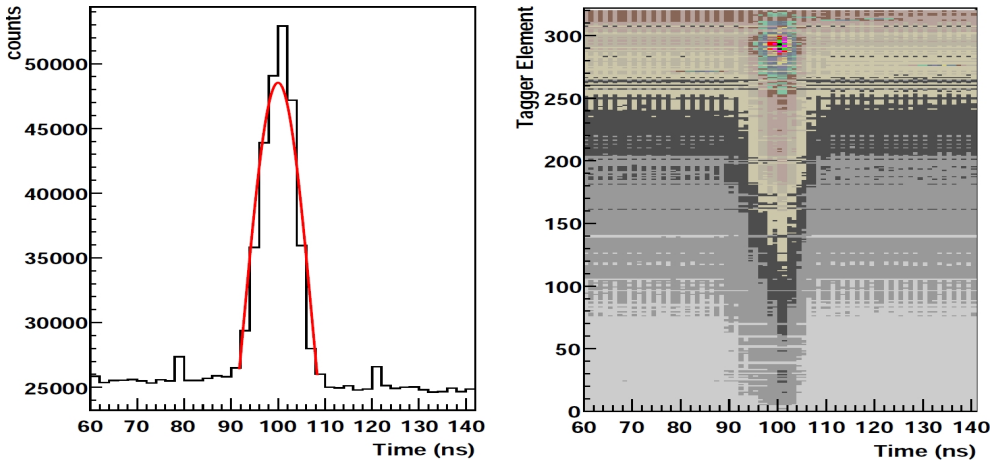

Figure 6.1: The time spectrum of each TDC was fit with a Gaussian around the coincidence peak (left). After calibration, the coincidence peaks are all aligned at a common time, chosen arbitrarily (right).

smaller magnitude. Figure 6.2 illustrates how a low energy pulse of height a will thus appear to have been detected at a later time than a more energetic pulse. A

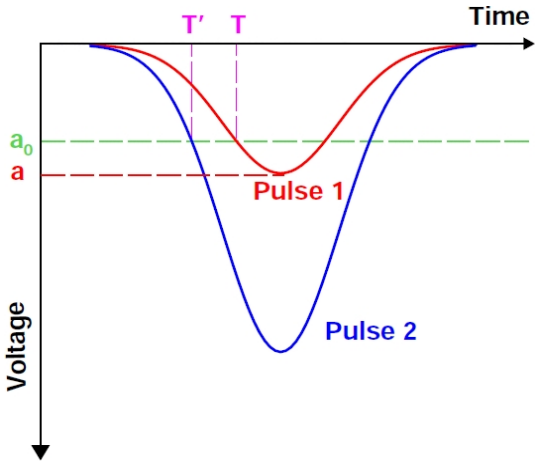

Figure 6.2: Pulses with different heights cross the discriminator threshold a_0 at different times, resulting in time walk.

corrected time T' can be calculated from the measured time T, the discriminator threshold a_0, and the rise time r

$$T' = T - r\sqrt{\frac{a_0}{a}} \tag{6.1}$$

The quantity ra_0 was determined by plotting energy as a function of time, and the correction was then calculated using Equation 6.1. The effect of the correction can be seen by plotting the energy of hits in NaI versus time, as shown in Figure 6.3.

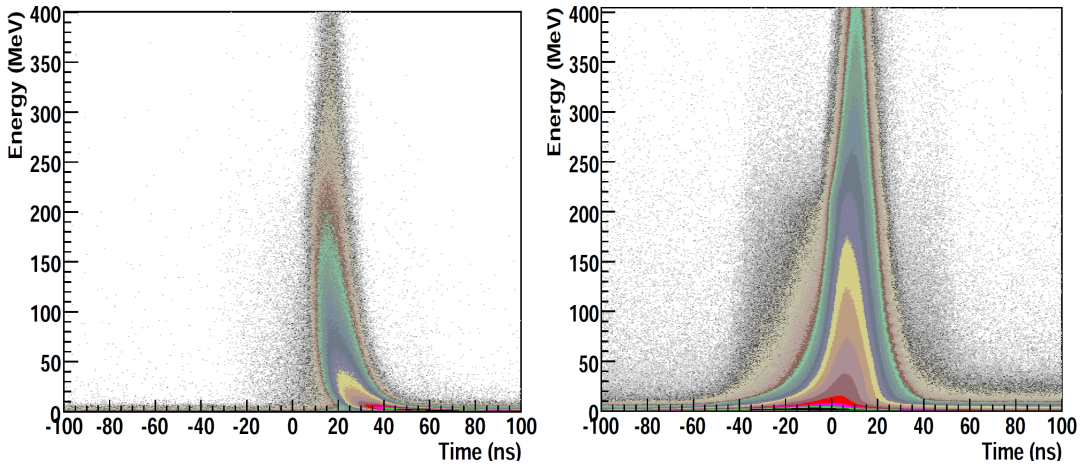

Figure 6.3: NaI energy vs. time without correction for time walk (left) and with the correction (right).

6.2 Photon Beam Tagger

6.2.1 Energy Calibration

Detailed measurements of the tagged photon energy were made after the recent Tagger upgrade [72]. This was done using the MAMI electron beam, the energy of which is known to within 140 keV [65], at seven energy values from 0.1952-1.3078 GeV. The bremsstrahlung radiator was removed so that a low current beam impinged directly onto the scintillators in the focal plane. The 1.834 T magnetic field used in standard tagging conditions was then varied so that incident electrons were detected in the small overlap region between neighboring channels, determining the hit position to within 5% of the channel width. For each beam energy, this scan was usually carried out over a range of 12 scintillators. By plotting the magnetic field strength versus the fractional channel number, the channel number hit corresponding to the standard 1.834 T magnetic field could

be interpolated. The beam energy was then plotted as a function of this channel number and fit with a linear function (Figure 6.4), assuming a uniform magnetic field. The correction factor shown in the bottom plot of Figure 6.4 was needed to account for non-uniformities in the magnetic field caused by the pole shim mounting screws. This was obtained using a simulation of the Tagger geometry with a uniform field. The calibration at each calibration point was then calculated and compared to the measured value. The difference between the two results defines the required correction.

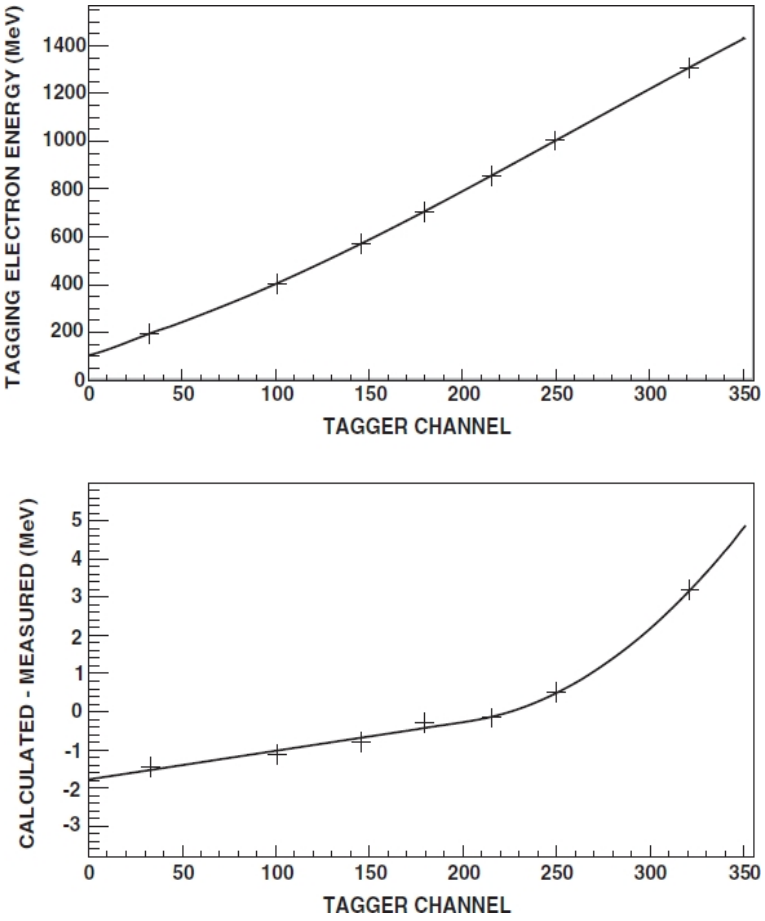

Figure 6.4: Tagger calibration from [72]. The top graph plots the channel number interpolated from the beam scan at the seven beam energies used for the calibration. The fit line gives the calibration assuming a uniform magnetic field. The bottom graph shows the correction due to the non-uniformity of the magnetic field.

6.2.2 Random Subtraction

Electrons detected in the tagger focal plane are identified as having emitted the photon for an event by means of a timing coincidence between the experimental trigger and the time of the tagger hit, shown in Figure 6.5. Tagger hits arriving in the 'prompt' window of 90-110 ns define the photon beam energy for recorded events. However, the prompt peak contains a significant background of random correlations from photons which do not pass the 3 mm collimator, photons which do not interact with the target, and electrons which undergo Møller scattering in the radiator. As it is not possible to decide which photon inside the prompt window caused the interaction in the target, a background subtraction must be made to reconstruct experimental observables using the correct photon momentum.

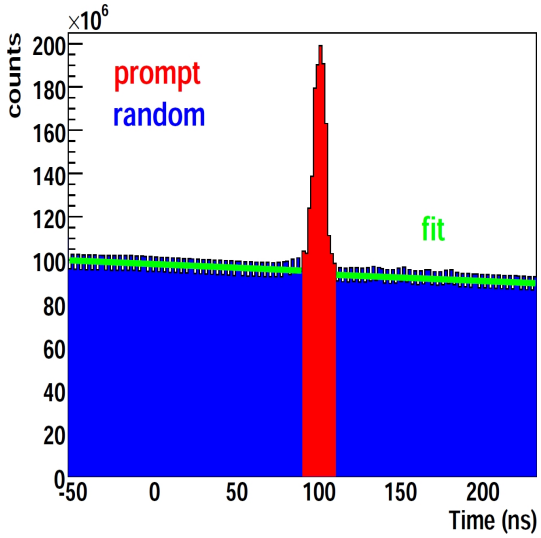

Figure 6.5: The prompt region (red) contains an uncorrelated background, which must be subtracted off. This is done by sampling the random region (blue) on either side of the coincidence peak. A linear fit to the random region (green) determines the background ratio in the prompt region.

The background contribution is quantified by sampling the 'random' region on either side of the prompt window. Reaction quantities which depend on the photon momentum are constructed separately for tagger hits in the prompt and random regions. The random contribution is then scaled and subtracted from the prompt contribution.

The scaling factor is calculated from linear fits to the random regions on either side of the prompt window in Figure 6.5. The integral of each fit function is then calculated over the appropriate range. The average of the two fits is then calculated and integrated over the prompt window. The scaling factor is given by the ratio of the prompt integral to the random integral. To optimise statistical accuracy, the random region was chosen to be as wide as possible, with a scaling factor of prompt/random=0.019.

6.3 Crystal Ball

The Crystal Ball energy was calibrated by collaborators at UCLA and the University of Mainz [81, 82].

The crystals were first gain matched prior to data taking. This was done using a ^{241}Am/^{9}Be source placed at the centre of the Crystal Ball. The americium decays through alpha emission

$$^{241}_{95}\mathrm{Am} \rightarrow ^{237}_{93}\mathrm{Np} + \alpha$$

The α particle then reacts with the beryllium to produce ^{13}C*, which decays via

$$^{13}\mathrm{C}^{*} \rightarrow ^{12}\mathrm{C}^{*} + n$$

The excited ^{12}C* decays to the ground state by emission of a 4.438 MeV photon, which is used to set the voltage gains for each crystal. A typical energy spectrum for a single crystal is shown in Figure 6.6. The neutron background was fit with an exponential, and the photon peak was fit with a Gaussian. This procedure thus defined a low energy calibration point for each crystal. This was repeated for each crystal, and the potentiometer at the base of each photomultiplier tube was adjusted so that the mean position occurs at the same channel number.

After the experiment, the crystals were calibrated at higher energies using the $\pi^0 \rightarrow 2\gamma$ reaction which satisfy several conditions. After calculating the invariant mass of the two detected photons $M_{2\gamma}$, events were selected if $|M_{2\gamma} - M_{\pi^0}|$ <30 MeV, where M_{π^0}=135 MeV. The photon beam energy was restricted to be less than 180 MeV in order to produce low energy pions, so that the decay photons had a large opening angle. This was imposed to ensure the decay photons were distributed as evenly as possible across all crystals. Furthermore, a minimum of

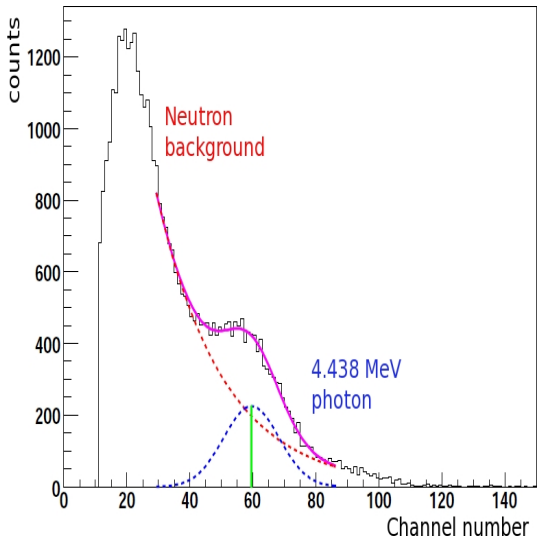

Figure 6.6: Gain matching using the americium/beryllium source. The fit to the full spectrum (magenta) is the sum of an exponential fit to the neutron background (red) and a Gaussian fit to the photon peak (blue). From [81].

70% of the energy of each photon cluster had to have been deposited in a single crystal, and the energy difference between the two clusters had to be less than 25% of the total detected energy. For a given crystal, $M_{2\gamma}$ was calculated and compared to M_{π^0}, and the gain was then scaled by the ratio $M_{2\gamma}/M_{\pi^0}$. Because the calibration depends on the gains of other crystals, the process was repeated until $M_{2\gamma}/M_{\pi^0} \approx 1$.

The clustering algorithm only includes crystals which measure energy above the hardware discriminator threshold of 2 MeV, so extended clusters can have non-negligible shower loss. Once the energy calibration is complete, a global energy scale factor must be determined to adjust the measured cluster energies so that the distribution of $M_{2\gamma}$ is centred on M_{π^0}. A separate scaling factor was calculated separately for each trigger condition for both the π^0 and η analysis. The values obtained vary from 1.051-1.070.

6.4 TAPS

The calibrations of the TAPS BaF_2 crystals and plastic veto shield were carried out by colleagues from the University of Giessen [68]

BaF_2 Calorimeter

The calibration method is similar to that of the Crystal Ball. Cosmic muons provided a reference energy to set the voltage gains of each crystal. The energy loss of muons in BaF_2 is known to be 6.4 MeV/cm, with a mean path length of 5.9 cm. Thus, muons passing vertically through TAPS will have an energy distribution centred at 37.7 MeV. The voltages of each crystal are adjusted so that the peak occurs at the same channel number. Due to the limited angular coverage of TAPS, the number of $\pi^0 \rightarrow 2\gamma$ decays where both photons are detected in TAPS is insufficient to perform the calibration. Rather, events with one photon detected in the Crystal Ball and the other photon detected in TAPS were selected, and the same procedure used to calibrate the NaI crystals was followed. Therefore, the Crystal Ball was calibrated before TAPS. An energy scaling factor of 1.1 was then applied to the TAPS crystals.

Veto

The plastic veto in front of the TAPS array was calibrated by plotting the energy deposited by protons in the scintillator ΔE against the full energy E detected in TAPS for both the simulation and data. Projections of ΔE were fit with Gaussians, and the mean position of the proton peak matched an ADC channel number to a simulated energy value.

6.5 PID

6.5.1 Azimuthal Alignment

The azimuthal alignment of the PID was done by colleagues at the University of Edinburgh.

Events which contained a cluster of just one crystal in the Crystal Ball were selected. Of these events, only those with one PID hit were used in the alignment. The azimuthal position of each of the 24 PID elements was determined by comparing the detected ϕ angle in the Crystal Ball with the coincident PID hit (Figure 6.7(a)). The ϕ projection of each element was then taken, an example of which is shown for PID element 8 in Figure 6.7(b). The spectrum shows a sharp coincidence peak at $\sim$100° and a second, broader peak 180° apart. This secondary

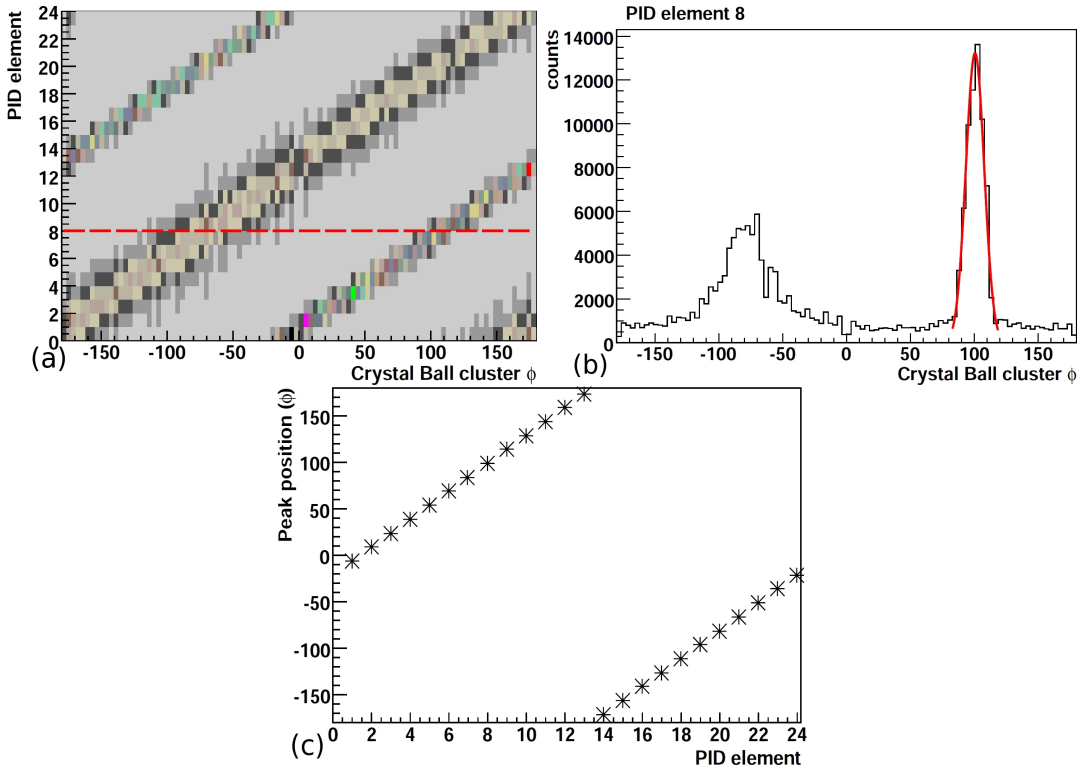

Figure 6.7: (a) The azimuthal alignment of the PID is achieved by plotting the ϕ angle of clusters in the Crystal Ball against the coincident PID element number. (b) The ϕ projection for PID element 8. The peak has been fit with a Gaussian, the mean of which is the azimuthal position of the element. (c) The result of the alignment.

peak arises from reactions such as $\gamma p \rightarrow \pi^+ n$ where the final state particles are coplanar in ϕ, but only one is charged. The mean of the coincidence peak was then determined by a Gaussian fit. Note that the polarimeter did not inhibit this procedure. The small ϕ deflection caused by scattering in the polarimeter is well within the 15° resolution of each PID element.

6.5.2 PID Gain Matching

The method used to set the gains of the PID is similar to the calibration procedure for the TAPS vetos. Plots of ΔE vs. E for each PID element were generated from the simulation and compared with data. Due to the energy lost in passage through the polarimeter, the measured proton energy could not be used for calibration.

Instead, the proton energy in $p\pi^0$ events prior to traversing the polarimeter was reconstructed from the measured π^0 momentum and plotted against ΔE, the energy deposited in the PID element (this analysis is discussed in greater detail in Section 8.2). Projections of the PID energy were taken across an energy range of 135-150 MeV for both histograms, and the peaks fit with Gaussians (Figure 6.8). The PID element gains were then scaled by the ratio of the peak positions, so that the centre of the PID energy distribution of each element matched the simulation.

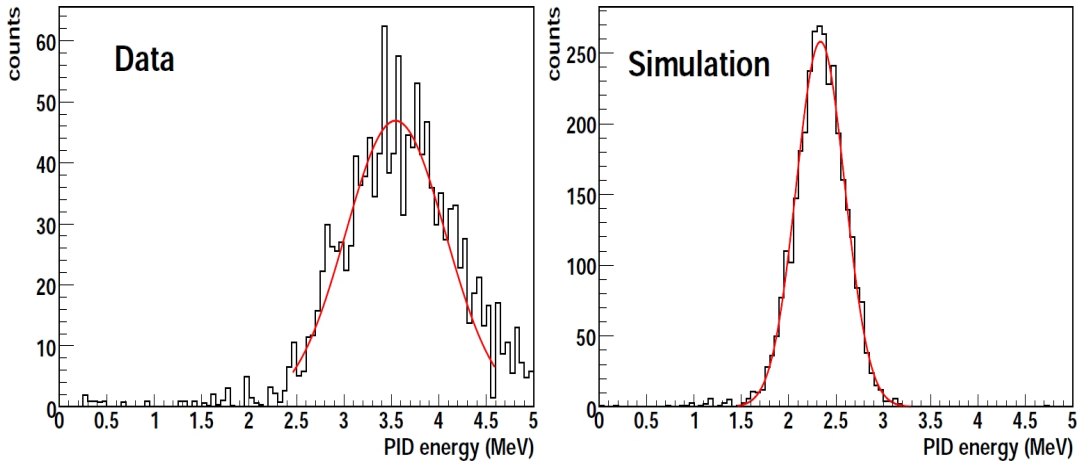

Figure 6.8: Energy deposited in PID element 24 in the data (left) and simulation (right) for protons with reconstructed kinetic energy between 135-150 MeV.

Chapter 7

Polarised Nucleon Scattering

The experiment on which this thesis is based measured the transfer of polarisation from a circularly polarised photon to the recoiling proton in meson photoproduction reactions. The polarisation of this recoiling proton was measured by exploiting a secondary nuclear scatter in the graphite polarimeter. Protons which undergo a nuclear scatter in the polarimeter exhibit a sinusoidally modulated azimuthal distribution, with an amplitude proportional to the transverse polarisation of the incident proton and the proton-carbon analysing power. The analysing power is an intrinsic property of the nuclear reaction occuring in the polarimeter material. The effective analysing power takes into account angular resolutions in the polarimeter and any background contamination in the scattered event sample. This was determined via simulation in order to extract recoil polarisation observables. This chapter outlines how the polarised proton-carbon scattering process was modeled in the simulation of the experimental apparatus. The results will be shown in Chapter 9.

7.1 The Nucleon-Nucleon Interaction

The force between nucleons is a residual of the color force of QCD. It can be thought of as arising due to van der Waals forces between the quarks of neighboring nucleons. A theoretical formulation of the force between nucleons has not yet been achieved within the framework of the fundamental degrees of freedom of QCD (quarks and gluons). Instead, phenomenological models based on two body forces have been developed whose parameters are obtained from fits to NN

data [83, 84]. These models use potentials with terms restricted only by the conserved symmetries of the strong interaction. Due to the observed dependence of the force between nucleons on their spins $\mathbf{s}_1$ and $\mathbf{s}_2$, potentials must contain a $\mathbf{s}_1 \cdot \mathbf{s}_2$ component. The proton-proton, neutron-neutron, and proton-neutron interactions should all have the same strength, after correcting for the electromagnetic force, reflecting the isospin symmetry of the nucleon-nucleon force. A non-central tensor term must also be included.

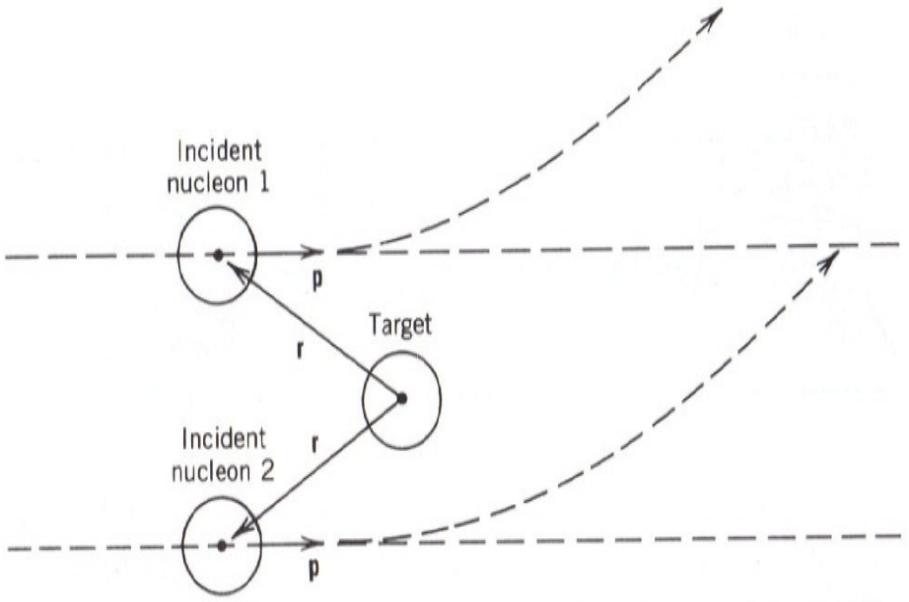

Figure 7.1: The spin-orbit coupling term acts to polarise scattered particles. All spins are oriented out of the page. Image from [85].

The feature of the nuclear force most relevant for polarised scattering is the spin-orbit coupling term. A nucleon with 3-momentum vector $\mathbf{p}$ incident on a nuclear target at a distance $\mathbf{r}$ has an angular momentum $\mathbf{L} = \mathbf{r} \times \mathbf{p}$. The spin-orbit component of the interaction couples the angular momentum vector to the total spin $\mathbf{S} = \mathbf{s}_1 + \mathbf{s}_2$, where $\mathbf{s}_1$ and $\mathbf{s}_2$ refer to the spins of the incoming nucleon and the target. The lowest order formula which preserves parity and time invariance [85] is given by $V_{so}(r)(\mathbf{L} \cdot \mathbf{S})$ where $V_{so}(r) < 0$ is a position dependent scalar. The effect of this term is illustrated in Figure 7.1, where all spins point out of the page. The angular momentum vector of nucleon 1 points into the page, and the dot product $\mathbf{L} \cdot \mathbf{S}$ is negative, so the interaction $V_{so}(r)(\mathbf{L} \cdot \mathbf{S})$ produces a repulsive

force. For nucleon 2, **L** points out of the page, resulting in an attractive force. This simplified picture demonstrates how the spin-orbit term acts to produce scattered particles at a given angle with a particular spin polarisation.

The polarisation P of an ensemble is defined as the asymmetry of the number of spin-up and spin-down particles

$$P = \frac{N(\uparrow) - N(\downarrow)}{N(\uparrow) + N(\downarrow)} \tag{7.1}$$

The inverse reaction, where a beam of polarised protons is incident on an unpolarised target, provides a convenient method for determining the polarisation of the proton beam. The spin-orbit potential results in protons with the same spin being preferentially scattered in the same direction. The polarisation of the incident protons can then be inferred from the azimuthal scattering distribution.

7.2 Polarised Proton Scattering

The derivation of the equation describing the scattering of polarised protons from a nucleus [86, 87] (Figure 7.2) uses the density matrix ρ

$$\rho = \sum_n c_n \chi_n \chi_n^\dagger \tag{7.2}$$

where all of the possible proton spin states χ_n appearing with probability c_n are summed. The average value of an operator S is then given as

$$\langle S \rangle = Tr(\rho S) \tag{7.3}$$

The operator which relates the initial state ρ_i with momentum $\mathbf{p}_{in}$ to the scattered state ρ_{sc} with momentum $\mathbf{p}_{sc}$ is the 2×2 scattering matrix $M(\theta_{sc}, \phi_{sc})$

$$\rho_{sc} = \sum_n c_n M \chi_n \chi_n^\dagger M^\dagger \tag{7.4}$$

The differential cross-section is obtained from ρ_i and ρ_{sc}

$$\frac{d\sigma}{d\Omega} = I = \frac{Tr(\rho_{sc})}{Tr(\rho_i)} \tag{7.5}$$

The incoming and scattered momentum vectors in Figure 7.2 define a scattering plane with unit normal vector $\hat{\mathbf{n}} = \mathbf{p}_{in} \times \mathbf{p}_{sc} / |\mathbf{p}_{in} \times \mathbf{p}_{sc}|$. For a proton with polarisation vector $\mathbf{P} = P_x \cdot \hat{\mathbf{x}} + P_y \cdot \hat{\mathbf{y}}$ the scattering matrix takes the form

$$M(\theta_{sc}, \phi_{sc}) = g(\theta_{sc}) + h(\theta_{sc}) \mathbf{P} \cdot \hat{\mathbf{n}} \tag{7.6}$$

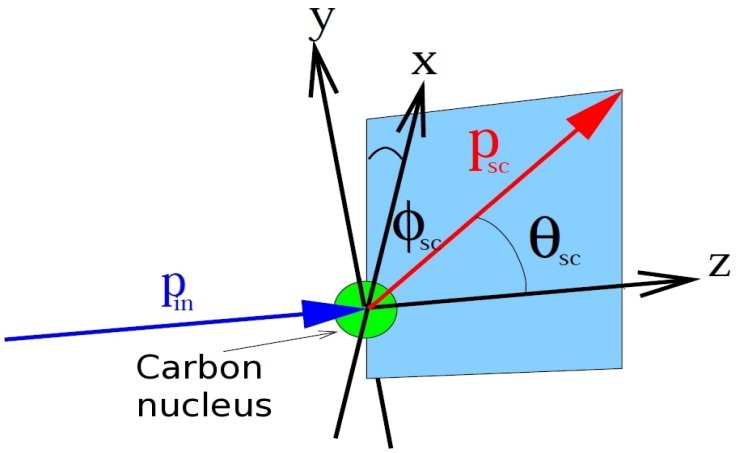

Figure 7.2: Scattering of a proton in a carbon polarimeter.

where $g(\theta_{sc})$ and $h(\theta_{sc})$ are complex functions, and $\mathbf{P}\cdot\hat{\mathbf{n}}$ is the transverse polarisation of the outgoing proton in the scattering plane. It can be shown in the case of a beam completely polarised in the direction $\hat{\mathbf{n}}$ that

$$I = \frac{1}{4}Tr(M^{\dagger}M) + \frac{1}{4}Tr(M^{\dagger}M)\mathbf{P}\cdot\hat{\mathbf{n}} \tag{7.7}$$

Substituting M from Equation 7.6 gives

$$I = \frac{1}{4}Tr(M^{\dagger}M) + \frac{1}{4}Tr(M^{\dagger}M)\mathbf{P}\cdot\hat{\mathbf{n}} = |g|^2 + |h|^2 + 2Re(gh)\mathbf{P}\cdot\hat{\mathbf{n}} = I_0 + I_p \tag{7.8}$$

where $I_0 = |g|^2 + |h|^2$ is the unpolarised differential cross-section, and $I_p = I_0 A\mathbf{P}\cdot\hat{\mathbf{n}}$ is the deviation introduced by the initial proton polarisation. The quantity

$$A = \frac{2Re(gh)}{|g|^2 + |h|^2} \tag{7.9}$$

is the *analysing power* of the reaction. The cross-section equation is now

$$I(\theta_{sc},\phi_{sc}) = I_0 + I_p = I_0(\theta_{sc})\left[1 + A\mathbf{P}\cdot\hat{\mathbf{n}}\right] \tag{7.10}$$

The scattering angles θ_{sc} and ϕ_{sc} are given [88] by

$$\sin\theta_{sc} = |\mathbf{p}_{in}\times\mathbf{p}_{sc}|\,, \qquad \sin\phi_{sc} = -\hat{\mathbf{x}}\cdot\hat{\mathbf{n}}, \qquad \cos\phi_{sc} = \hat{\mathbf{y}}\cdot\hat{\mathbf{n}} \tag{7.11}$$

so that Equation 7.10 can be written as

$$I(\theta_{sc},\phi_{sc}) = I_0(\theta_{sc})\left[1 + A(\theta_{sc})(P_y\cos\phi_{sc} - P_x\sin\phi_{sc})\right] \tag{7.12}$$

The $\mathbf{L}\cdot\mathbf{S}$ term in the nucleon-nucleon interaction produces an azimuthal modulation in the distribution of scattered protons proportional to the product of the initial polarisation and the analysing power.

7.3 Determining Analysing Power

The analysing power of a polarimeter varies as a function of nucleon energy and θ_{sc} and is determined empirically by analsyis of experimental data for polarised nucleon-nucleon scattering. One of the most widely used analysing materials for protons is carbon-12 due to its large scattering cross-section and its widespread availability [89]. The proton-^{12}C analysing power has been measured at TRIUMF [89], PSI [88], Jefferson Lab [90], and LAMPF [91]. These facilities have calibrated carbon polarimeters by measuring the azimuthal distributions in proton-nuclear scattering using incident protons with known polarisation P. In such measurements, the analysing power is the only unknown quantity in Equation 7.12. Polarised beams can be produced by elastically scattering polarised electrons from a hydrogen target or from Van de Graaf accelerators where the polarisation is determined from the ion source [92].

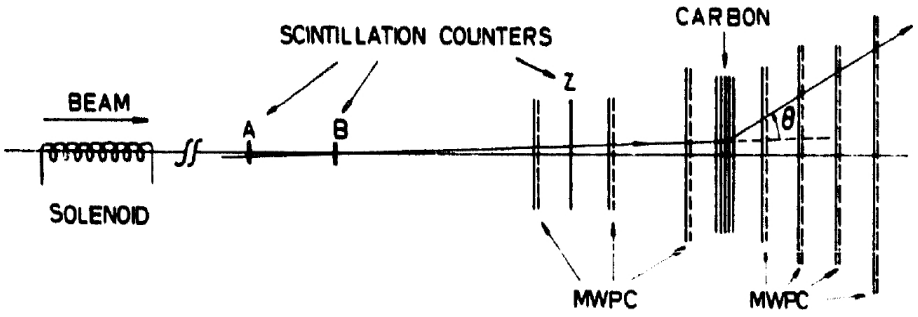

Figure 7.3: Experimental setup used to measure the analysing power of carbon in [88].

Figure 7.3 shows a typical setup used to measure analysing power. Wire chambers record the tracks of a proton into and out of the polarimeter, allowing for a precise measurement of the scattering angles θ_{sc} and ϕ_{sc}. Instrumental asymmetries are minmised by taking data with the beam polarisation vectors $\mathbf{P}$ and $-\mathbf{P}$. Selected events have a single detected track before and after scattering in the polarimeter and a polar scattering angle θ_{sc} between 5° and 20°. The analysing power at a fixed beam energy can then extracted as a function of θ_{sc} from the asymmetry of the ϕ_{sc} distribution (Figure 7.4).

The extensive data set available for p-^{12}C scattering allows a parameterised fit of the analysing power as a function of incident proton momentum p and

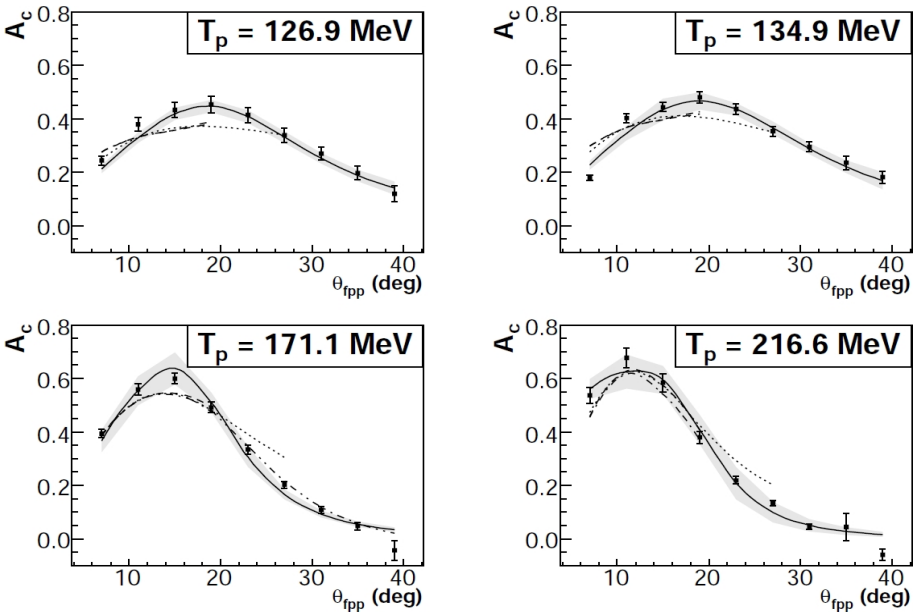

Figure 7.4: Analyzing power as a function of θ_{sc} at different beam energies measured by [90], compared to parameterisations obtained in previous experiments. The gray area indicates the error band.

scatter angle θ_{sc} to be obtained. The most widely used parameterisation is from McNaughton [62]

$$A(\theta_{sc}, p) \quad = \quad \frac{ar}{1 + br^2 + cr^4} \tag{7.13}$$

where $r = p\sin\theta_{sc}$ and the coefficients a,b,c are defined as

$$X = \sum_{i=0}^{i=4} X_i (p - p_0)^i, X = a, b, c$$

with an offset p_0. For data above 450 MeV, an extra term $dp\sin(5\theta_{sc})$ is included, where d is defined in the same way as a, b, c. This additional term is necessary due to the non-negligible contribution from inelastic scattering at increasing proton energies [91].

7.4 Simulation of Polarised Scattering

In order to extract proton polarisation from experiment, the analysing power must be known at each data point. The polarimeter installation at MAMI lacked a pro-

ton beam of known polarisation, ruling out a direct measurement. Consequently, the polarimeter was calibrated using a Geant4 simulation of the experimental setup. While Geant4 accurately calculates the energy loss and θ_{sc} distribution of protons traversing the carbon polarimeter, the models do not include the effects of polarised scattering. This required new algorithms to introduce the proper azimuthal distribution, allowing the analysing power of the polarimeter to be obtained from simulation.

7.4.1 New Analysing Power Parameterisation

Previous measurements and parameterisations of the proton-carbon analysing power were performed over the proton energy and scatter angle acceptance appropriate for the particular experimental setup. The phase space covered by the Crystal Ball polarimeter for the reaction $\gamma p \rightarrow p\pi^0$, shown in Figure 7.5, was not fully described by any existing analysing power parameterisation.

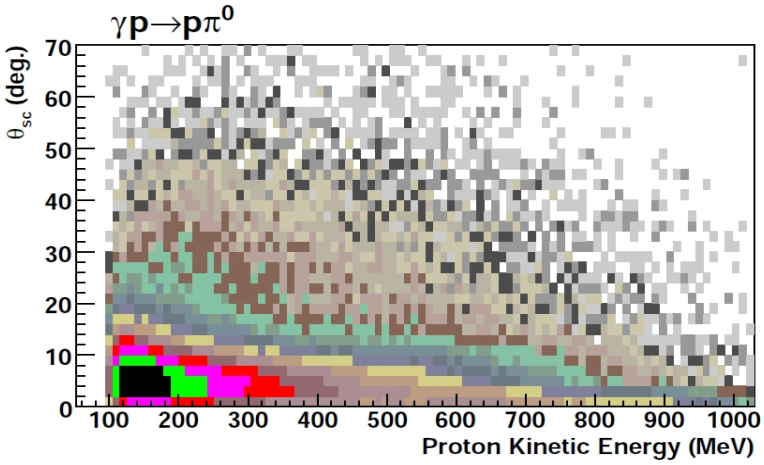

Figure 7.5: Simulation of the phase space for the reaction $\gamma p \rightarrow p\pi^0$ for photon beam energies between 0.4-1.4 GeV. The scattering angle θ_{sc} is calculated from reaction kinematics.

As a result, a new parameterisation of the analysing power was done based on the world data set of proton-carbon elastic scattering (Figure 7.6). The functional form used, based on that used in [90], was

$$A(\theta_{sc}, p) = \frac{ar}{1 + br^2 + cr^4 + dr^6} + ep\sin(5\theta_{sc}), \tag{7.14}$$

$$\begin{aligned} r &= p\sin\theta_{sc}, \\ X &= \sum_{i=0}^{i=4} X_i(p-p_0)^i, X = a, b, c, d \end{aligned}$$

where the extra term in the denominator was added to improve the fit. A χ^2 minimisation fit to the data shown in Figure 7.6 was optimised by the parameters in Table 7.1, with p_0 = 1.67672 GeV/c and e=0.108356 $(\mathrm{GeV/c})^{-1}$. This parameterisation is valid from 80-800 MeV and $2^\circ < \theta_{sc} < 40^\circ$, and the fit, which does not take into account systematic uncertainties, has a χ^2 of 2.19 per data point (Figure 7.7).

	0	1	2	3	4
a	2.20904	1.43983	-9.72434	-35.2466	-21.2429
b	4.9952	-7.97064	88.3627	296.751	195.305
c	37.1864	-200.439	1160.7	-3119.27	-3920.79
d	8.9808	-166.891	1181.26	-3212.6	4446.96

Table 7.1: Fit parameters for the analysing power parameterisation.

7.4.2 Inelastic Scattering

An important aspect of the analysing power measurements described above is the insistence on observing a single track before and after scattering. This primarily restricts the event space to elastically scattered protons, where the carbon nucleus is left intact. However, as the energy of the incoming proton increases, the probability of inelastic scattering increases. In such events, the incoming proton scatters off of a single nucleon in the carbon nucleus. The scattered nucleon takes away most of the available kinetic energy, while the residual nucleon typically has an energy less than 100 MeV.

An additional feature of such reactions is the possibility of charge exchange, when the proton scatters off a neutron inside the carbon. It may be that in experiments with trackers, the low energy recoil protons from charge exchange reactions are measured. Such events would effectively contribute negative analysing power. These events are also relevant for the Crystal Ball, which has a neutron detection efficiency of $\approx 30\%$ at 100 MeV. Figure 7.8 shows the fraction of scatters where a

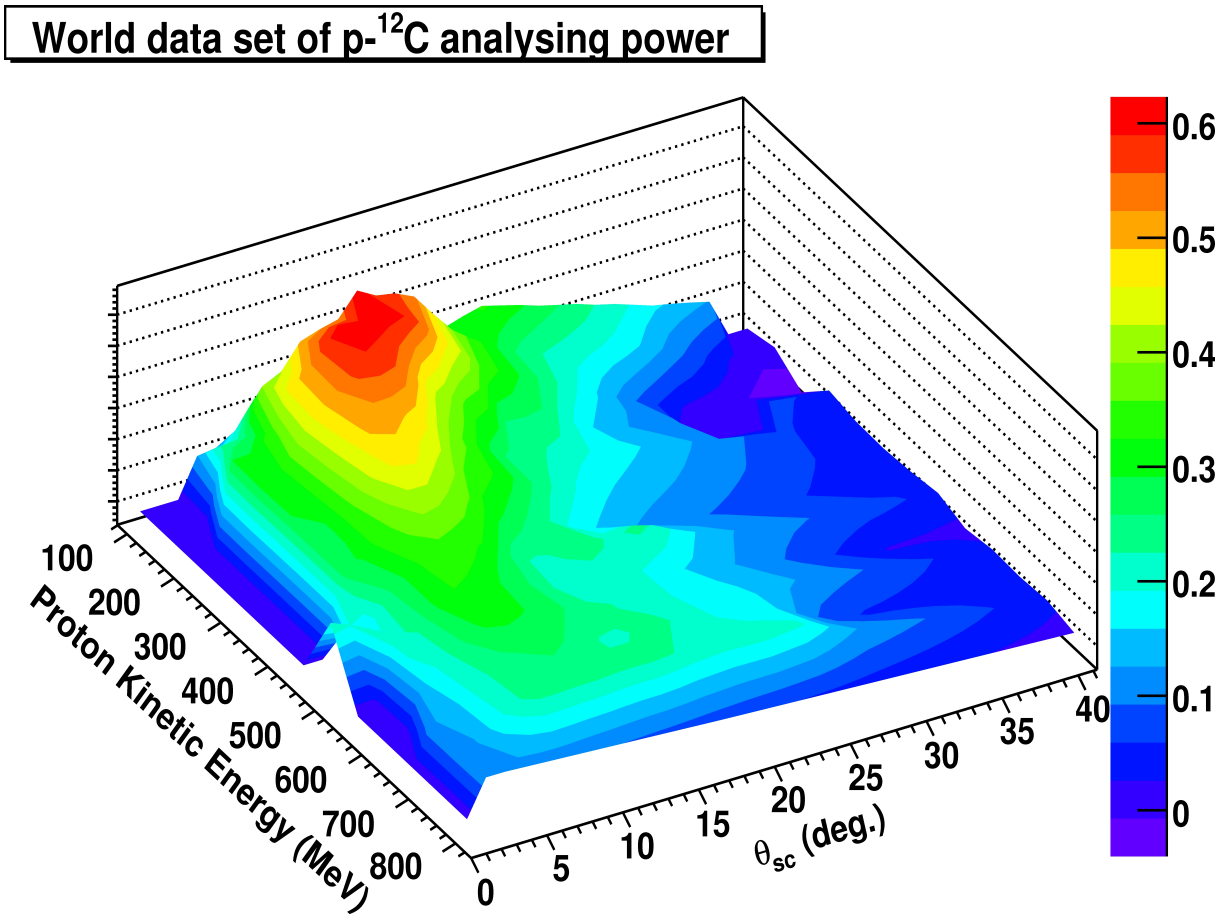

Figure 7.6: World data set for proton-carbon analysing power up to 800 MeV.

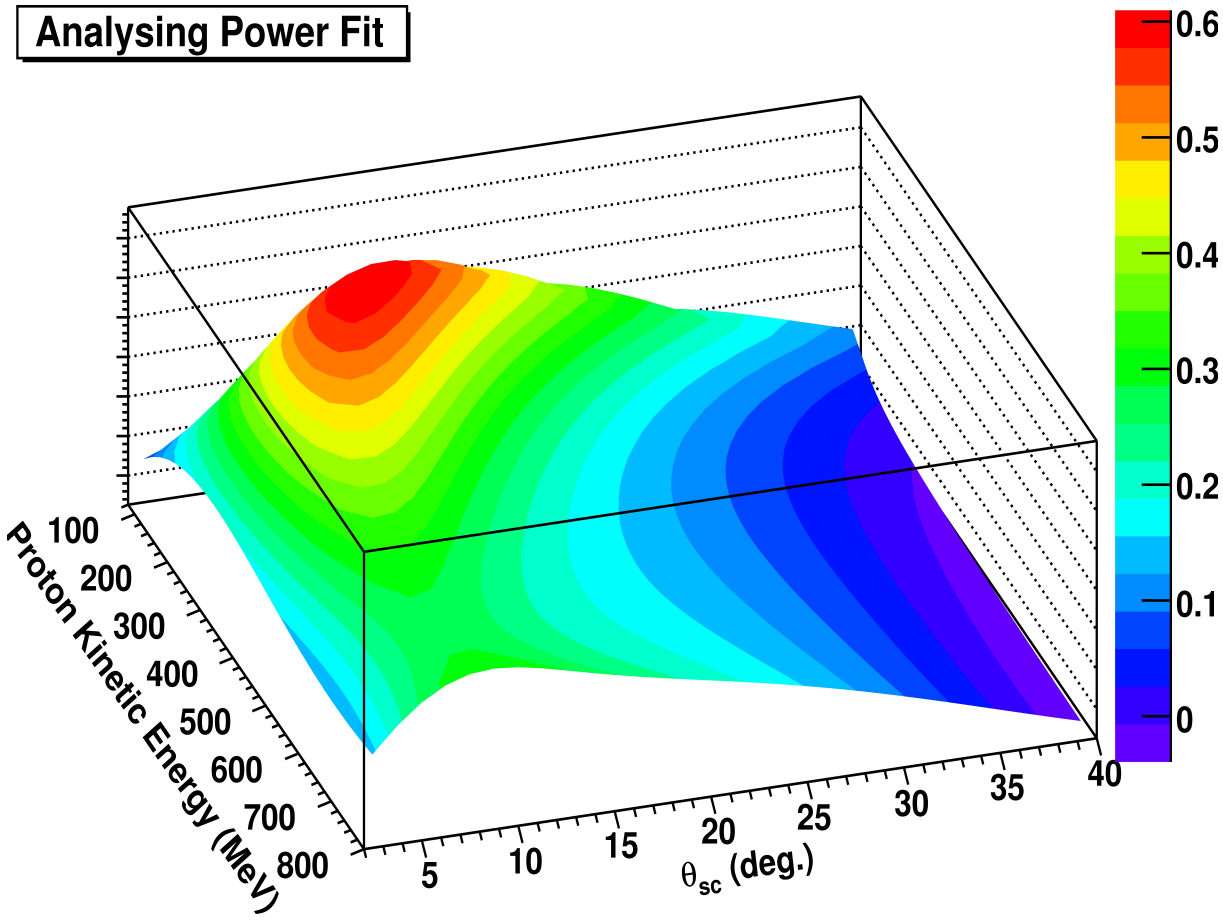

Figure 7.7: Fit of the analysing power data shown in Figure 7.6.

neutron was detected in the simulation. While such events only represent around 5% of all nuclear scatters, they have a significant effect above 500 MeV.

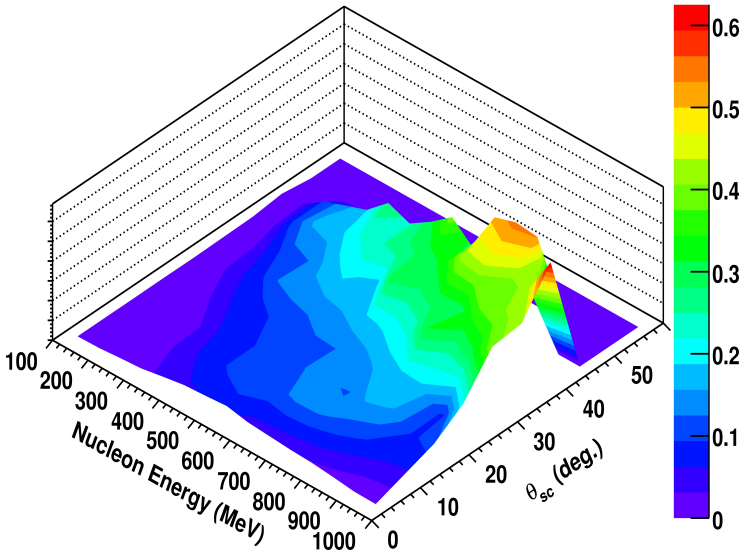

Figure 7.8: The fraction of charge exchange reactions, where a neutron was detected in the simulation.

Crucially, scattering from a single nucleon has a different analysing power distribution than elastic scattering from the entire nucleus. The quasi-free proton-proton and proton-neutron analysing powers are shown in Figure 7.9. Based on the extensive data set of proton-proton and proton-neutron scattering, partial wave analyses like SAID are able to accurately parameterise these analysing powers.

The histograms in Figure 7.9 were read into the simuation, while the analysing power of an elastically scattered event was calculated using Equation 7.14 and the parameters in Table 7.1. When an inelastic scatter in the polarimeter occured, an analysing power was assigned to the event based on the final state nucleon with the highest kinetic energy and the quasi-free analysing power. In both cases, the analysing power was then used to modify the outgoing azimuthal scattering angle to conform to the distribution of Equation 7.12.

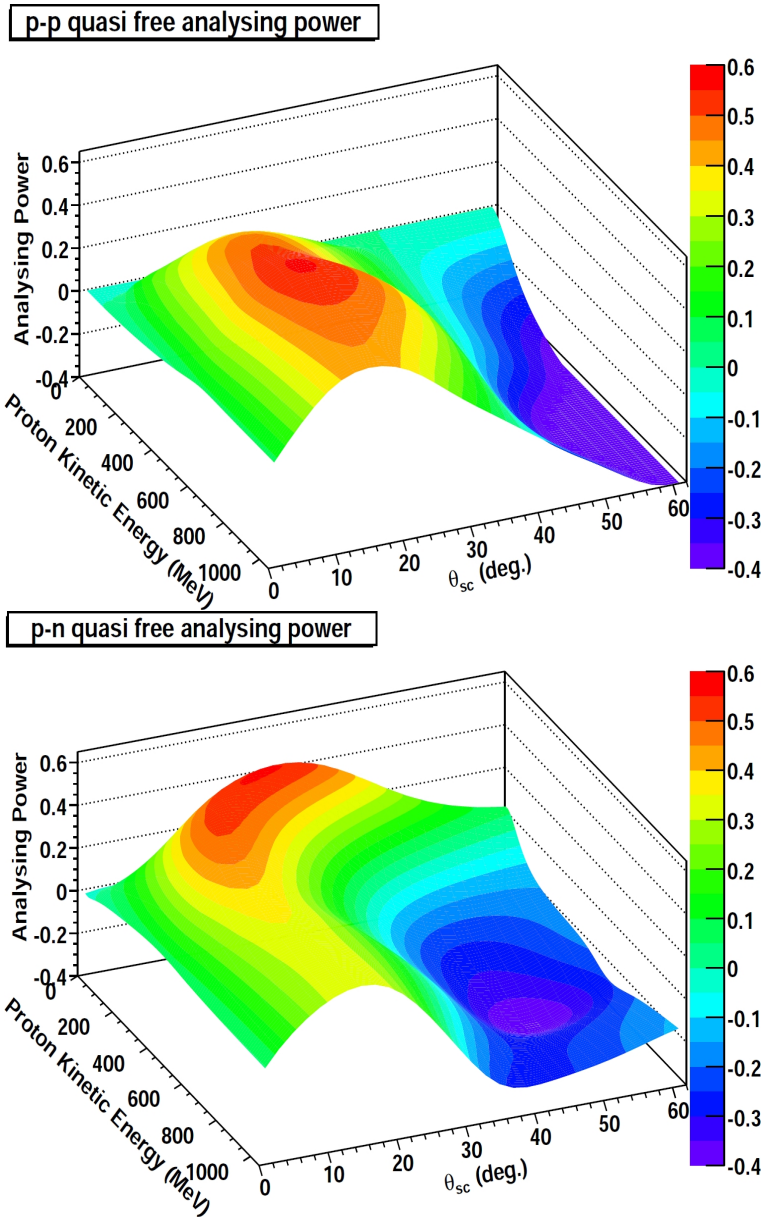

Figure 7.9: SAID calculation of the proton-proton (top) and proton-neutron (bottom) analysing powers [93].

7.4.3 Simulated Azimuthal Scattering Distribution

To obtain the azimuthal distribution of Equation 7.12, the initial proton polarisation was set as $\mathbf{P} = P_x\hat{\mathbf{x}}$, with P_x=±1, so that the transverse polarisation P_T is 100% with no $\hat{\mathbf{y}}$ component. Consequently, the cosϕ_{sc} term in Equation 7.12 vanishes, leaving

$$I(\theta_{sc}, \phi_{sc}) = I_0(\theta_{sc})\,[1 - AP_x\sin\phi_{sc}] \tag{7.15}$$

The analysing power A of an event which had a nuclear scatter was calculated in the simulation on an event by event basis. The ϕ scattering angle ϕ_{old} then needed to be chosen from a new distribution which has been weighted according to the expected ϕ distribution calculated using the analysing power. This was achieved as follows. First, a new azimuthal angle ϕ_{new} was randomly chosen in the range $[0, 180°]$. To check if ϕ_{new} defined an appropriate shift for ϕ_{old}, a new random number $y \in [0, 2]$ was generated. Then

$$\text{if } y > 1 - AP_T\sin\phi_{new}, \qquad \phi_{new} \rightarrow -180° + \phi_{new} \tag{7.16}$$

Otherwise, ϕ_{new} was unchanged.

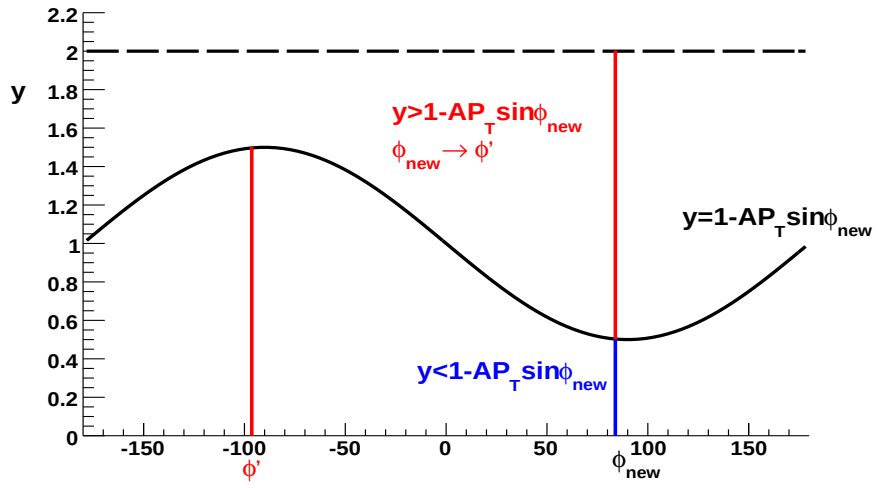

Figure 7.10: The initially flat azimuthal distribution is given the correct 1-A$P_T$sinϕ_{sc} modulation.

This maps the initially flat distribution of ϕ_{new} between 0 and 180° to the desired 1-AP_Tsinϕ_{new} distribution spanning -180° to 180° (Figure 7.10). The

new ϕ angle is then used to define a rotation ϕ_{rot} about the z-component of the scattered particle 4-vector

$$\phi_{rot} = \phi_{new} - \phi_{old} \tag{7.17}$$

The 4-vectors of all final state particles undergo this rotation in order to conserve energy and momentum.

7.5 Summary

The nucleon-nucleus interaction is a residual of the color force between quarks. It is described phenomenologically based on extensive experimental observation of its properties. The spin-orbit coupling term provides a mechanism by which polarimeters can be used to measure nucleon polarisation in scattering reactions. The cross-section of such reactions has an azimuthal modulation proportional to the initial polarisation and the analysing power of the reaction. The analysing power for elastic proton-carbon scattering has been measured at several facilities using proton beams of known polarisation. These measurements have been parameterised as a function of energy and polar scattering angle over the phase space covered by the Crystal Ball. The quasi free proton-proton and proton-neutron analysing powers are used to describe inelastic scattering. The simulation of the experimental setup uses these analysing power assignments to model polarised scattering and to benchmark the polarimeter performace. Chapter 8 discusses how the simulation is used to extract polarisation observables from the data.

Chapter 8

Selection of Nuclear Scattered Events

8.1 Analysis Procedure

In the reactions of interest, a photon with 4-vector $\overrightarrow{\mathbf{p}}_{beam}$ induces an electromagnetic interaction, producing a pseudoscalar meson and a recoiling proton. The meson subsequently decays electromagnetically to two photons on a time scale of $\sim 10^{-16}$ seconds. The recoiling proton scatters in the polarimeter into the detector system, and the scattering angles are calculated at the scattering location.

The momentum of the meson can be reconstructed from the sum of the detected decay photons. The 4-vector of the recoiling proton prior to scattering $\mathbf{p}_{rec}$ can then be calculated from the tagged photon beam

$$\mathbf{p}_{rec} = \mathbf{p}_{target} + \mathbf{p}_{beam} - \mathbf{p}_{meson} \tag{8.1}$$

where the target 4-vector $\mathbf{p}_{target}$ is

$$\mathbf{p}_{target} = (m_p, \overrightarrow{\mathbf{0}}), \qquad m_p = 938.27 \text{ MeV} \tag{8.2}$$

The diagram in Figure 8.1 illustrates the reconstruction of the scattered vector for nucleons scattered into both the Crystal Ball and TAPS. When the scattered nucleon is detected (red), the angles θ_{det} and ϕ_{det} are recorded by the calorimeter with respect to the centre of the target. To obtain the scattering vector at the polarimeter (blue), the position vector from the target to the location of the

detected nucleon $\vec{\mathbf{r}}_{det}$ is calculated (green), and the scattered 3-vector $\vec{\mathbf{r}}_{sc}$ is obtained from the vector subtraction

$$\vec{\mathbf{r}}_{sc} = \vec{\mathbf{r}}_{det} - \vec{\mathbf{r}}_{rec} \tag{8.3}$$

The determination of $\vec{\mathbf{r}}_{rec}$ is described in Section 8.3. The scattering angles θ_{sc} and ϕ_{sc} can then be obtained. They are defined as the angles of $\vec{\mathbf{r}}_{sc}$ in a frame defined by

$$\hat{\mathbf{z}} = \hat{\mathbf{p}}_{rec}, \qquad \hat{\mathbf{y}} = \frac{\hat{\mathbf{p}}_{beam} \times \hat{\mathbf{p}}_{CM}}{|\hat{\mathbf{p}}_{beam} \times \hat{\mathbf{p}}_{CM}|}, \qquad \hat{\mathbf{x}} = \hat{\mathbf{y}} \times \hat{\mathbf{z}} \tag{8.4}$$

where $\mathbf{p}_{CM}$ is the meson vector boosted into the centre of mass frame.

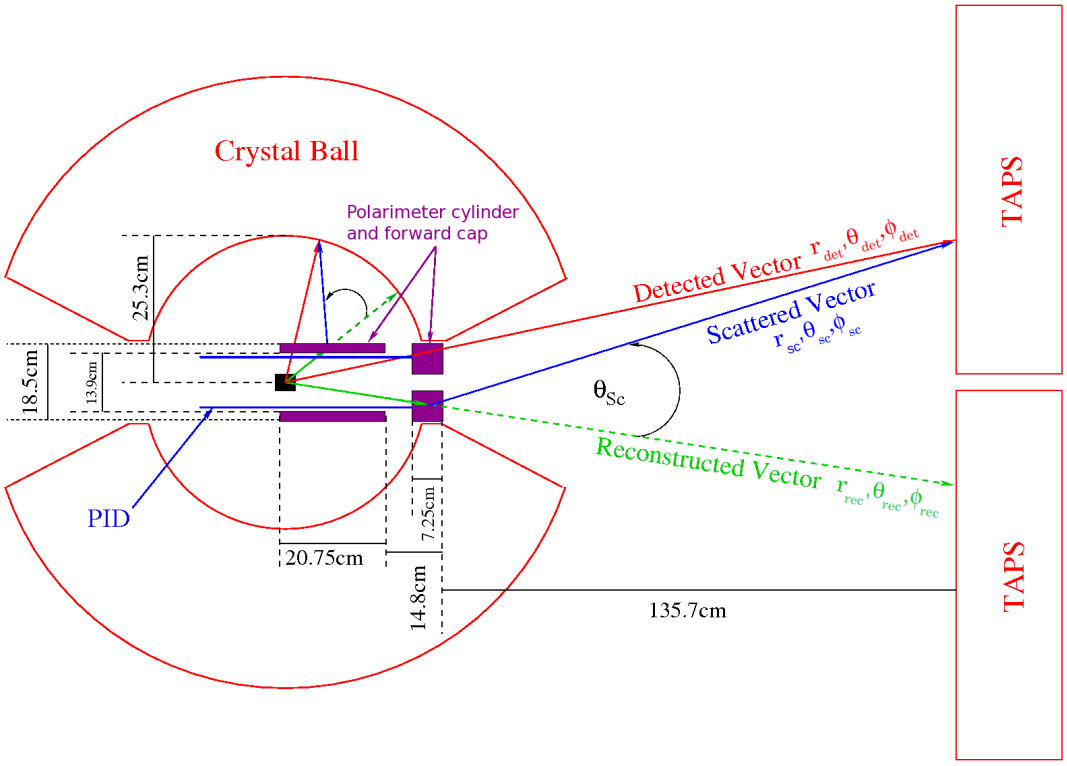

Figure 8.1: Schematic of the polarimeter setup [94].

8.2 Reaction Identification

Analysis of polarimeter data begins with consideration of the number of particles detected. Figure 8.2 shows the number of clusters in the Crystal Ball and

TAPS at the start of the analysis process. The final state in the reactions under consideration have one nucleon and two photons, so 3 cluster events are selected for analysis. The identity of each particle as the nucleon or a decay photon must be determined by reconstructing the π^0 4-vector.

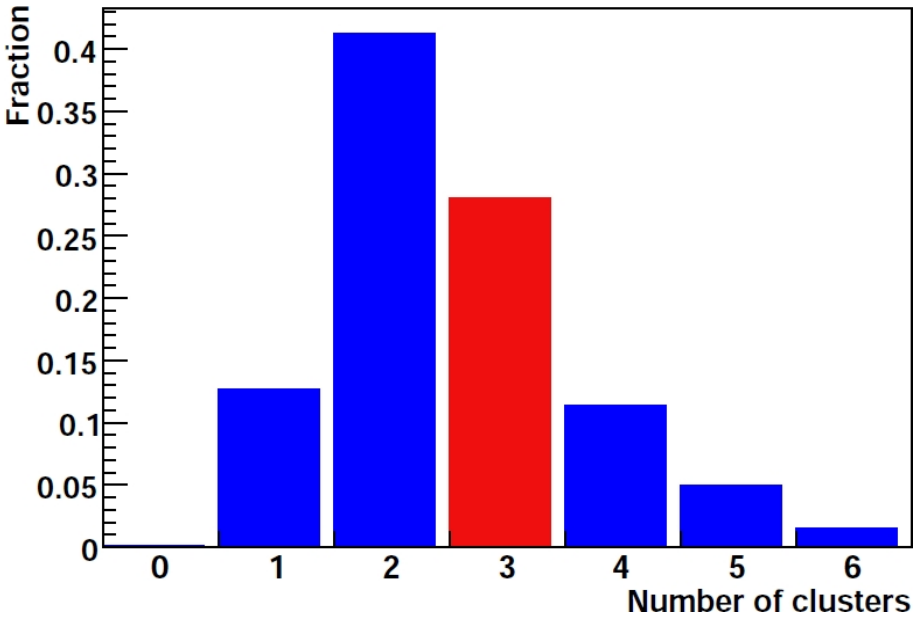

Figure 8.2: The number of clusters reconstructed in the Crystal Ball and TAPS. Analysed events have 3 detected particles.

Initially, each particle is assumed to be a (massless) photon. A Lorentz vector $\mathbf{v}_i$ can then be associated with each cluster

$$\mathbf{v}_i = (E, \overrightarrow{\mathbf{p}}\ ), \qquad |\overrightarrow{\mathbf{p}}\ | = p = E_{measured}$$

and the components of $\overrightarrow{\mathbf{p}}$ can be obtained from the lab angles

$$p_x = p\sin\theta_{lab}\cos\phi_{lab}, \qquad p_y = p\sin\theta_{lab}\sin\phi_{lab}, \qquad p_z = p\cos\theta_{lab} \tag{8.5}$$

The clusters corresponding to π^0 decay photons can be inferred by considering the 3 two particle combinations and identifying π^0 candidates. The sum of the Lorentz vectors $\mathbf{v}_i + \mathbf{v}_j$ is computed

$$v_i + v_j = \left(E_i + E_j, \overrightarrow{\mathbf{p}_i} + \overrightarrow{\mathbf{p}_j}\right) \tag{8.6}$$

and the invariant mass $M_{2\gamma}$ is calculated

$$M_{2\gamma}^2 = (E_i + E_j)^2 - |\overrightarrow{\mathbf{p}_i} + \overrightarrow{\mathbf{p}_j}|^2 \tag{8.7}$$

The combination $\mathbf{v}_i$,$\mathbf{v}_j$ that best reconstructs the mass of the pion M_{π^0}=135 MeV is used to define the photons, with the other cluster taken as the proton. The observed $M_{2\gamma}$ distribution is shown in Figure 8.3. A cut is made so that 100 MeV $< M_{2\gamma} <$ 170 MeV. A subsequent check of the $\pi^0 \rightarrow 2\gamma$ candidates is done to verify that the decay products are indeed uncharged photons. The ϕ angles of the photon 4-vectors are compared to the PID hits for the event to verify that there is no coincidence, and the TAPS vetoes are checked to ensure that the element in front of a proposed photon cluster did not fire.

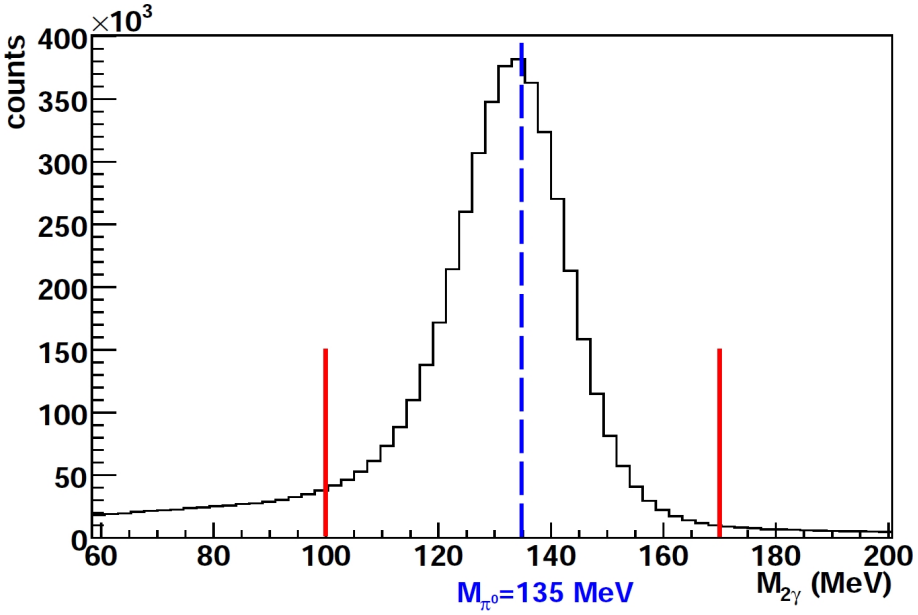

Figure 8.3: Invariant mass of 2 particle cluster sums.

The 4-vector of the π^0 $\mathbf{p}_{\pi^0}$ is then

$$\mathbf{p}_{\pi^0} = \mathbf{v}_i + \mathbf{v}_j \tag{8.8}$$

and the 4-vector of the recoil proton can be obtained from Equation 8.1

$$\mathbf{p}_{miss} = \mathbf{p}_{rec} = \mathbf{p}_{in} - \mathbf{p}_{\pi^0} \tag{8.9}$$

where the sum of the momenta of the beam and target have been written as $\mathbf{p}_{in}$, the total incident momentum. The vectors $\mathbf{p}_{rec}$ and $\mathbf{p}_{\pi^0}$ are coplanar in ϕ by construction. The calculation assumes the 'missing' momentum $\mathbf{p}_{miss}$ after reconstructing the π^0 is due to the recoiling proton, as is expected for a p(γ,π^0)p reaction. The mass M_{miss} of this 4-vector, displayed in Figure 8.4, has a well-defined peak centred on the proton mass of 938 MeV. A cut is applied so that M_{miss} is within the range 850-1050 MeV.

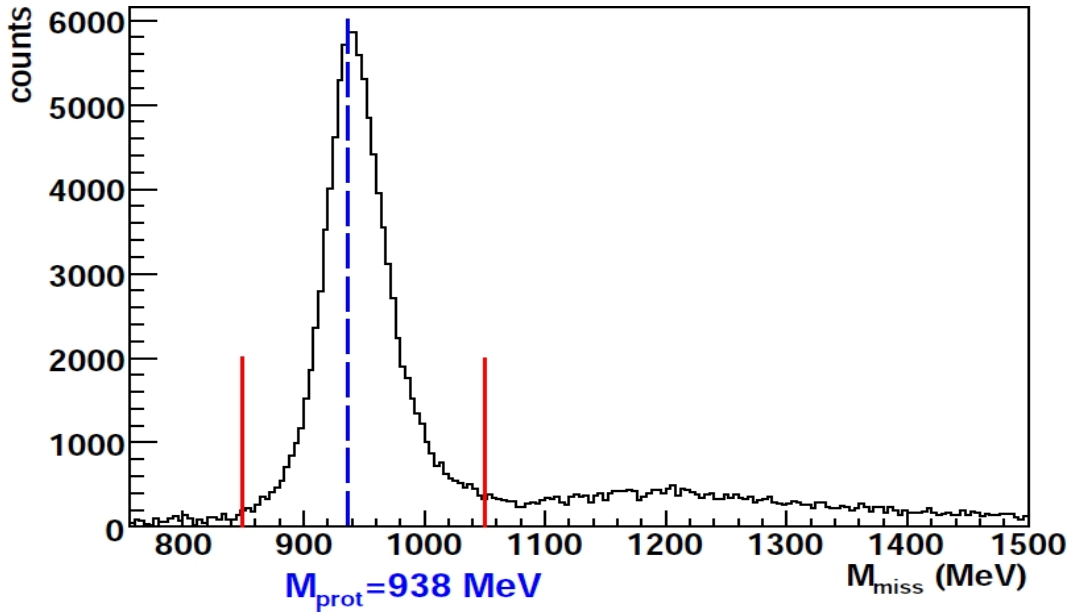

Figure 8.4: Missing mass spectrum.

Identification of charged particles with the Crystal Ball and TAPS is usually achieved using the $\Delta E - E$ method, where the energy E in the calorimeter is compared to the small amount of energy ΔE deposited in the PID or TAPS vetoes respectively. The dependence of ΔE on the kinetic energy E produces a clear separation of charged particles by mass. However, the subsequent energy loss of protons in the analysing material surrounding the PID degrades this distinction (Figure 8.5). Instead of using this degraded correlation, a new particle identification technique was developed. The first step in this method is requiring a correlation between the reconstructed ϕ angle of the recoil proton ϕ_{rec} and an appropriate PID element. A correlated PID hit was identified by the condition $|\phi_{rec} - \phi_{PID}| < 15°$. Once a correlated PID hit has been established, the energy

ΔE measured by the PID element is compared to the kinetic energy of the recoil proton (Figure 8.6). By using this reconstructed energy rather than the detected energy, a clear proton ridge can be seen (Figure 8.6). Points lying inside the defined boundaries are identified as $p\pi^0$ events.

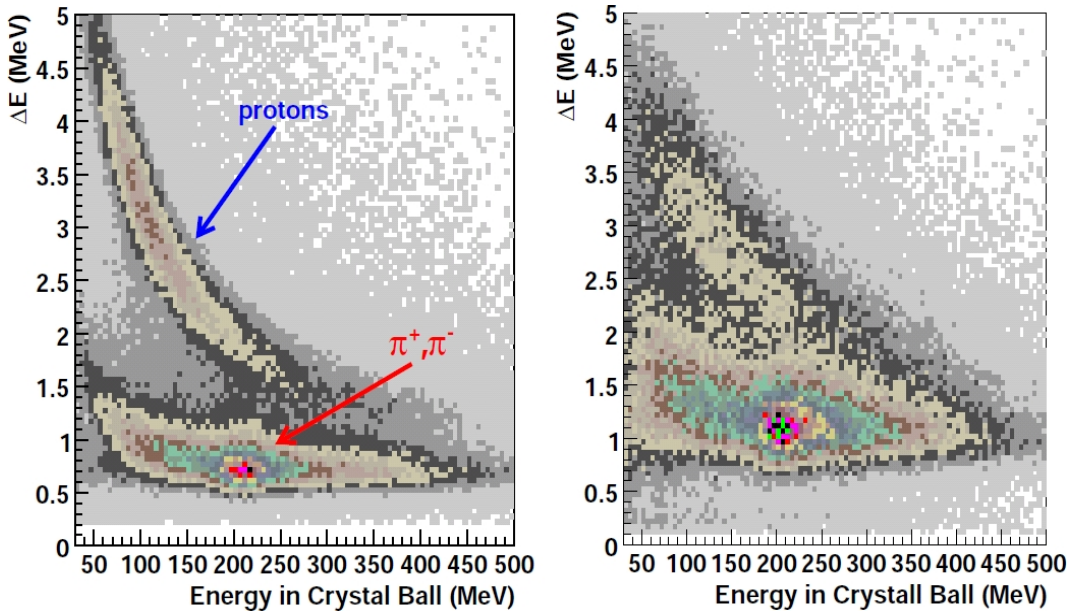

Figure 8.5: The histogram on the left illustrates particle identification with the Crystal Ball and PID in the usual experimental configuration, separating protons and charged pions in clearly defined loci. With the polarimeter installed (right), charged particles lose energy as they traverse the analysing material, and the separation is blurred.

One advantage conferred by this new particle identification method is the clean identification kinematically of protons which are energetic enough to punch through the NaI crystals. At kinetic energies greater than ~450 MeV, protons punch through the Crystal Ball and therefore do not deposit their full energy in the NaI crystals. The new method recovers these punch through events and includes protons with energies greater than 1 GeV. This significantly expands the available event sample.

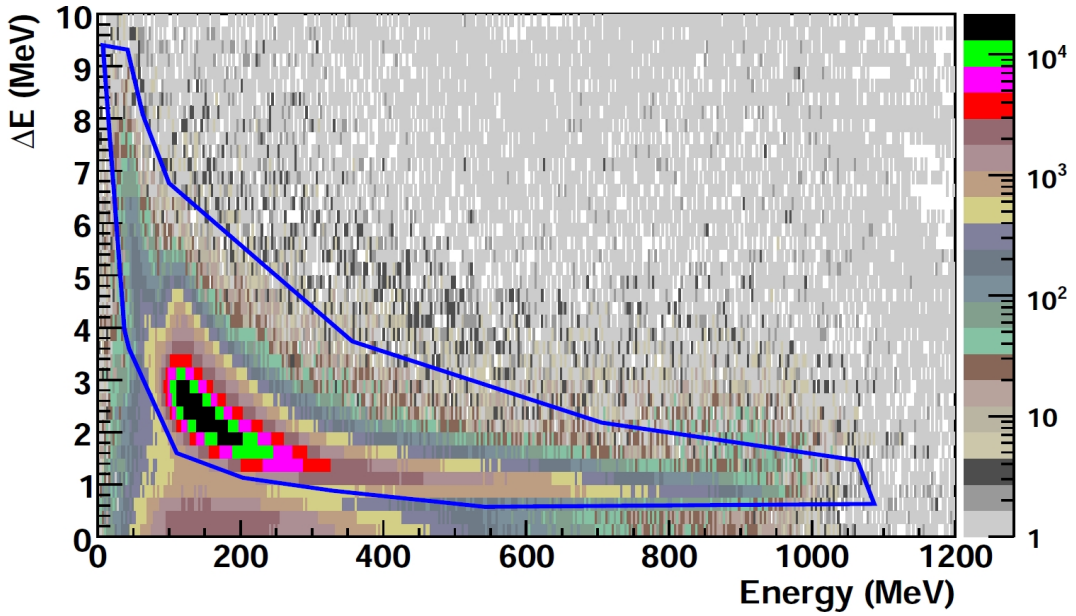

Figure 8.6: Identification of $p\pi^0$ events using a coincidence between a PID element and the reconstructed recoil proton 4-vector. Viewed on a log-z scale.

8.3 Reconstructing Scattering Angles

After identifying $p\pi^0$ reactions, the scattering of protons in the carbon polarimeter was reconstructed. Events for which the reconstructed proton kinetic energy was less than 100 MeV are excluded, as these events are not energetic enough to pass through the analysing material. The reconstructed lab theta angle θ_{rec} of the reconstructed proton is used to determine if the scatter occured in the forward cap or the cylinder. If θ_{rec} <12°, the proton is taken to have been incident on the forward cap, while all other events are taken to have been scattered by the graphite cylinder. In each case, the scattering is assumed to take place at the midpoint of the polarimeter thickness. The position vector from the centre of the target to the scattering location $\overrightarrow{\mathbf{r}}_{rec}$ can then be drawn as

$$\begin{aligned} \overrightarrow{\mathbf{r}}_{rec} &= 36/\cos\theta_{rec}\hat{\mathbf{p}}_{rec} \qquad \text{for } \theta_{rec} < 12^\circ \\ \overrightarrow{\mathbf{r}}_{rec} &= 8.25/\sin\theta_{rec}\hat{\mathbf{p}}_{rec} \qquad \text{for } \theta_{rec} \geq 12^\circ \end{aligned}$$

where $\hat{\mathbf{p}}_{rec}$ is a unit vector in the direction of the recoil proton momentum. The detected nucleon angles θ_{det} and ϕ_{det} define a unit vector $\hat{\mathbf{r}}_{det}$ which is then scaled

according to whether the nucleon is detected in the Crystal Ball or TAPS.

$$\vec{\mathbf{r}}_{det} = R\ \hat{\mathbf{p}}_{rec}, \quad R = \begin{cases} 49 \text{ cm}, & \text{nucleon detected in Crystal Ball} \\ 173 \text{ cm}, & \text{nucleon detected in TAPS} \end{cases}$$

This describes a vector from the centre of the target to the hit position in the detector, which is taken to occur at halfway along the depth of a calorimeter element. The scattered vector $\vec{\mathbf{r}}_{sc}$ is then calculated from Equation 8.3

$$\vec{\mathbf{r}}_{sc} = \vec{\mathbf{r}}_{det} - \vec{\mathbf{r}}_{rec}$$

and the scattering angles θ_{sc} and ϕ_{sc} are constructed from the axes defined previously in Equation 8.4. The distributions are shown in Figure 8.7.

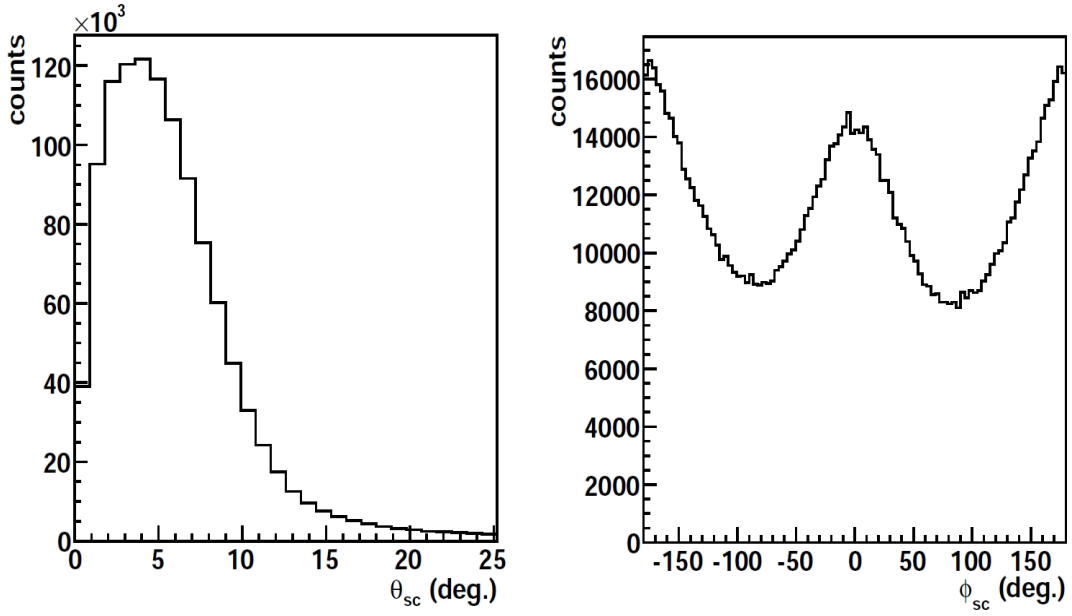

Figure 8.7: Polar (left) and azimuthal (right) scattering angles reconstructed in the analysis.

Only ∼12% of protons incident on the polarimeter will undergo a nuclear scatter. The histograms shown in Figure 8.7 therefore include a large background of $p\pi^0$ events which did not have a nuclear scatter in the polarimeter. This background must be identified and reduced in the event sample as such events contain no polarisation information for the proton. The contribution from the background can be seen in Figure 8.8, where θ_{sc} is plotted on a logarithmic scale

for the data (magenta), the Geant4 simulation (blue), and the simulation with the nuclear interaction switched off (red). The simulation agrees very well with the data, lending support to the accuracy of the modelling of scattering in Geant4.

From Figure 8.8, it is evident that up to θ_{sc} ~13°, the background of non-nuclear scattered events dominates. Nuclear scattered events lie in the shaded region, and these scatters must be separated from the ≈90% background.

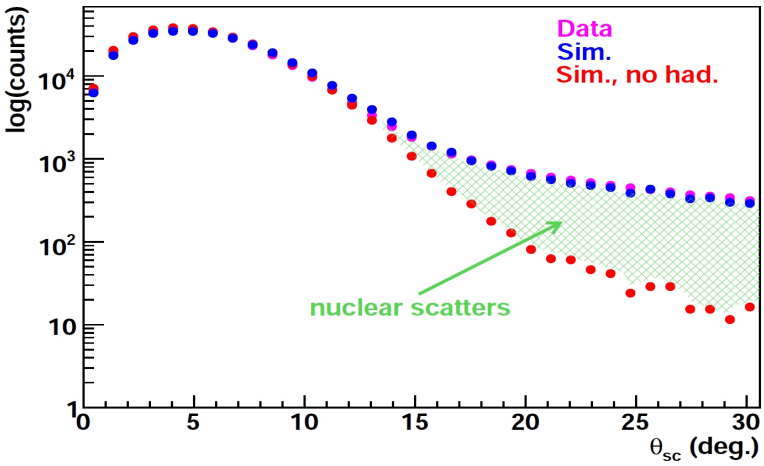

Figure 8.8: Comparison of θ_{sc} for data (magenta), simulation (blue), and the simulation with no hadronic interaction (red). Nuclear scattered events lie in the shaded region.

8.4 Cut Optimisation

Figure 8.8 suggests that most of the background can be removed by cutting on θ_{sc} >13°. However, the p-^{12}C analysing power tends to peak at θ_{sc} ≈10°, so a cut at 13° would remove events that produce large asymmetries. Furthermore, it is clear from Figure 8.9 that a correlation between θ_{sc} and ϕ_{sc} exists, so a cut on θ_{sc} should optimally include a dependence on ϕ_{sc}.

The observables used to select nuclear scattered events are θ_{diff}=θ_{det}-θ_{recon} and ϕ_{diff}=ϕ_{det}-ϕ_{recon}, the differences between the reconstructed and detected angles. These quantities measure the degree by which the recoil proton was deflected from its initial kinematically reconstructed trajectory after passing through the polarimeter. A 2-dimensional plot of ϕ_{diff} vs. θ_{diff} is displayed in Figure 8.10.

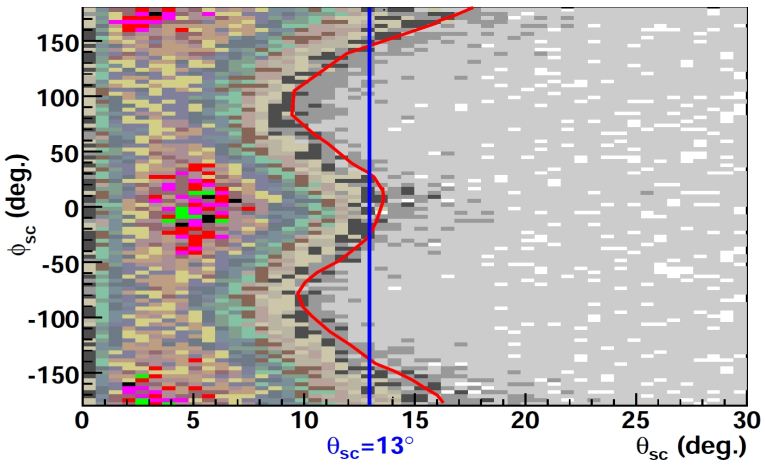

Figure 8.9: Plotting the polar and azimuthal scattering angles simultaneously reveals the ϕ dependence of the θ_{sc} distribution. An effective selection cut for nuclear scattered events would follow the contour shown in red.

The high concentration of events in an elliptical region around (0,0) dominantly arises from small angle deflections from Coulomb scattering. Events with large deflections are more likely to have had a nuclear scatter. An elliptical exclusion region is then defined in terms of θ_{diff} and ϕ_{diff} to reject these background events from the sample.

The shape of the cut is determined using the output of the simulation. Beam helicity asymmetries are simulated by defining a polarisation vector $\overrightarrow{\mathbf{P}}$ at runtime:

$$\overrightarrow{\mathbf{P}} = hP_x\hat{\mathbf{x}} \tag{8.10}$$

where h=±1 is the helicity of the beam. The azimuthal modulation of the scattering with analysing power (Section 7.4) is included for events which scattered in the polarimeter, while all other events are given an analysing power of 0. The angular distribution of protons which had a nuclear scatter in the polarimeter is then given by Equation 7.15

$$N^{\pm}(\theta_{sc},\phi_{sc}) = N_0(\theta_{sc})\left[1 \mp AP_x\sin\phi_{sc}\right]$$

where $N^{\pm}$ is the distribution for beam helicity state ±. Forming an asymmetry between the two helicity states gives:

$$\frac{N^- - N^+}{N^- + N^+} = A\sin\phi_{sc} \tag{8.11}$$

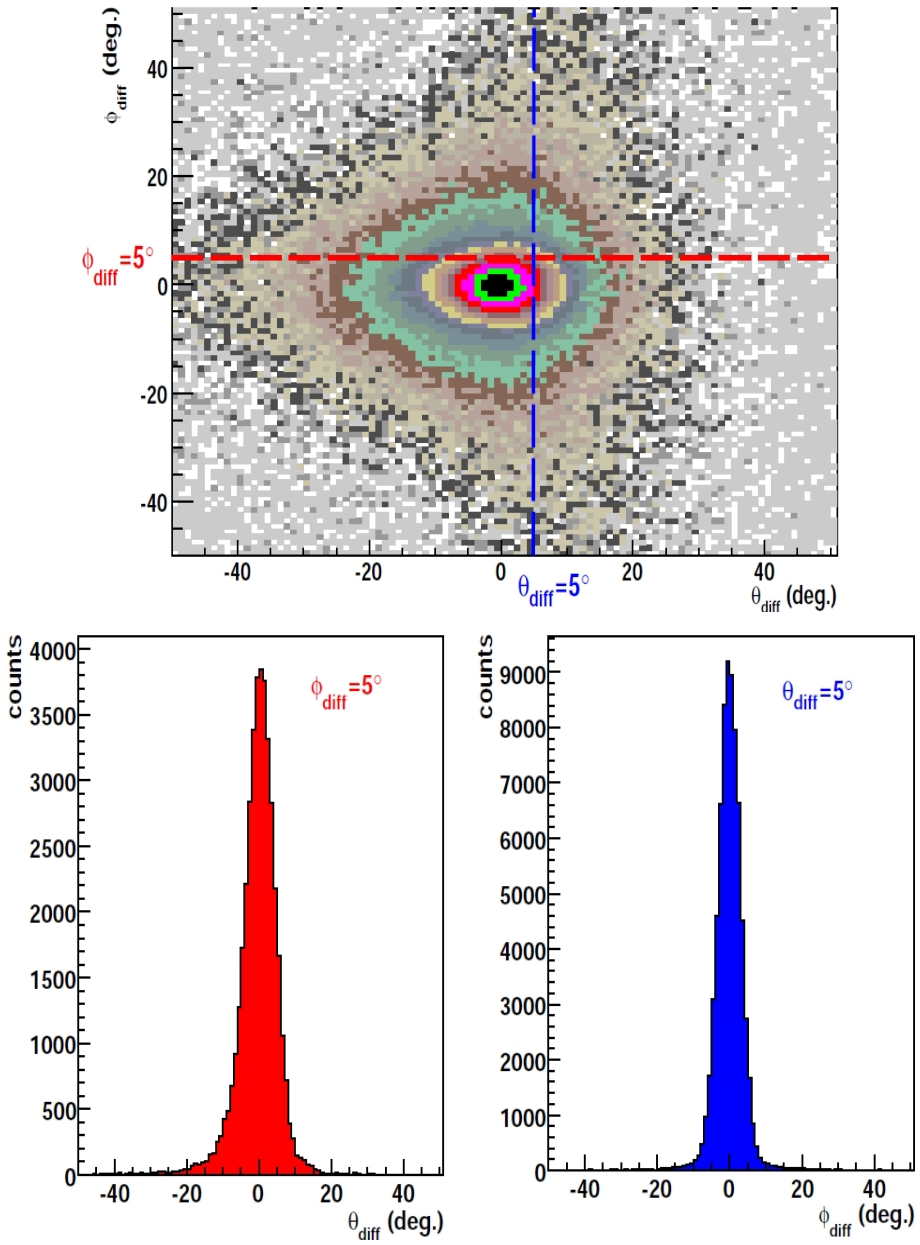

Figure 8.10: 2-dimesional plot of $\delta\phi$ vs. $\delta\theta$ (top), with projections of each axis (bottom).

so that the magnitude of the observed asymmetry is the effective analysing power, which wil account for dilution due to the resolution of the detectors and background processes.

180 million $p\pi^0$ events were generated and input to the simulation, equally divided between positive and negative helicity assignments. The output was analysed with the analysis described above to reconstruct the reaction kinematics and polarimeter scattering angles. The plot of ϕ_{diff} vs. θ_{diff} was then drawn, and elliptical exclusion regions of various sizes were tested. Events for which

$$\frac{\theta_{diff}^2}{R_{\delta\theta}^2} + \frac{\phi_{diff}^2}{R_{\delta\phi}^2} \geq 1 \tag{8.12}$$

satisfy the cut (Figure 8.11).

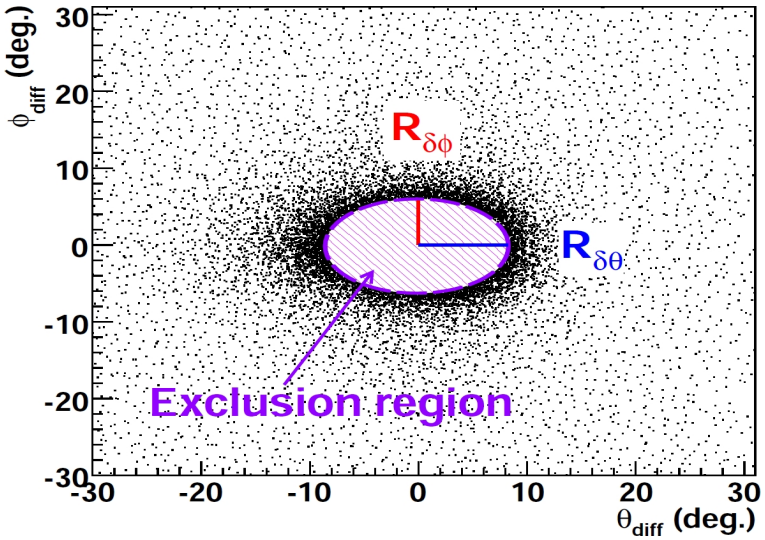

Figure 8.11: An elliptical exclusion region, defined by $R_{\delta\phi}$ and $R_{\delta\theta}$, reduces the large Coulomb background of events with small angular deflections.

The beam helicity asymmetries were then formed, and the effective analysing power was determined by a fit to a sinusoid (Figure 8.12). The size of the ellipse was varied from $R_{\delta\phi}$=0,1,2,...,20° and $R_{\delta\theta}$=0,1,2,...,18°. The optimal cut size was chosen so that the fractional error in the fitted asymmetry σ_A/A_{eff} was minimised. This quantity was calculated for each of the 20×18=360 ellipse sizes and displayed as a function of $R_{\delta\phi}$ and $R_{\delta\theta}$ in Figure 8.13. The amount of dilution varies with energy and angle, so event selection was optimised by carrying out

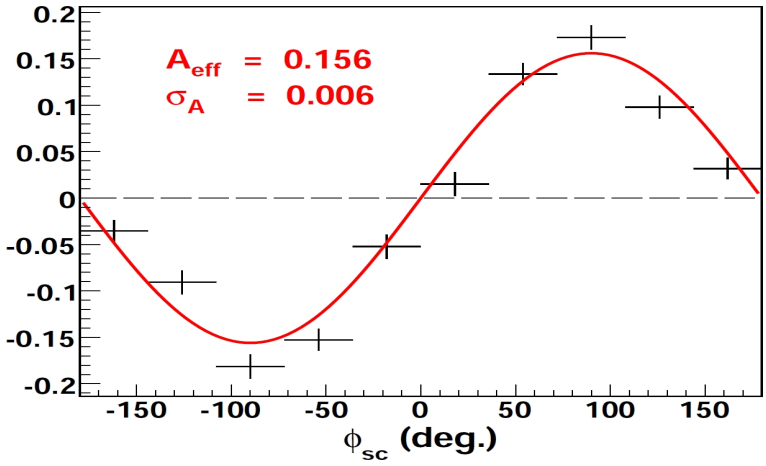

Figure 8.12: Simulated beam helicity asymmetry, shown as a function of ϕ_{sc} and fit with a sinusoid. The fitted amplitude is the effective analysing power.

this process in bins of reconstructed proton energy T_p and angle θ_{rec}. The entire phase space (100<T_p <1050 MeV, 0< θ_{rec} <60°) was divided into kinematic regions defined by a 50 MeV wide energy range and a 5° wide angular bin, and 2-dimensional ϕ_{diff}-θ_{diff} plots were generated for each division.

The values of $R_{\delta\phi}$ and $R_{\delta\theta}$ corresponding to the minimum of the surface in Figure 8.13 were found recursively using an iterative procedure over all angular bins for a fixed energy range. At the initial angular bin of 0< θ_{rec} <5°, test values of $R^0_{\delta\phi}$=5 and $R^0_{\delta\theta}$=5 were initially chosen. A fit function M(x,y) was defined as having a Gaussian distribution in both dimensions

$$M(x,y) = -e^{-\frac{1}{2}\left(\frac{x-R^0_{\delta\theta}}{\sigma_\theta}\right)^2} - e^{-\frac{1}{2}\left(\frac{y-R^0_{\delta\phi}}{\sigma_\phi}\right)^2} + C \tag{8.13}$$

with σ_ϕ=3 and σ_θ=3 approximating the angular resolutions of the detector and C a constant. The minimum of the surface was found using three iterations of a fitting procedure. The domain of M was first restricted to a 10×10 box around (x=$R^0_{\delta\theta}$,y=$R^0_{\delta\phi}$), and the surface was then fit over this area. The means x^1_μ and y^1_μ of the fit result were used to define the centre of a 4×4 box, over which the fit result M^1(x,y) is restricted, and the surface fit again. The procedure is repeated a third time over a 2×2 box, and the means are taken as the values of $R_{\delta\phi}$ and $R_{\delta\theta}$ which minimise the fractional error for the first angular bin.

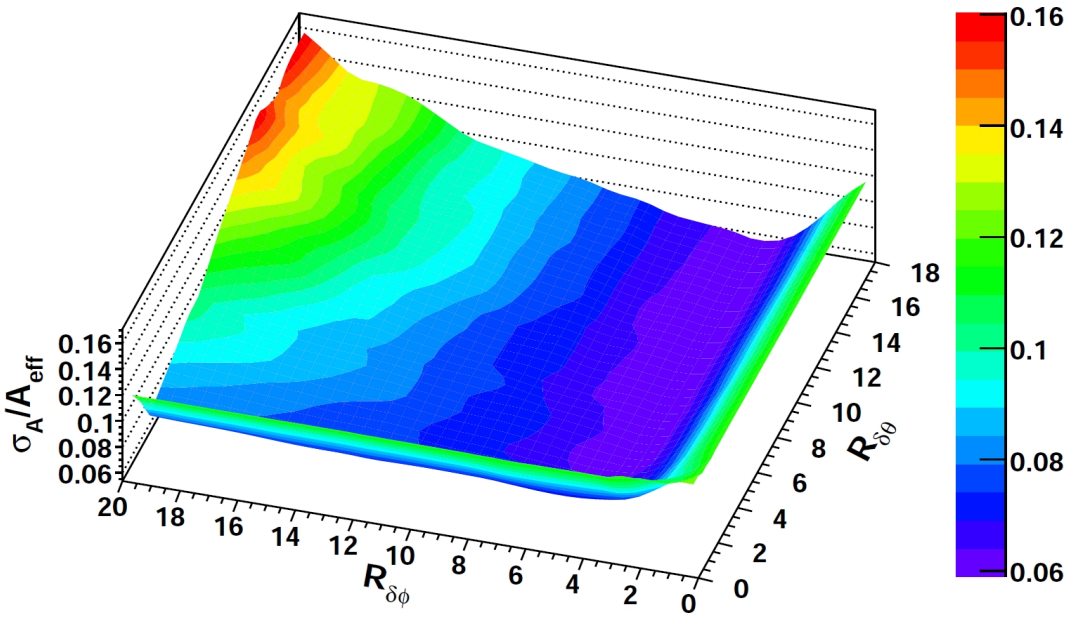

Figure 8.13: A sample surface plot of the figure of merit as a function of $R_{\delta\phi}$ and $R_{\delta\theta}$. The values of $R_{\delta\phi}$ and $R_{\delta\theta}$ for the surface minimum are chosen as the cut size.

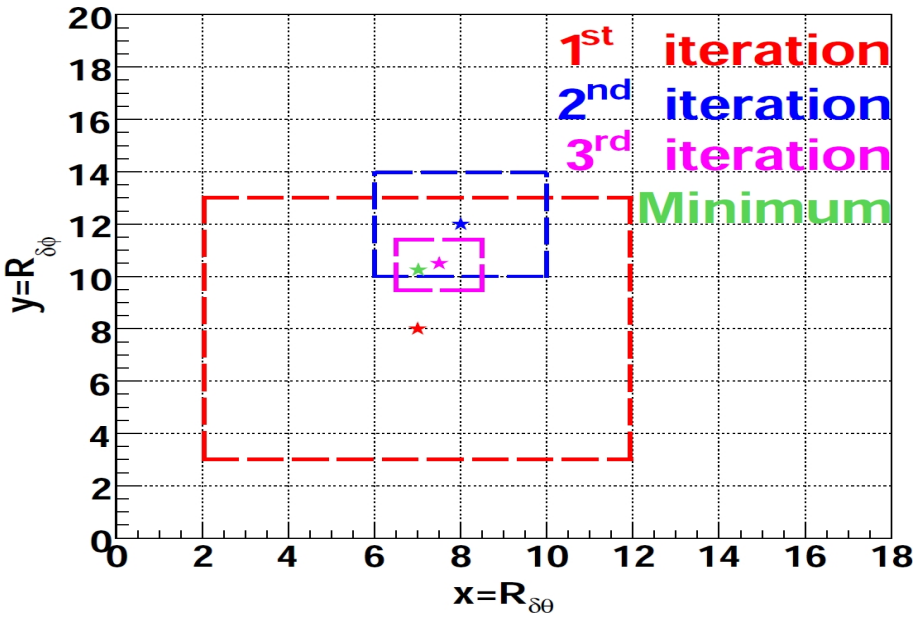

Figure 8.14: Graphical illustration of the iterative process used to fit the minimum of the 2-dimensional ϕ_{diff}-θ_{diff} plot with a fit function which is the sum of Gaussians in x and y.

To ensure a smooth variation of the cut size, the fit results from angular bin i are used as the initial test values for angular bin i+1, and the algorithm is repeated for the remaining bins. At the next energy bin, the process is repeated starting with the test values of $R^0_{\delta\phi}$=5 and $R^0_{\delta\theta}$=5. The results, displayed in Figure 8.15, define the energy and angular dependent elliptical cut.

Plotting ϕ_{sc} vs. θ_{sc} after applying the elliptical cut (Figure 8.16) demonstrates the effectiveness of this selection method in suppressing small angular scattering while preserving the ϕ_{sc} dependence of θ_{sc}.

8.5 Overview of Nuclear Scattered Event Sample for $\gamma p \rightarrow p\pi^0$

A total of $\sim 2.0 \times 10^6$ nuclear scatters were obtained, with a polarimeter acceptance of $\sim$7% in the simulation. The angular distribution and beam energy spectrum of accepted events are shown in Figure 8.17. The bremsstrahlung cross-section varies as $1/E_\gamma$ while the $p\pi^0$ cross-section also falls with increasing energy, resulting in a higher photon flux at lower beam energies. The π^0 centre of mass angular distribution shows a significant acceptance between 50-160°.

The effectiveness of the elliptical cut can be assessed using the simulation. Simulated data where the analysing power was set to 1 were generated and analysed as described above. The deviation from 1 in the resulting beam helicity asymmetries (Figure 8.18) gives an estimate of the dilution due to background, and is graphed as a function of beam energy and centre of mass angle in Figure 8.19. Of the set of events which pass all selection cuts, 58% are estimated to have had a nuclear scatter in the polarimeter.

The reduction in the size of the asymmetry (corresponding to an increase in dilution) observed for θ_{CM} between 110-130° reflects the reduced resolution in θ_{sc} achieved in this region. In Figure 8.20(a), the simulated scattering angle θ_{MC} is compared to the θ_{sc}, the angle calculated in the analysis, as a function of θ_{CM} for events which have scattered in the graphite. The resolution is then obtained by taking projections along the θ_{CM} axis and fitting with a Gaussian. The widths of each projection are displayed in Figure 8.20(b). The resolution increases up to θ_{CM} $\sim$130° before dropping sharply beyond 140°. The significant improvement in resolution is due to forward boosted nucleons scattering in the upstream cap into

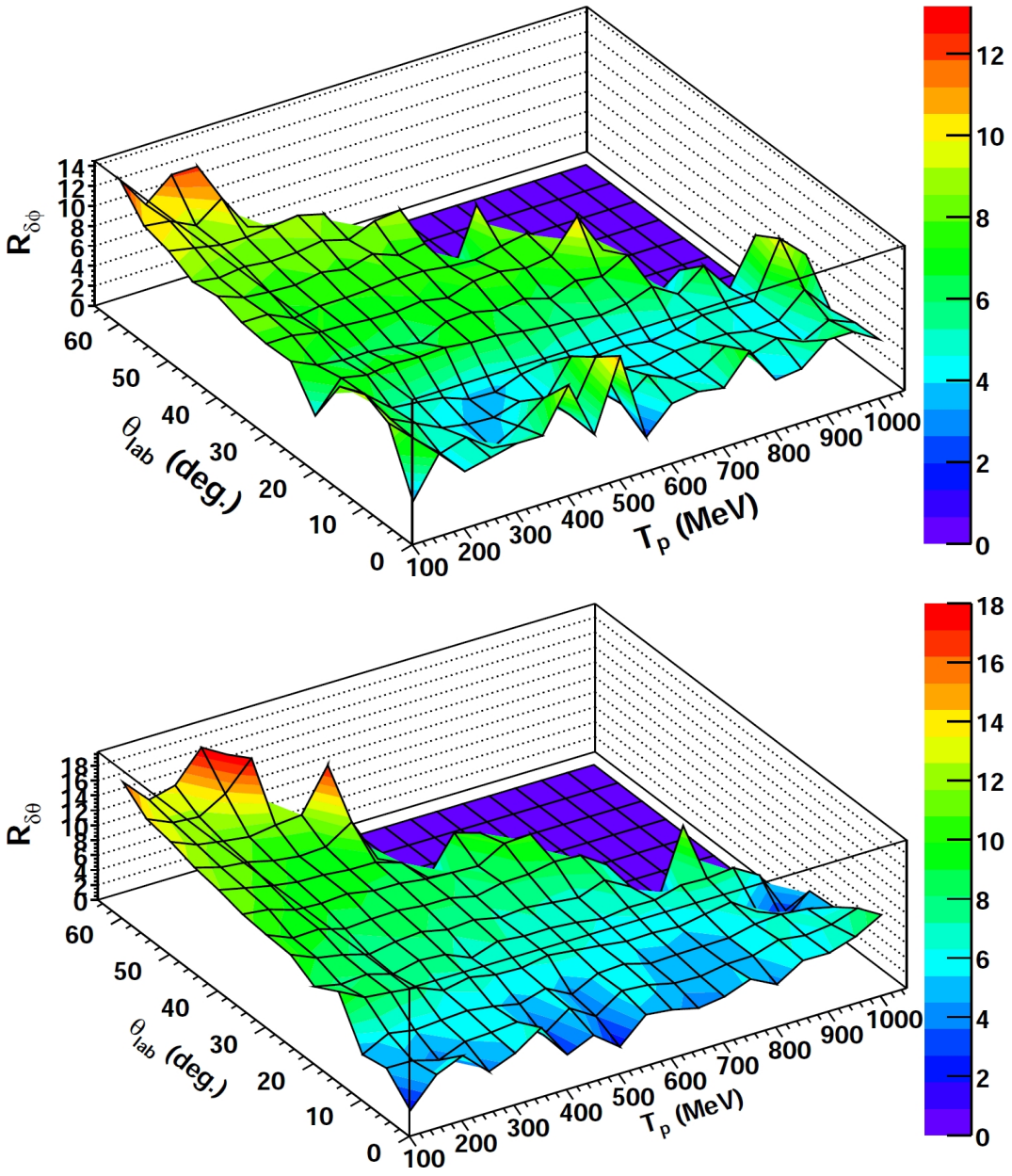

Figure 8.15: Values of $R_{\delta\phi}$ (top) and $R_{\delta\theta}$ (bottom) which optimise the fractional error in the effective analysing power, shown as a function of θ_{lab} and the kinetic energy of the recoil proton.

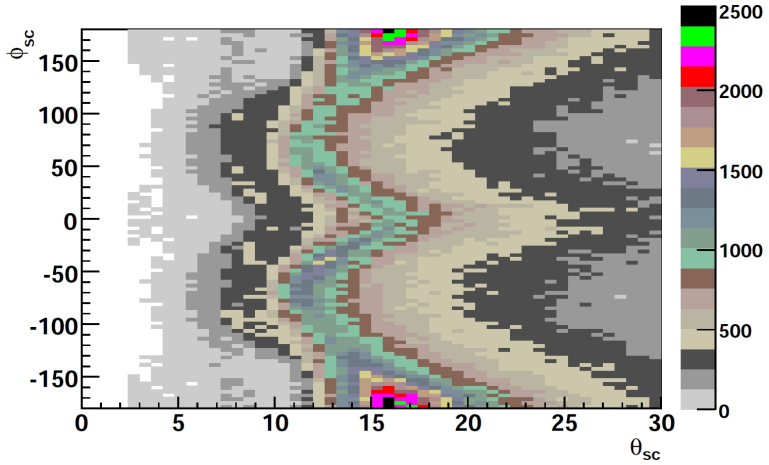

Figure 8.16: The scattering angles ϕ_{sc} and θ_{sc} after applying the elliptical cut.

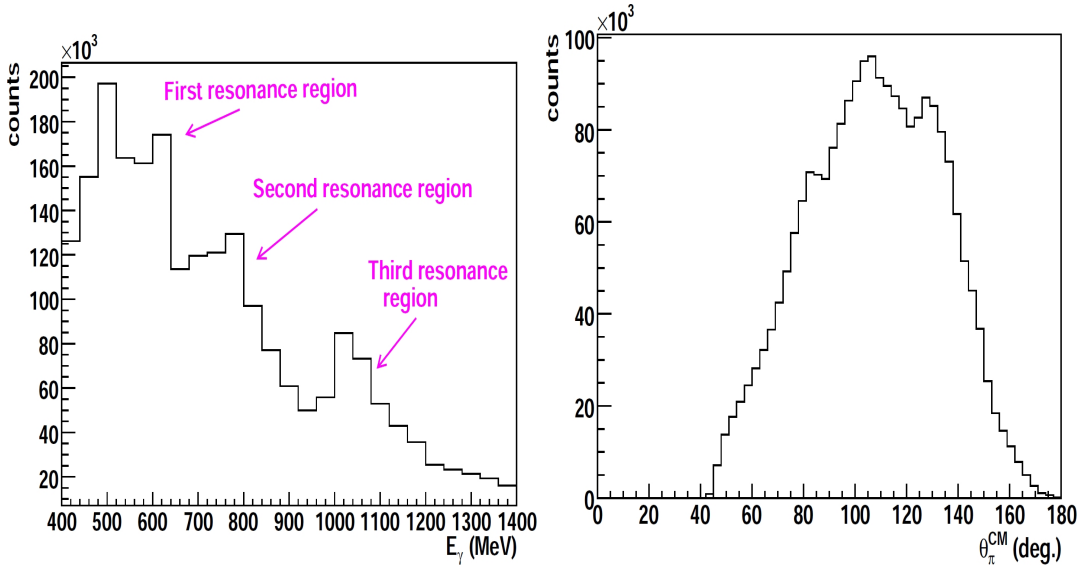

Figure 8.17: Photon beam energy spectrum (left) and centre of mass distribution (right) for nuclear scattered events in the $\gamma p \rightarrow p\pi^0$ reaction.

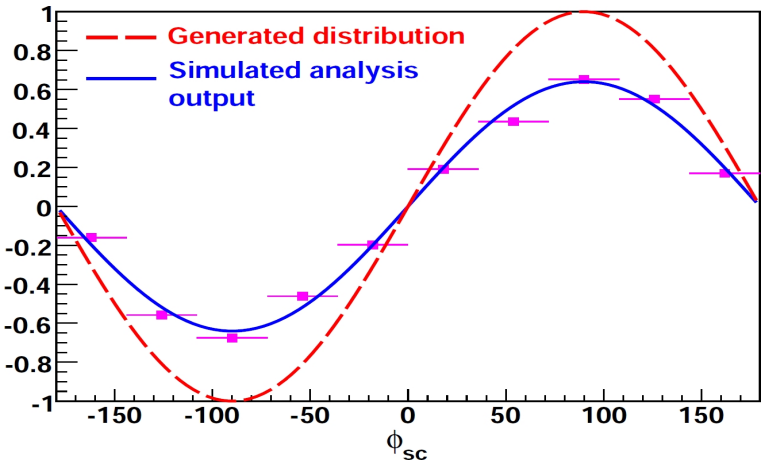

Figure 8.18: The dilution factor is obtained by analysing simulated data where the analysing power has been set to 1. The reduction from 1 in the resulting beam helicity asymmetries indicates the signal to background ratio.

TAPS. Located ∼1.5 meters away from the target, TAPS provides a significant improvement in the reconstruction of the scattering angle.

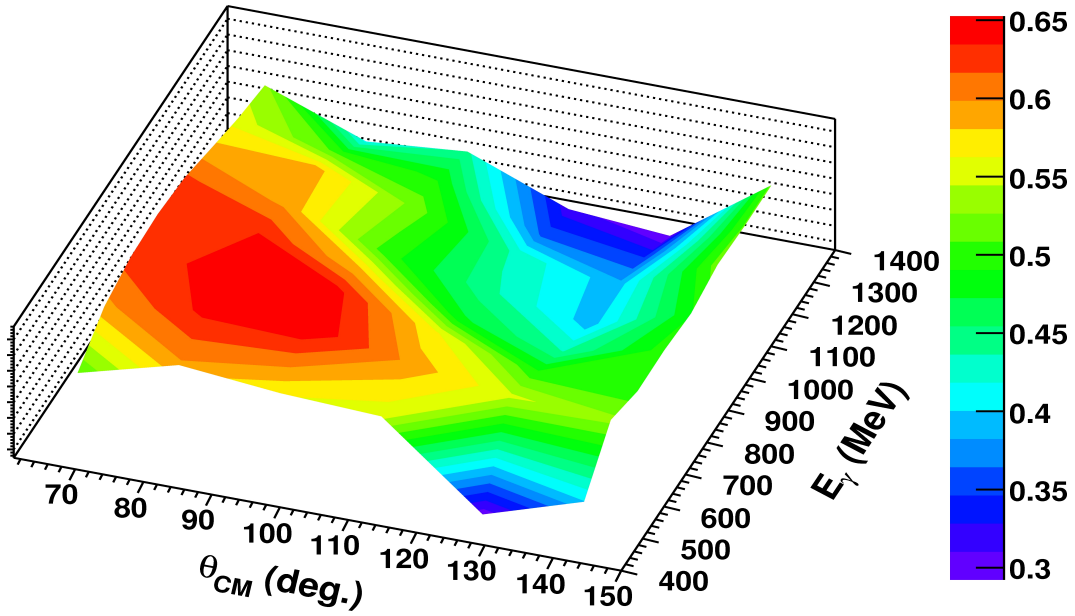

Figure 8.19: Dilution factor as a function of centre of mass angle and photon beam energy.

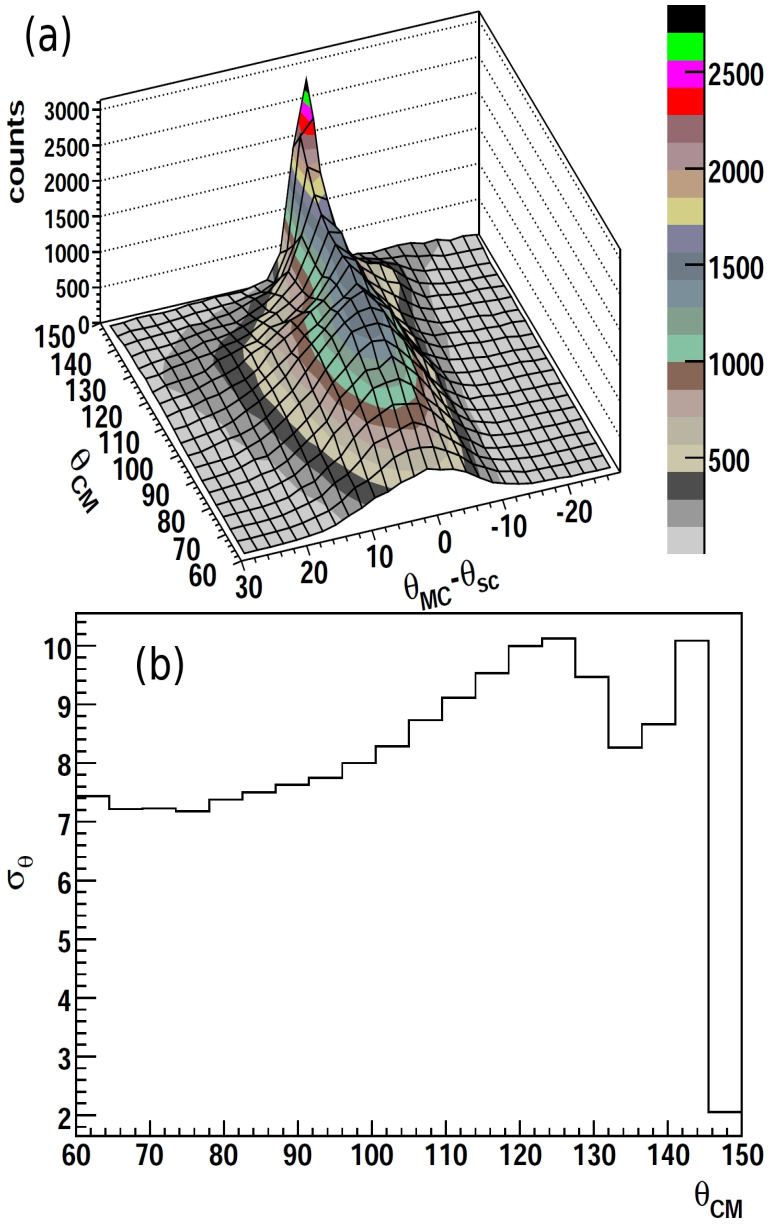

Figure 8.20: (a)The difference between the actual scatter angle θ_{MC} and the calculated scatter angle θ_{sc}, plotted as a function of θ_{CM}. (b)Taking projections along the θ_{CM} axis and fitting with a Gaussian reveals a θ_{CM} dependence of the resolution in θ_{sc}.

8.6 Summary of Nuclear Scattered Events for $\gamma p \rightarrow p\eta$

The procedure outlined above can be easily adapted to analysis of the $\gamma p \rightarrow p\eta$ reaction, with the η decaying to 2 photons with a branching ratio of $\approx$39% (compared to the 99% branching ratio for the $\pi^0 \rightarrow 2\gamma$ decay). The 2γ invariant mass cut is then centred on the η mass of 547 MeV when reconstructing the reaction (Figure 8.21). Due to the different phase space of the reaction channel, the optimisation of the elliptical cut for selecting nuclear scatters must be repeated (Figure 8.22).

Approximately 125,000 nuclear scattered $p\eta$ events were observed after random subtraction, with a polarimeter acceptance estimated at 5%. The kinematic distributions of these events are shown in Figure 8.23. Around 49% of events which pass the elliptical cut have had a nuclear scatter in the polarimeter. Beam helicity asymmetries are then formed from these events.

8.7 Empty Target Subtraction

The yield of events classified as nuclear scatters includes a contamination from events produced from the walls of the target. This contribution is measured by analysing empty target data with the same analysis as for production running. The random subtracted empty target yield is then scaled by a factor calculated from the ratio of tagger hits from full target and empty target run periods. The empty target background accounted for approximately 16% of accepted nuclear scattered events (Figure 8.24), and this contribution was subsequently subtracted off.

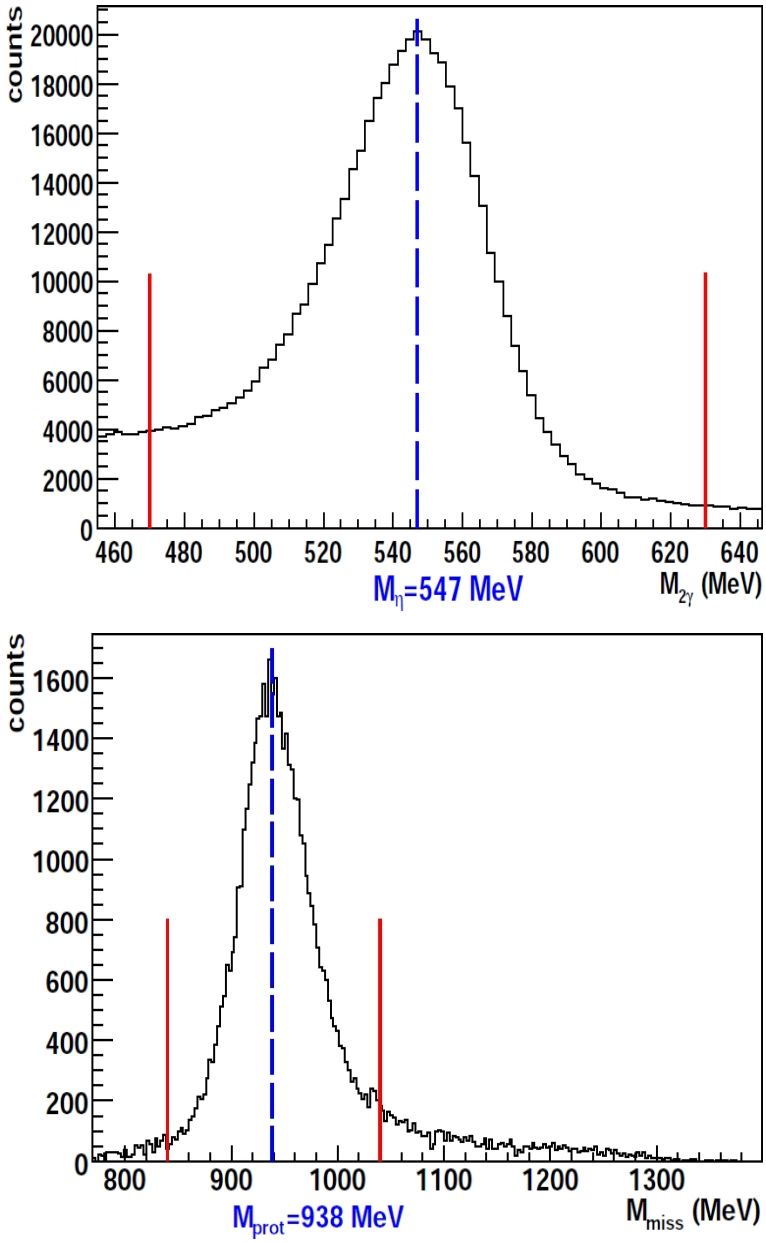

Figure 8.21: Invariant 2 photon mass distribution (top), where the limits of the cut are 470-620 MeV, and missing mass plots (bottom). The limits of the missing mass cut are 840-1040 MeV.

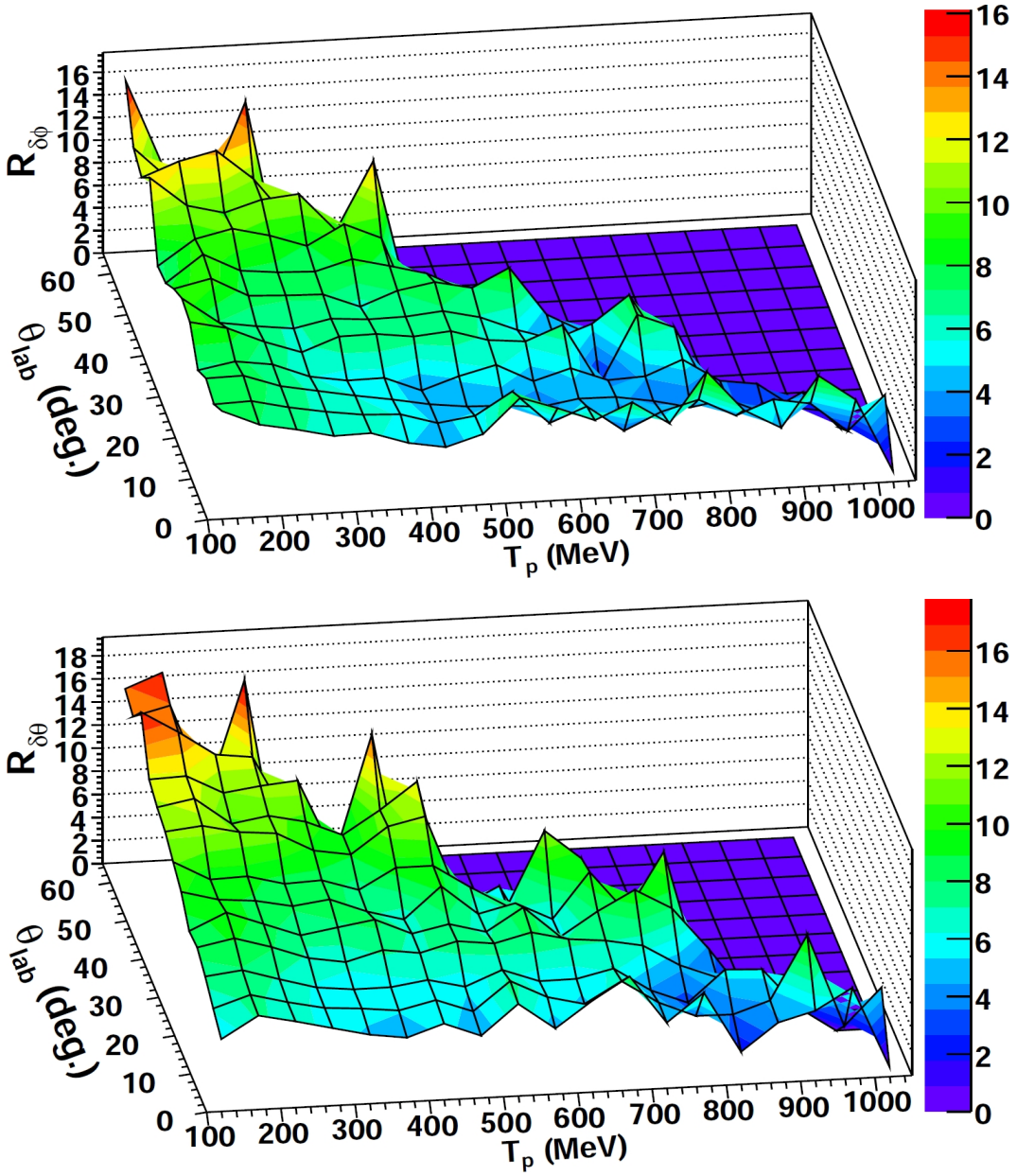

Figure 8.22: Optimised values of $R_{\delta\phi}$ (top) and $R_{\delta\theta}$ (bottom) for the $\gamma p \rightarrow p\eta$ channel.

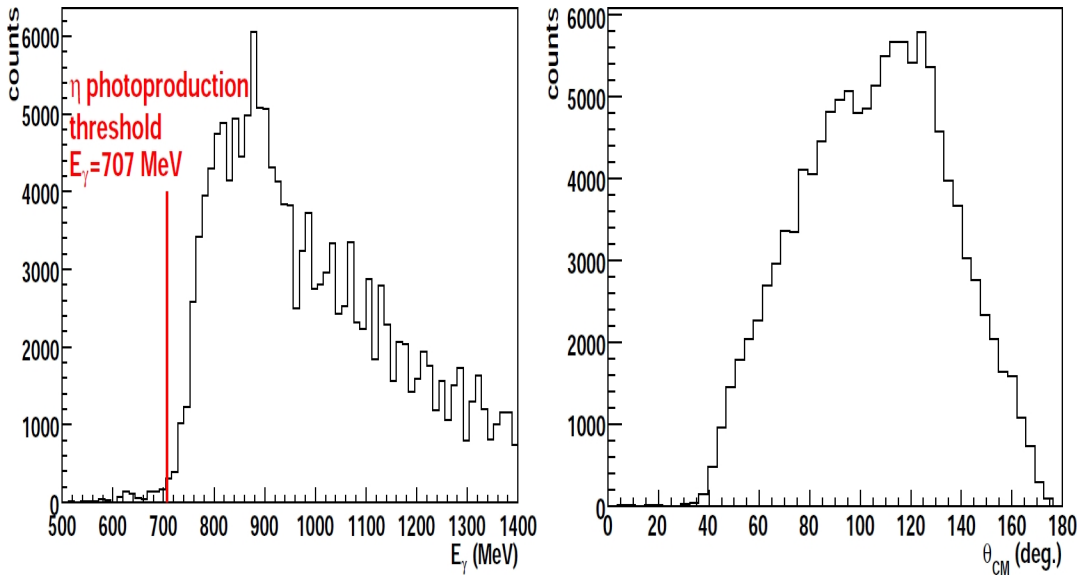

Figure 8.23: Photon beam energy spectrum and centre of mass distribution for nuclear scatters in the $\gamma p \rightarrow p\eta$ channel.

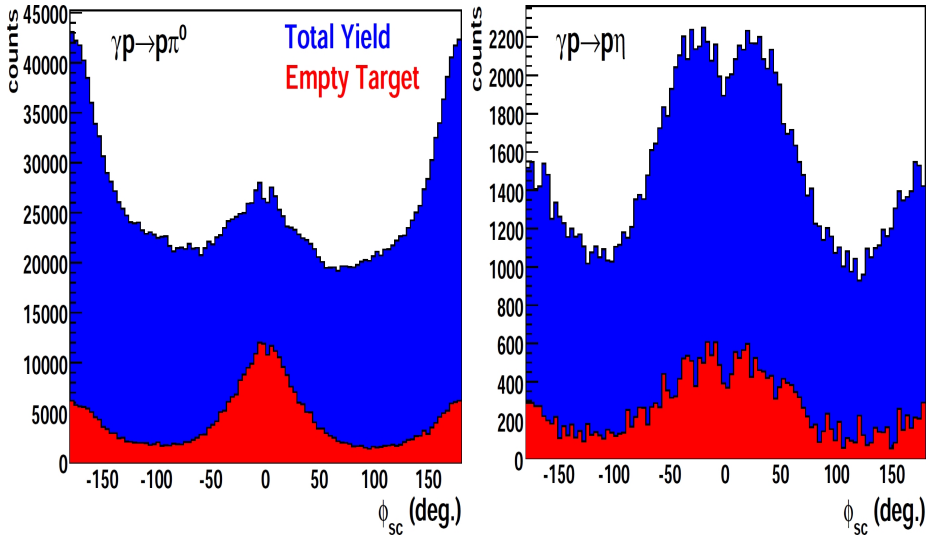

Figure 8.24: Empty target contribution to the ϕ_{sc} spectrum of nuclear scattered events for the $p\pi^0$ (left) and $p\eta$ (right) reactions. The empty target contribution (red) is subtracted off from the full yield (blue) before forming beam helicity asymmetries.

Chapter 9

Beam Helicity Asymmetries

9.1 Extracting C_x

The azimuthal distribution for secondary scattering of protons in the polarimeter is

$$N(\theta_{sc},\phi_{sc}) \quad = \quad N_0(\theta_{sc})\{1 + A(\theta_{sc})\,[P_y \cos\phi_{sc} - P_x \sin\phi_{sc}]\} \tag{9.1}$$

where $N_0(\theta_{sc})$ is the number of detected protons that scattered with polar angle θ_{sc}. This term depends on the polarimeter acceptance $\Omega(\theta_{sc},\phi_{sc})$ and the pion acceptance $K(\theta_\pi,\phi_\pi)$ and is related to the total number of protons scattered by the analyser $N_{sc}(\theta_{sc})$ by

$$N_0(\theta_{sc}) = \Omega(\theta_{sc},\phi_{sc})K(\theta_\pi,\phi_\pi)N_{sc}(\theta_{sc}) \tag{9.2}$$

The polarisation measurement was made over a range of θ_{sc}, so that the polar angle dependence of Equation 9.1 is integrated out

$$N(\phi_{sc}) = N_{sc}\{1 + A_{eff}\,[P_y \cos\phi_{sc} - P_x \sin\phi_{sc}]\}\Omega(\phi_{sc})K(\phi_\pi) \tag{9.3}$$

where A_{eff} is the effective analysing power of the scattering reaction.

Exact knowledge of the acceptance can be avoided by forming the beam helicity asymmetry. The azimuthal yields for each helicity state is then given by

$$N^{\pm}(\phi_{sc}) = N_{sc}\{1 + A_{eff}\,[P \cos\phi_{sc} \mp P_x \sin\phi_{sc}]\}\Omega(\phi_{sc})K(\phi_{sc}) \tag{9.4}$$

Taking the difference between the helicity distributions isolates the P_x component

$$N^- - N^+ = 2N_{sc}(A_{eff}P_x \sin\phi_{sc})\Omega(\phi_{sc})K(\phi_{sc}) \tag{9.5}$$

while the sum is equal to

$$N^- + N^+ = 2N_{sc}(1 + A_{eff}P_y\cos\phi_{sc})\Omega(\phi_{sc})K(\phi_{sc}) \tag{9.6}$$

The beam helicity asymmetry is the quotient of these distributions

$$\frac{N^- - N^+}{N^- + N^+} = \frac{A_{eff}P_x\sin\phi_{sc}}{1 + A_{eff}P_y\cos\phi_{sc}} \tag{9.7}$$

where the acceptances cancel out. For recoil protons produced with a photon beam with circular polarisation $P_\gamma^\odot$, the transverse momentum components are

$$P_x \;=\; P_\gamma^\odot C_x, \qquad P = P_y$$

Thus, C_x is the fraction of the initial beam polarisation transferred to the recoiling proton, and the single polarisation observable P is the induced polarisation in the $\hat{\mathbf{y}}$ direction of the scattering frame. Substituting these values into Equation 9.7 gives

$$\frac{N^- - N^+}{N^- + N^+} = \frac{A_{eff}P_\gamma^\odot C_x\sin\phi_{sc}}{1 + A_{eff}P\cos\phi_{sc}} \tag{9.8}$$

Asymmetries were formed as a function of ϕ_{sc} in bins of photon energy and centre of mass angle. Extraction of C_x required calculating the beam polarisation, determining the analysing power, and P, and subsequently fitting the data asymmetries using Equation 9.8. These quantities, and the fitting procedure to obtain C_x, are discussed in Sections 9.2-9.5.

9.2 Beam Polarisation

As mentioned in Section 5.1.2, the degree of circular polarisation of the photon beam is calculated directly from the tagged photon energy E_γ by

$$P^\odot = \frac{P_{MAMI} \times E_\gamma \times (E_{MAMI} + \frac{1}{3}(E_{MAMI} - E_\gamma))}{E_{MAMI}^2 + (E_{MAMI} - E_\gamma)^2 - \frac{2}{3}E_{MAMI} \times (E_{MAMI} - E_\gamma)} \tag{9.9}$$

where E_{MAMI}=1508 MeV is the energy of the MAMI electron beam and P_{MAMI} is the longitudinal polarisation of the electron beam. This was measured by the MAMI beam operators using a Mott polarimeter [95] installed at the beam source (Figure 9.1). The polarimeter consisted of a 15 μm thick gold target with

a diameter of 16 mm. Elastically scattered electrons were detected by two Si-diodes fixed at a scattering angle of 164° on either side of the scattering plane. The count rates R for each detector (1,2) and each electron helicity (+,-) were measured, and the asymmetry A is obtained from the ratio $Q=(R_1^+R_2^-)/(R_1^-R_2^+)$

$$A = \frac{1-\sqrt{Q}}{1+\sqrt{Q}} \tag{9.10}$$

Calculating the asymmetry in this way removed any possible false asymmetries from detection efficiencies, detector solid angular coverages, and any small variation in the beam current as the helicity is flipped. The effective analysing power for electron scattering is calculated [96] and divided out of the measured asymmetry. The reported beam polarisation was 85.5% ±3%(syst.).

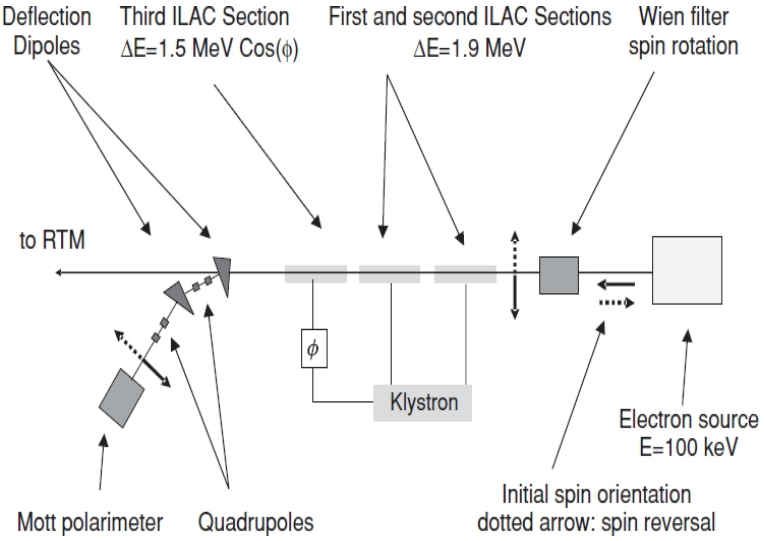

Figure 9.1: The Mott polarimeter [95].

The polarisation was calculated over 125 MeV wide E_γ bins. The polarisations of all photons in a particular bin were calculated and histogrammed, which was then normalised by dividing out the total number of counts. The average polarisation over the bin, $\overline{P^\odot}$, was taken to be

$$\overline{P^\odot} = \sum_{i=1}^{N} n_i x_i \tag{9.11}$$

where N is the number of bins in the polarisation histogram, and n_i and x_i are the number of normalised counts and x_i is the midpoint of the i^{th} bin. A sample calculation is shown in Figure 9.3.

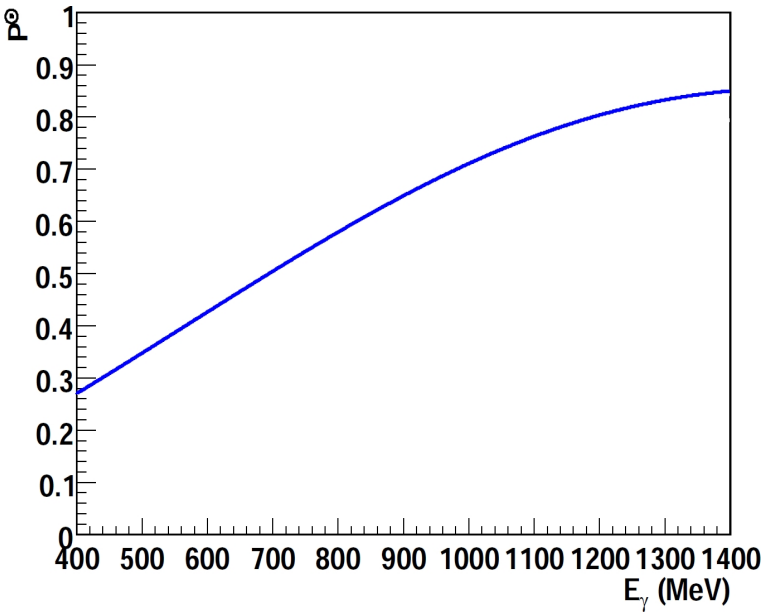

Figure 9.2: Graph of Equation 9.9.

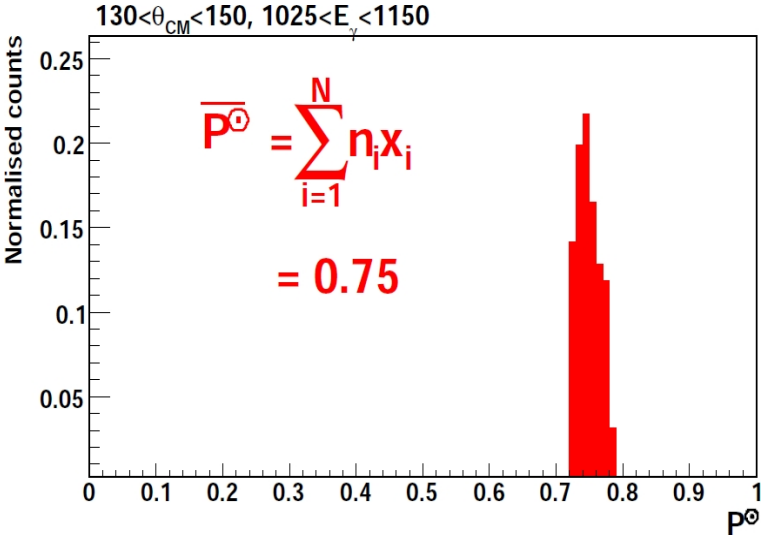

Figure 9.3: Sample polarisation calculation for 100° $< \theta_{CM} <$110°, 1025 MeV$< E_\gamma <$1150 MeV.

9.3 Analysing Power

After the elliptical cut was shaped and implemented in the analysis, the simulated data were re-analysed. The asymmetries in the helicity yields of simulated events were fit with a sinusoid as described in Section 8.4, the amplitude of which is the effective analysing power A_{eff}. Some sample fits are shown in Figure 9.4 in the energy range 775 MeV<E_γ <900 MeV in four different centre of mass angle bins. In some bins, the asymmetry was not fit perfectly by the sinϕ_{sc} function. This was due to the dilution by unscattered events varying with ϕ_{sc}. In particular, the dilution is highest at 0° and 180° due to events originating at the front and back of the 5 cm long target cell.

The effective analysing power is shown as a function of E_γ for the $\gamma p \rightarrow p\pi^0$ reaction in Figures 9.5 and 9.6 and as a function of θ_{CM} in Figures 9.7 and 9.8 for the π^0p channel. The values show a slight rise with increasing E_γ, averaging ∼0.2 across each angular bin in Figures 9.5 and 9.6. In Figures 9.7 and 9.8, the analysing power tends to increase up to θ_{CM} ∼100°, followed by a gradual decline up to 140°. This observation is consistent with the results of the dilution factor shown in Section 8.5. As a higher fraction of nucleons are detected in the tunnel region of the Crystal Ball, the uncertainty of the azimuthal position ϕ_{CB} of the detected particle increases as $1/\sin\theta_{CB}$. Consequently, the reconstruction of the scatter angles in the polarimeter is more uncertain, which reduces the simulated asymmetry. The sharp rise at θ_{CM}=150° reflects the increase in angular resolution achieved when nucleons are detected in TAPS at forward angles.

The effective analysing power for the $\gamma p \rightarrow p\eta$ reaction is shown in Figure 9.9 as a function of E_γ. Due to the factor of 10 reduction in the available statistics in the data, the results are presented in fewer angular bins. The effective analysing power is lower compared to the π^0 channel due to a higher dilution factor and the greater kinetic energy of recoiling protons in η photoproduction.

9.4 Single Polarisation Observable P

The induced polarisation P has been measured in several experiments for photon energies up to 1400 MeV[1]. These data points form part of the database of over

[1]References for these experiments can be found on the SAID database [93]

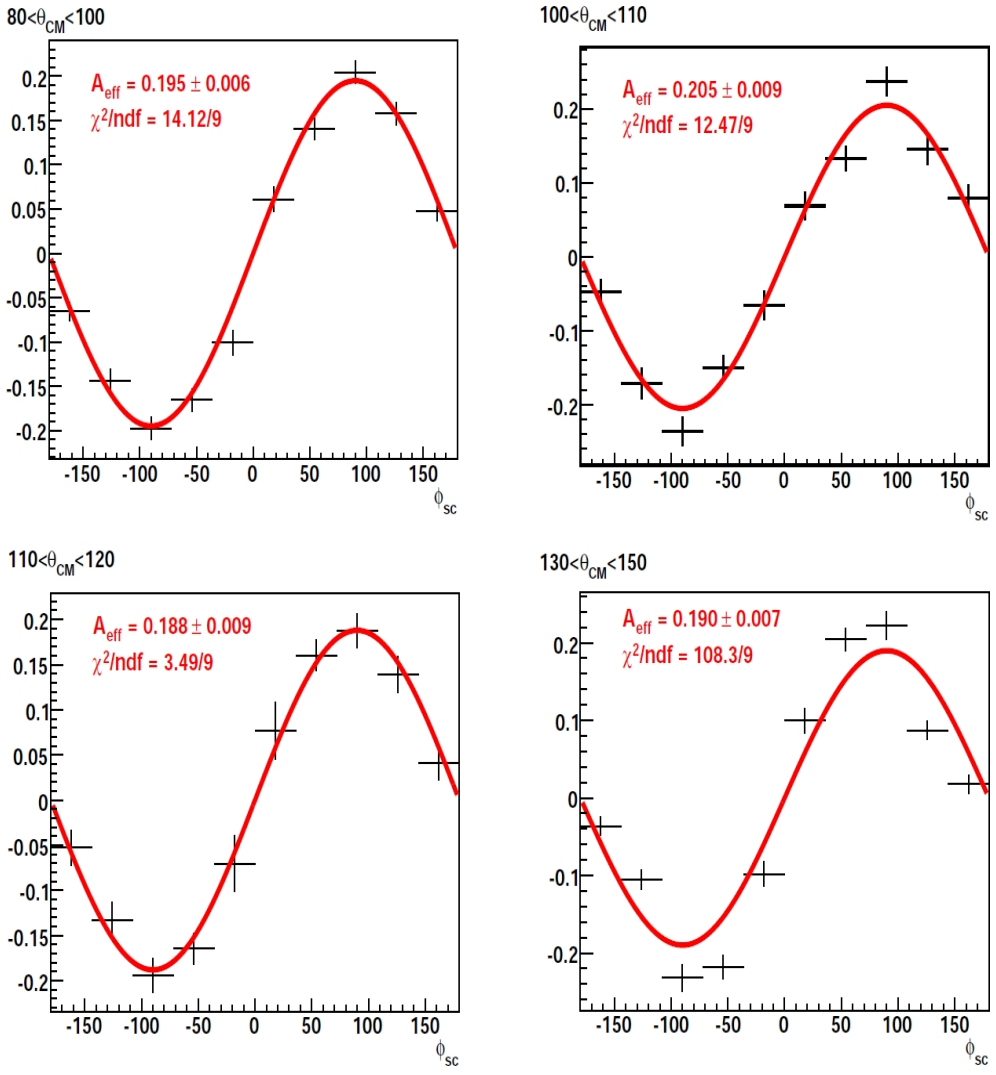

Figure 9.4: Analysing power asymmetries in the range 775 MeV<E_γ <900 MeV.

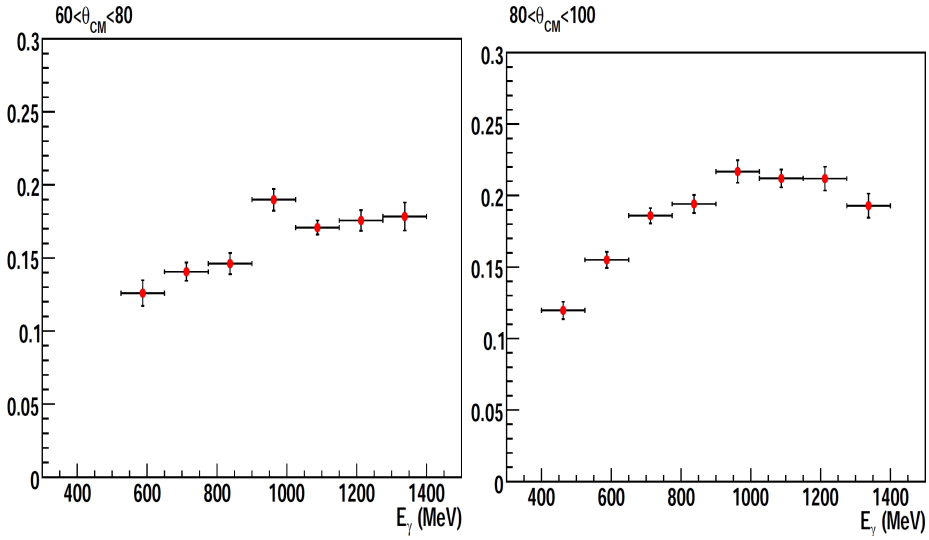

Figure 9.5: Effective analysing power as a function of E_γ for the $\gamma p \rightarrow p\pi^0$ reaction for $60 < \theta_{CM} < 80$.

25000 measurements of polarisation observables in the π^0p reaction channel which the SAID group have used to fit the reaction amplitudes. The fitted amplitudes can then be used to extrapolate values for P across the entire phase space covered by the experimentally obtained sample of nuclear scattered events. The results are displayed in Figure 9.10 for both π^0 and η production.

The determination of P to include in Equation 9.8 in a given bin is similar to the calculation of the beam polarisation. At each value of ϕ_{sc} in the appropriate E_γ and θ_{CM} range, the value of P was read off from Figure 9.10 and put into a histogram. The histogram was then normalised, and the average value $\overline{P}$ was calculated as in Equation 9.11.

The dominance of the sine term in Equation 9.8 in π^0 production can be assessed by considering the product $A_{eff}\overline{P}$. This quantity was calculated at each measurement point and put into a histogram, seen in Figure 9.11(a). The distribution was fit with a Gaussian with parameters μ=-0.055 and σ=0.069. In Figure 9.11, Equation 9.8 has been drawn with $A_{eff}\overline{P}$=0 (blue) and $A_{eff}\overline{P}=\mu\pm2\sigma$ (red) for an arbitrarily chosen value of $A_{eff}P^{\odot}C_x$. The deviation from a pure $\sin\phi_{sc}$ is minimal, and the beam helicity asymmetries consequently exhibit a strong sinusoidal dependence.

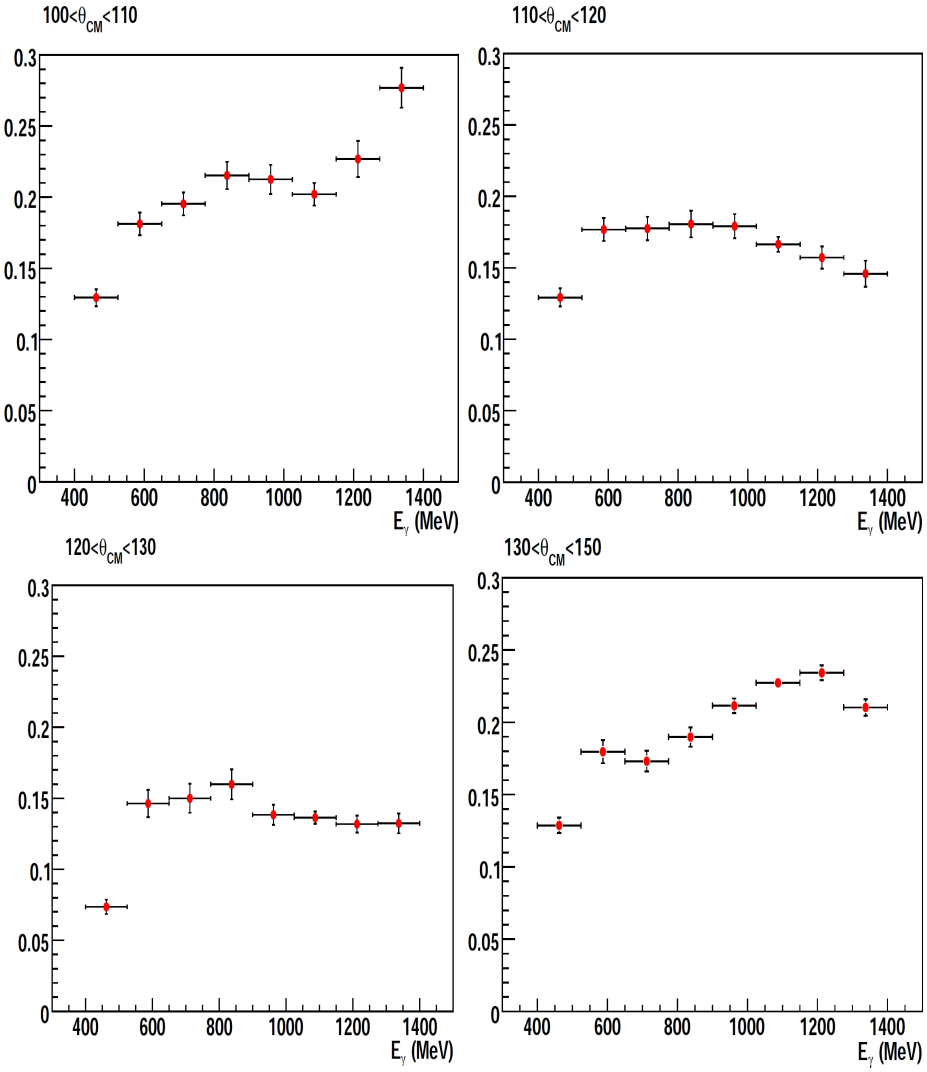

Figure 9.6: Effective analysing power as a function of E_γ for the $\gamma p \rightarrow p\pi^0$ reaction for $100< \theta_{CM} <150$.

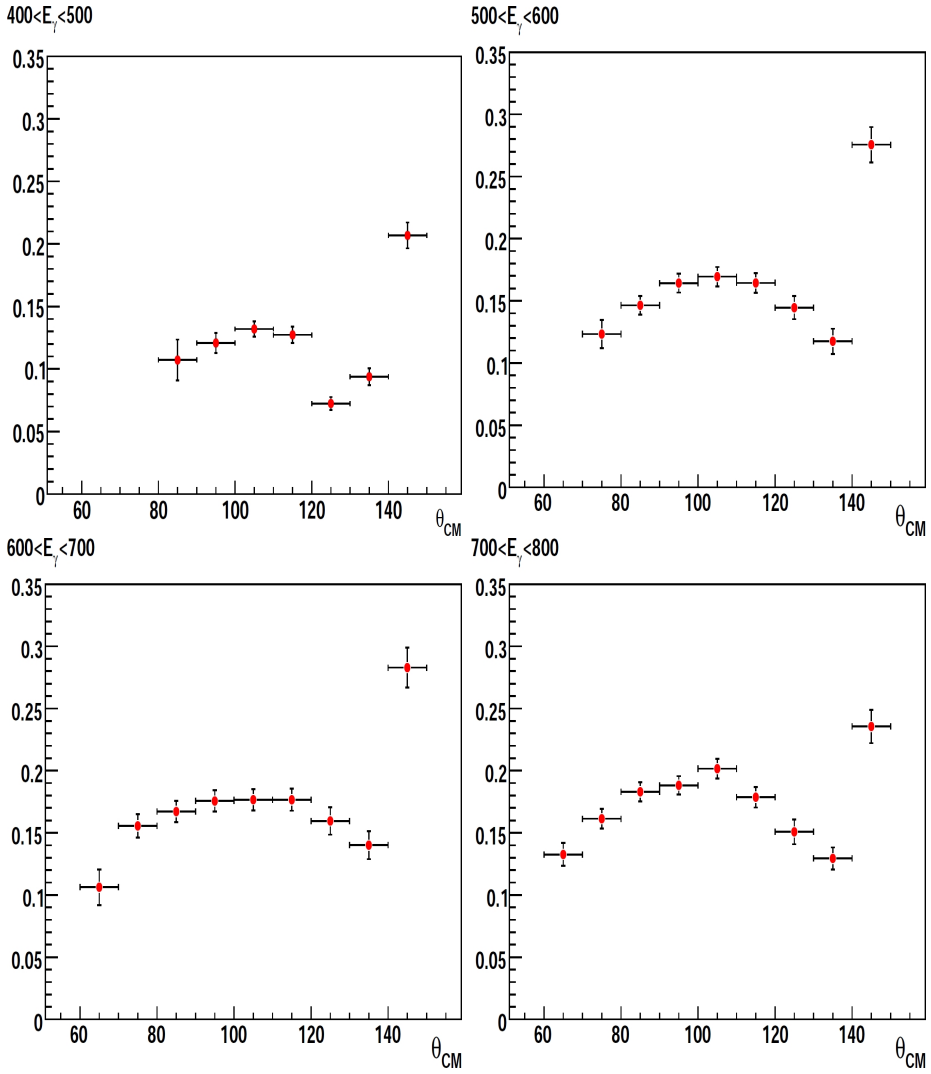

Figure 9.7: Effective analysing power as a function of θ_{CM} for the $\gamma p \rightarrow p\pi^0$ reaction for $400 < E_\gamma < 700$.

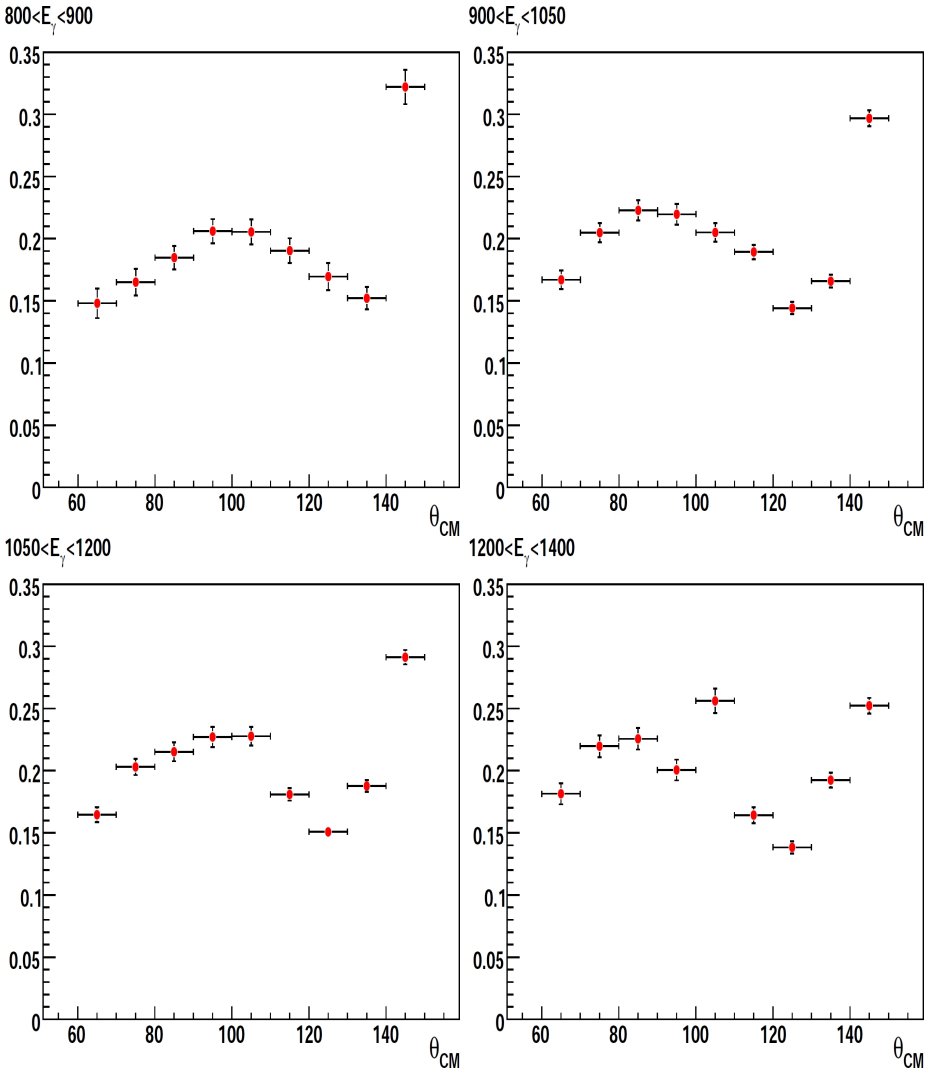

Figure 9.8: Effective analysing power as a function of θ_{CM} for the $\gamma p \rightarrow p\pi^0$ reaction for $800 < E_\gamma < 1400$.

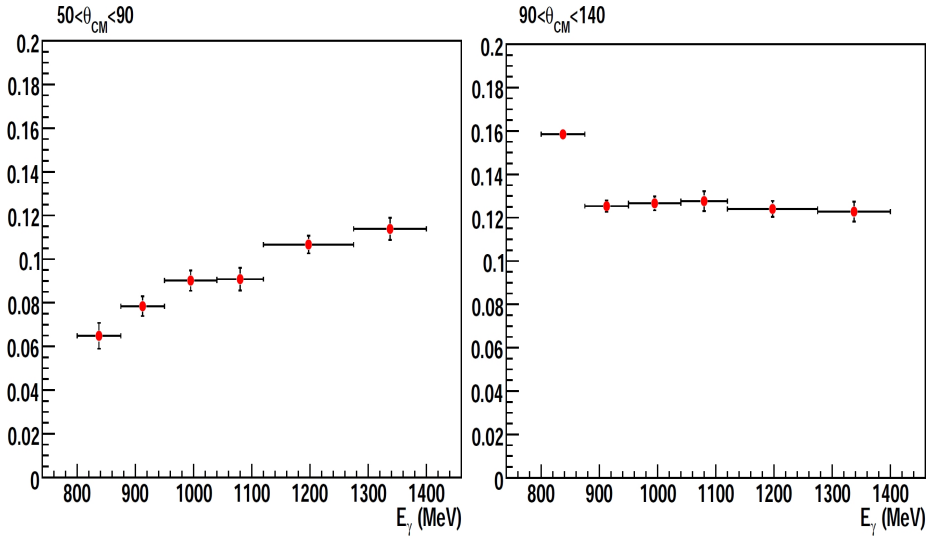

Figure 9.9: Effective analysing power as a function of E_γ for the $\gamma p \rightarrow p\eta$ reaction for $50 < \theta_{CM} < 140$.

9.5 C_x Fitting Procedure

After obtaining the quantities $\overline{P^{\odot}}$, A_{eff}, and $\overline{P}$, the respective parameters in Equation 9.8 were fixed and not permitted to vary in a χ^2 minimisation fit to the data beam helicity asymmetries, some examples of which are shown in Figure 9.12.

An improved fit can be achieved by dividing out the simulated asymmetries from the data asymmetries. The motivation for this method comes from the ϕ_{sc} dependence in the dilution factor resulting from uncertainty in the γp interaction vertex in the target cell. Each data asymmetry histogram was divided by the corresponding simulated asymmetry used to extract the analysing power. This removes the $\sin\phi_{sc}$ dependence of Equation 9.8 and directly cancels out the varying dilution factor

$$f(\phi_{sc}) = \frac{B}{1 + A_{eff}\overline{P}\cos\phi_{sc}}, \qquad B = C_x\overline{P^{\odot}} \tag{9.12}$$

In Figure 9.13, the asymmetries shown in Figure 9.12 have been divided out by the simulated asymmetries and fit with the function in Equation 9.12

Dividing out the ϕ_{sc} dependent dilution in this manner and fitting with Equation 9.12 gave a minor improvement in the χ^2 of the fit results. The χ^2 values

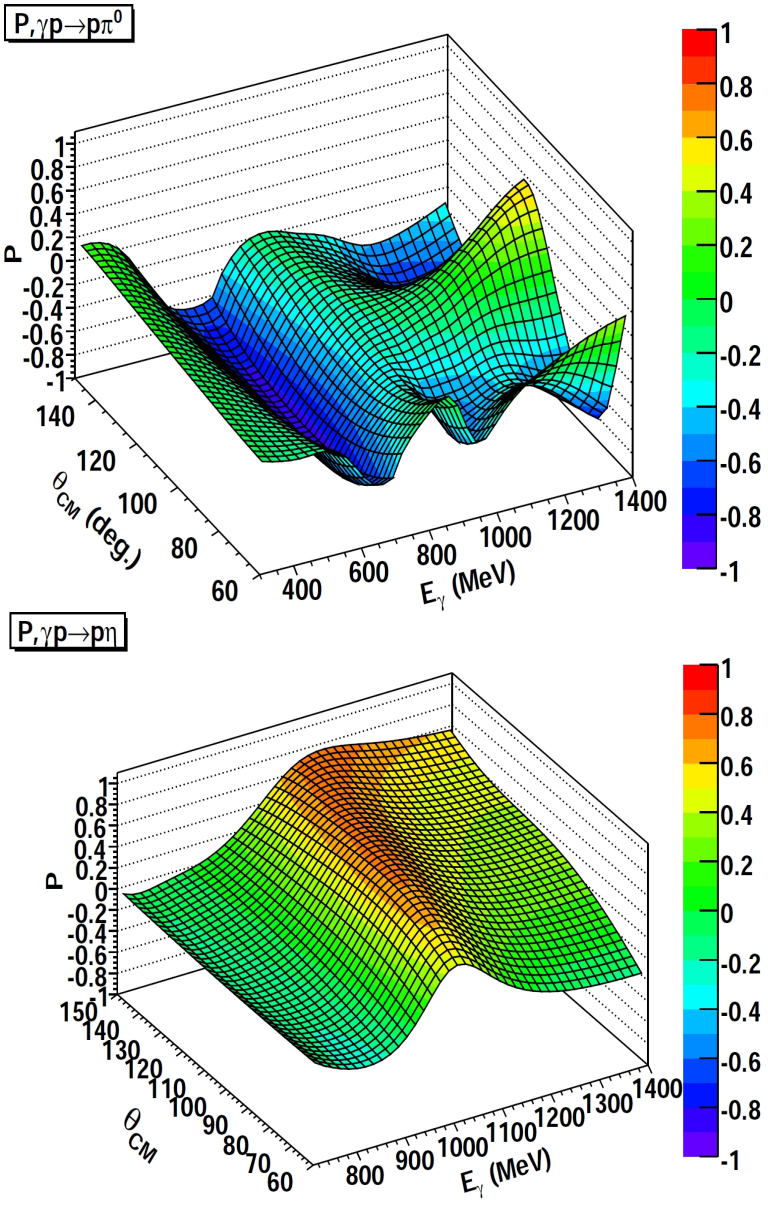

Figure 9.10: Values of P from SAID [93] for π^0 photoproduction (top) and η photoproduction (bottom).

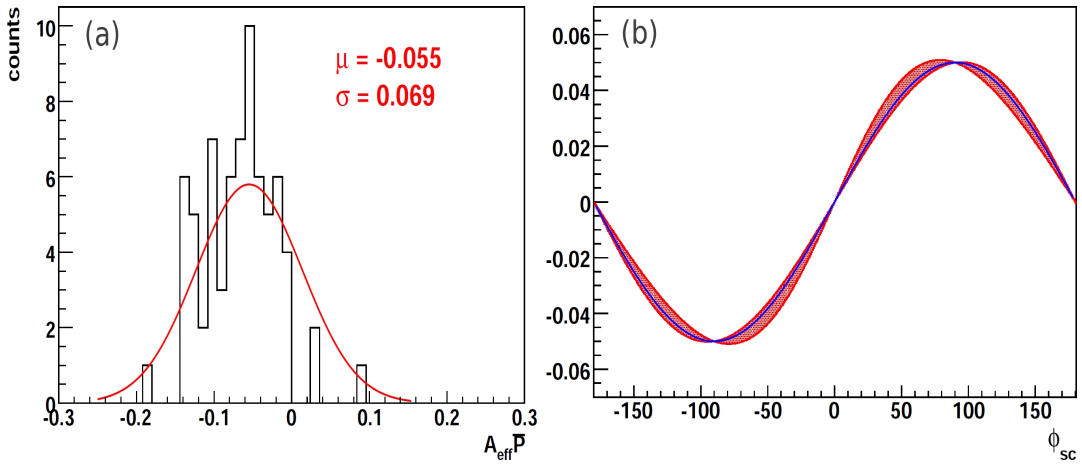

Figure 9.11: (a) Histogram of the quantity PA_{eff} for each measurement point along with a Gaussian fit. (b) Equation 9.8 with $A_{eff}\overline{P}$=0 (blue) and $A_{eff}\overline{P}$=$\mu\pm 2\sigma$ (red).

obtained fitting with the sinϕ_{sc} term and the 'linear' fit function are compared at each measurement point in Figure 9.14.

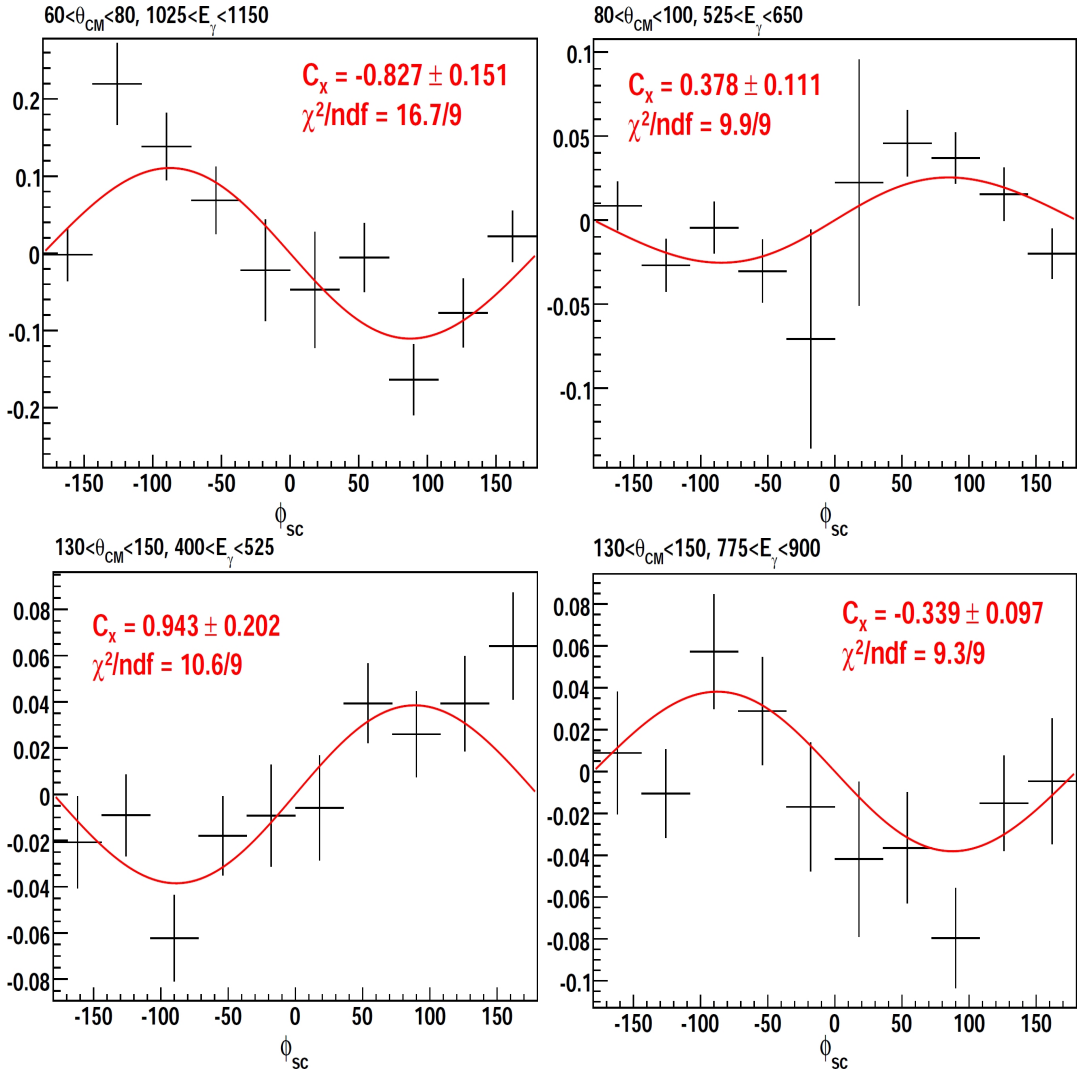

Figure 9.12: Examples of beam helicity asymmetries fit with Equation 9.8.

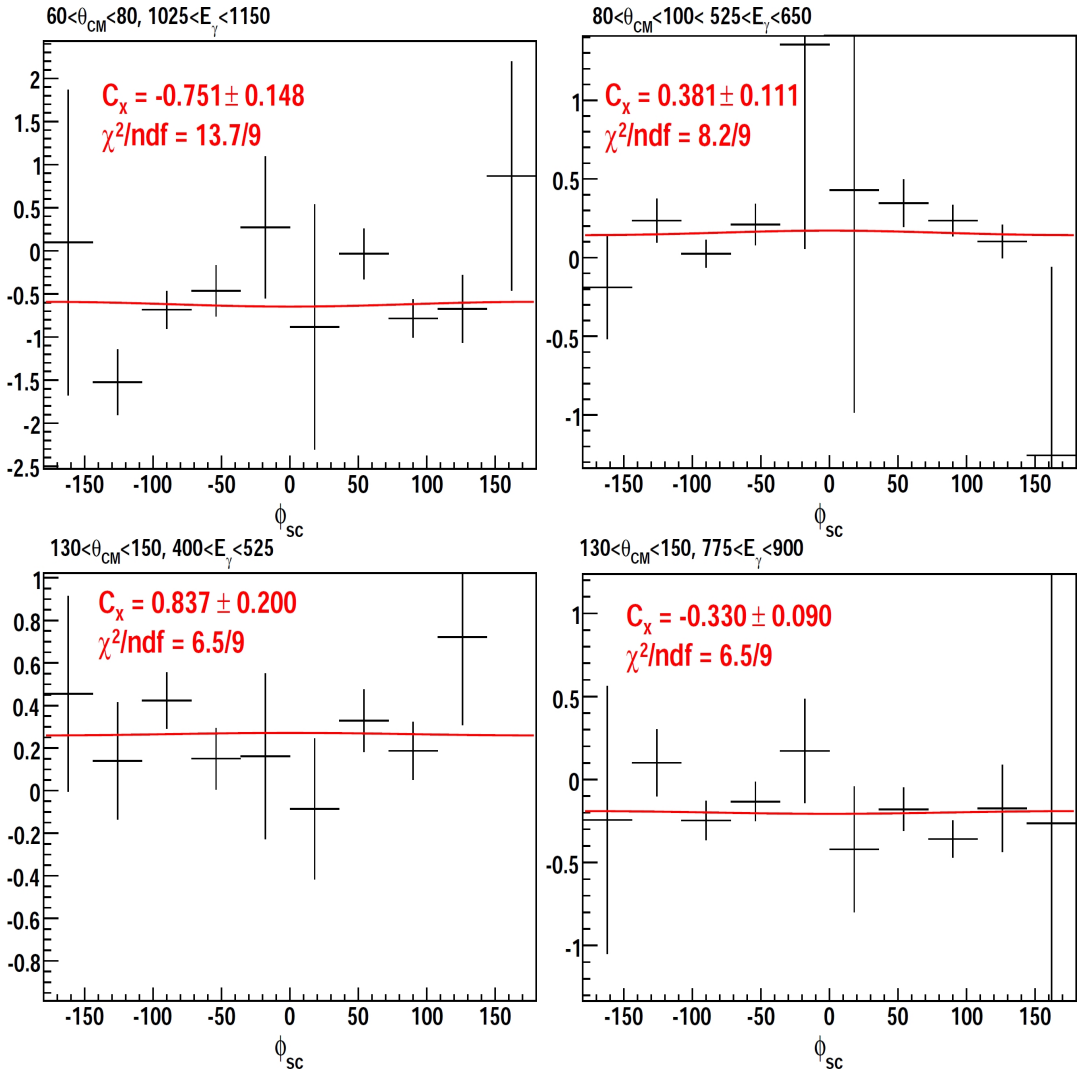

Figure 9.13: The same asymmetries in Figure 9.12 with the corresponding simulated asymmetries divided out and fit with a flat line.

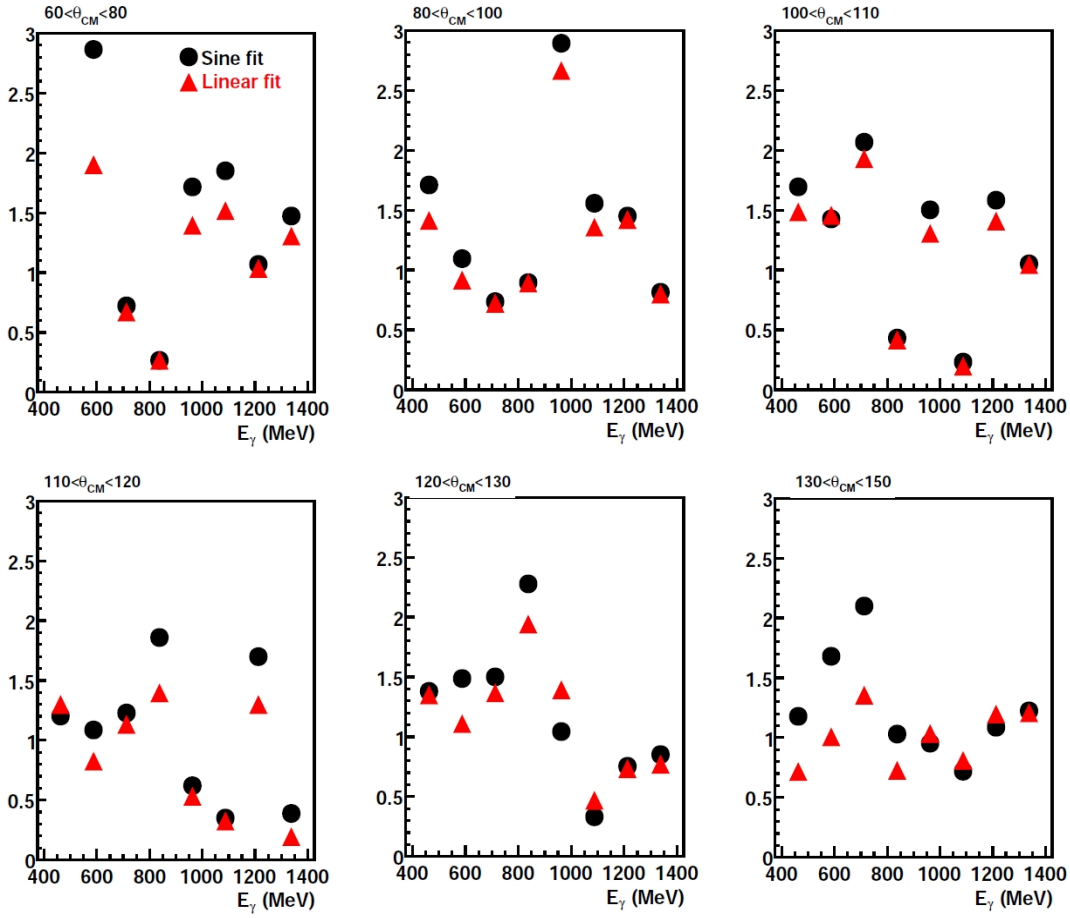

Figure 9.14: Comparison of the χ^2 using the sine fit (circles) and the linear fit (triangles) at each measurement point. The linear fit provides a slight improvement in the fit result.

Chapter 10

Results and Discussion

The systematic uncertainty of the new measurements is examined and quantified in this chapter. The C_x results obtained for π^0 and η photoproduction are then presented in Section 10.2.

10.1 Systematic Uncertainties

The dominant source of systematic uncertainty in these measurements is the calibration of the analysing power. Contributions from other sources, such as background from other reaction channels and false asymmetries, are also assessed.

10.1.1 Analysing Power Parameterisation

The database of p-^{12}C scattering on which the new analysing power parameterisation described in Chapter 7 was sourced from calibrations of carbon polarimeters used in conjunction with tracking detectors placed to track the scattered particles after scattering in the analyser. Therefore, the acceptance and event selection of these experiments would show differences to the present experimental setup. To estimate any resultant effect on the calculated analysing powers, the analysing power parameterisation input to the Geant4 simulation was extended using elastic proton-nucleon analysing powers (Section 7.4.2). These were included to simulate the contributions to the total p^{12}C scattering distribution from events which scatter off a nucleon inside the carbon nucleus. The contribution from such events is most significant at large scattering angles.

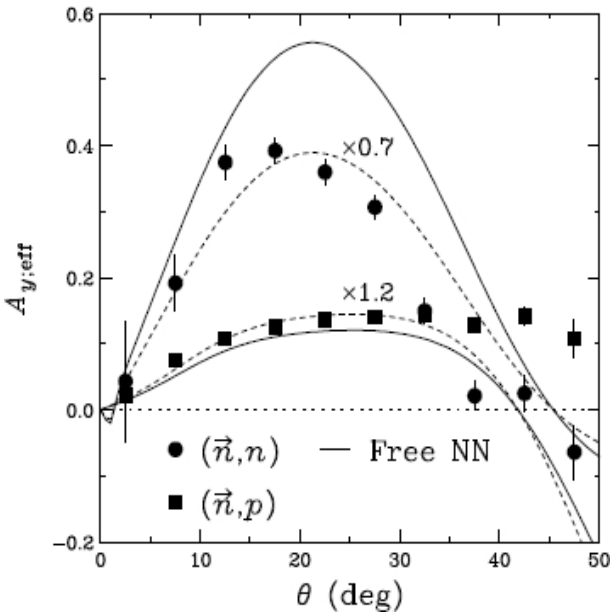

Figure 10.1: Comparison of the free nucleon-nucleon analysing powers to the quasi-elastic n-^{12}C analysing powers [97].

The quasi-elastic n-^{12}C analysing power has been compared to the free neutron-nucleon analysing powers in a previous experiment using a polarised neutron beam [97] at energies ∼200 MeV. The effective analysing powers for neutron and proton final states are shown in Figure 10.1 as a function of scattering angle, compared to the calculated free nucleon-nucleon analysing powers. The effective analysing power of the n-^{12}C reaction with a neutron in the final state has been measured as 70% of the analysing power for free neutron-proton scattering. Because this reduction has not been investigated over a broad energy range, the effect was not included in the scattering model of the present experimental setup. Therefore, the free proton-nucleon analysing powers provided an upper limit on the calibration of the polarimeter at MAMI.

To estimate the systematic uncertainty arising from the analysing power parameterisation, polarised scattering was simulated in two separate simulations; one with the model including the McNaughton based parameterisation for elastic scattering processes with an additional account of the quasi-free proton-nucleon analysing powers (QF) outlined in Chapter 7, while the second model applied the McNaughton based parameterisation (McN) to all events. These two models

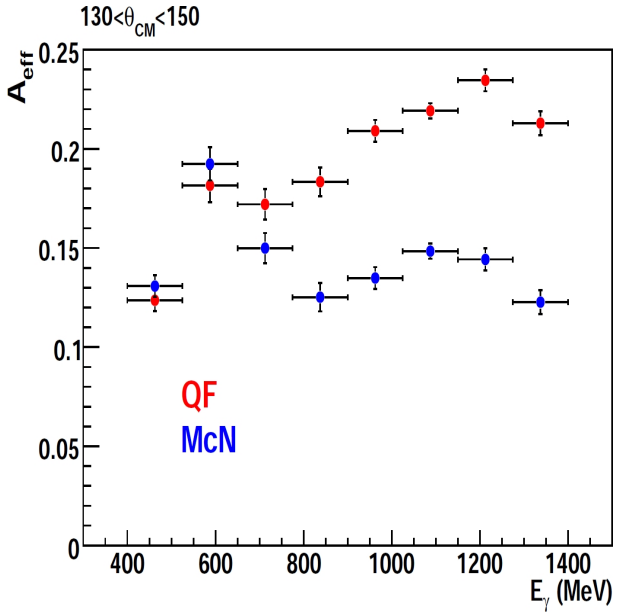

Figure 10.2: Comparison of the effective analysing power for 130< θ_{CM} <150 for both polarised scattering models.

define the boundaries of the polarimeter performance. The results for the two simulations are shown in one of the pion angular bins in Figure 10.2. The outputs were analysed with the same analysis code, and C_x was extracted as a function of θ_{CM} in 9 different E_γ ranges using each model. For each energy bin, the difference of the two C_x values at each point was calculated. The differences were plotted and fit with a flat line (Figure 10.3), the value of which is taken as the systematic uncertainty for the bin.

The final C_x values reported here have been calculated by taking the arithmetic average of the values and statistical uncertainties obtained using each analysing power model. The energy dependent systematic uncertainty, shown in Figure 10.3, is greatest at higher E_γ where the cross-section for inelastic scattering is higher.

10.1.2 Consistency of C_x with Scatter Angle

For a given kinematic range, the azimuthal asymmetry was formed over all values of θ_{sc}. The analysing power and acceptance are integrated over all values of θ_{sc}

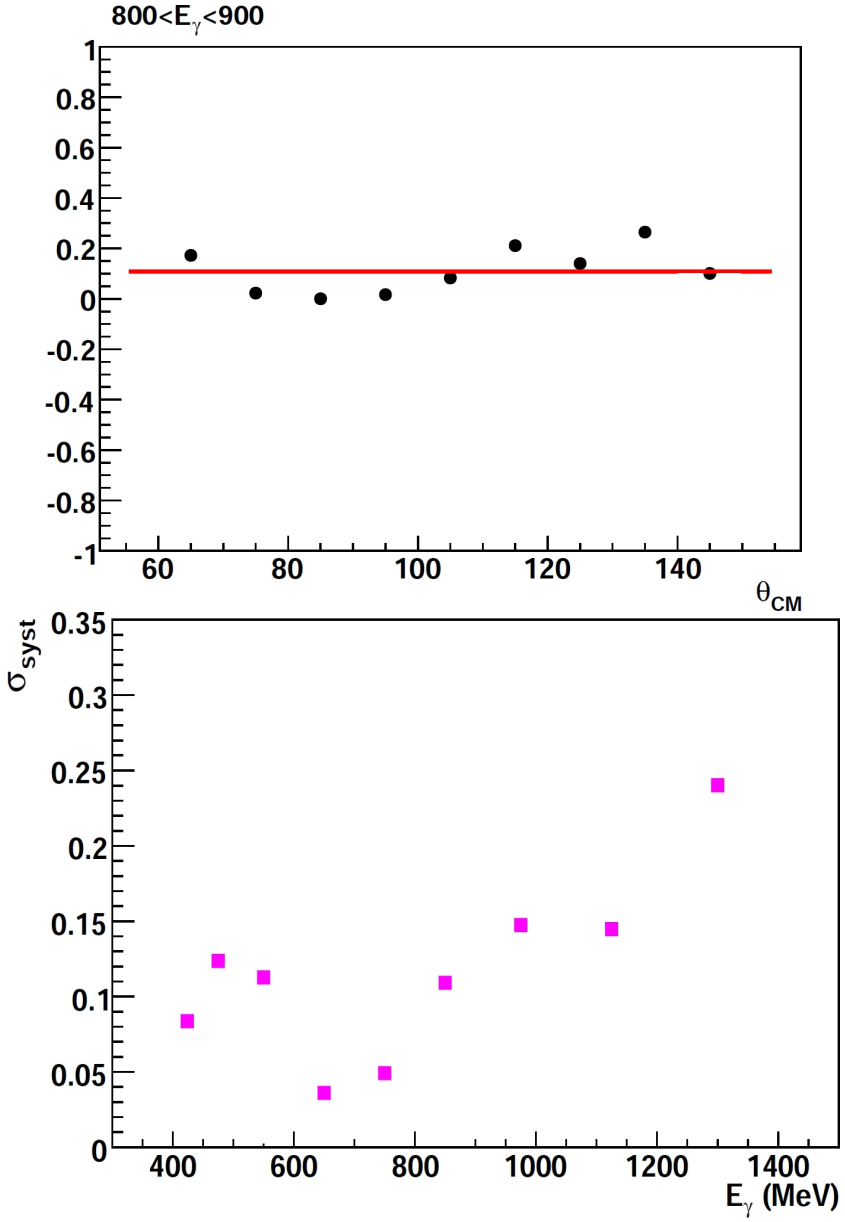

Figure 10.3: (top) The difference between the values of C_x obtained using both analysing power parameterisations were plotted as a function of θ_{CM} in bins of E. The systematic uncertainty was estimated by fitting the differences with a flat line. (bottom) The quoted systematic uncertainty, displayed as a function of E_γ.

to give an effective analysing power for the bin. Calculating C_x as a function of θ_{sc} thus provides a means of determining the stability of the C_x results.

To maximise the available statistics, C_x has been plotted as a function of θ_{sc} over as wide a kinematic region as possible where C_x was observed to have little variation. This is shown in Figure 10.4 for 120< θ_{CM} <150 and E_γ >800 MeV using the QF and McN models of polarised scattering. Up to θ_{sc} ∼20°, C_x is indeed observed to be constant and the points are well fit by a flat line as expected. However, for the region θ_{sc} >20°, C_x diverges to ∼0 for both scattering models. Azimuthal asymmetries are therefore diluted by accepting events with larger scattering angles. Based on this observation, events with θ_{sc} >20 were excluded from the analysis.

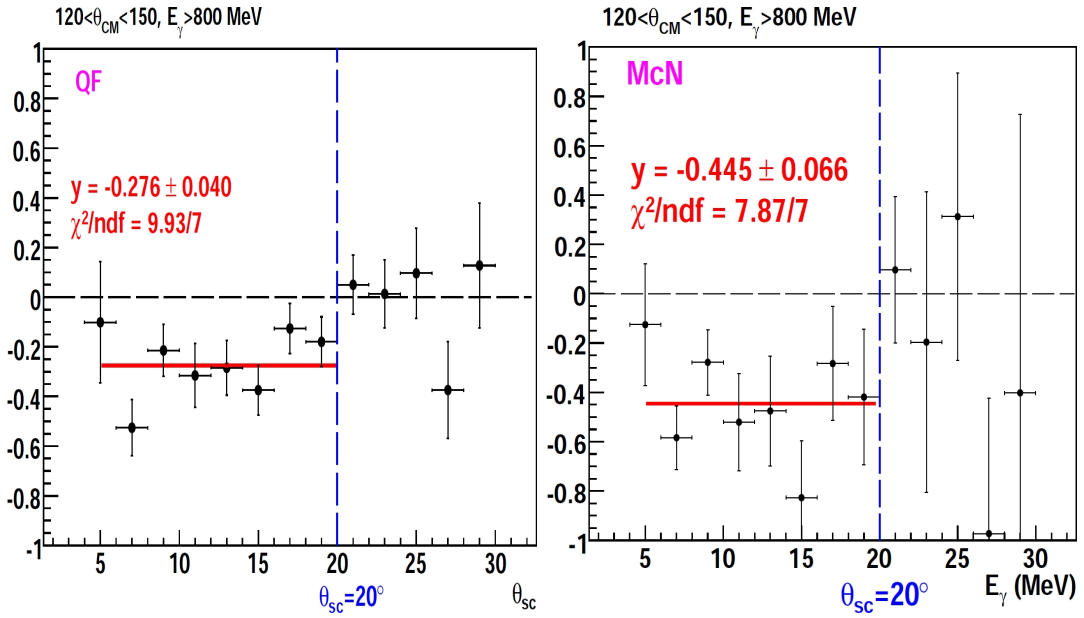

Figure 10.4: C_x extracted as a function of θ_{sc} using the QF (left) and McN (right) models of polarised scattering.

This finding is consistent with the upper bound on θ_{sc} used in the experiments measuring the p-^{12}C analysing power as well as in the analysis of the previous C_x measurement at Jefferson Lab [60] and A1 at MAMI [98]. The latter reference employed a similar polarimeter scattering thickness as the present work and shows a similar fall off of the analysing power beyond ∼20° (Figure 10.5). It is clear that more work is necessary to fully understand the behaviour of the analysing power

at larger scattering angles. However, the smaller yield of these angles means that the region can be excluded without significantly affecting the statistical accuracy of the current results.

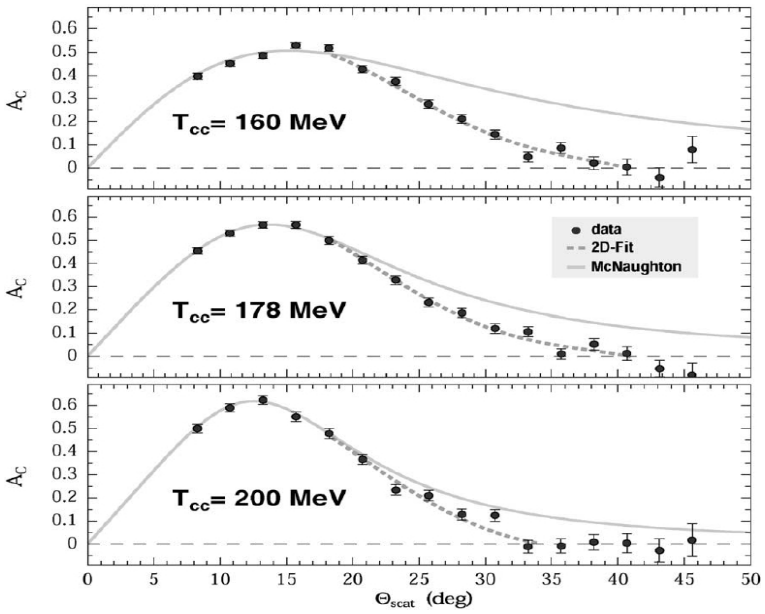

Figure 10.5: The p-^{12}C analysing power measured out to large scattering angles [98].

10.1.3 Contamination From Other Reaction Channels

Meson photoproduction off the proton produces a variety of final states, as seen in Figure 10.6, where the total cross-sections of several reaction channels have been plotted. To estimate the level of contamination from these competing reactions in the event sample, 20 million events were generated for each background channel and passed through the Geant4 simulation of the experiment. The simulated events were then analysed with the full polarimeter analysis code, and the number of events passing all selection cuts was compared to the yield obtained from 20 million $p\pi^0$ (or $p\eta$) events. The yields for each background reaction were then scaled by the ratio of the cross-sections to provide a realistic estimate of their contribution to the experimental data.

The most significant background reactions to consider for the $p\pi^0$ event sample are $p\pi^0\pi^0$ and $n\pi^+\pi^0$. The scaled yield from $\pi^0\pi^0$ constituted a background

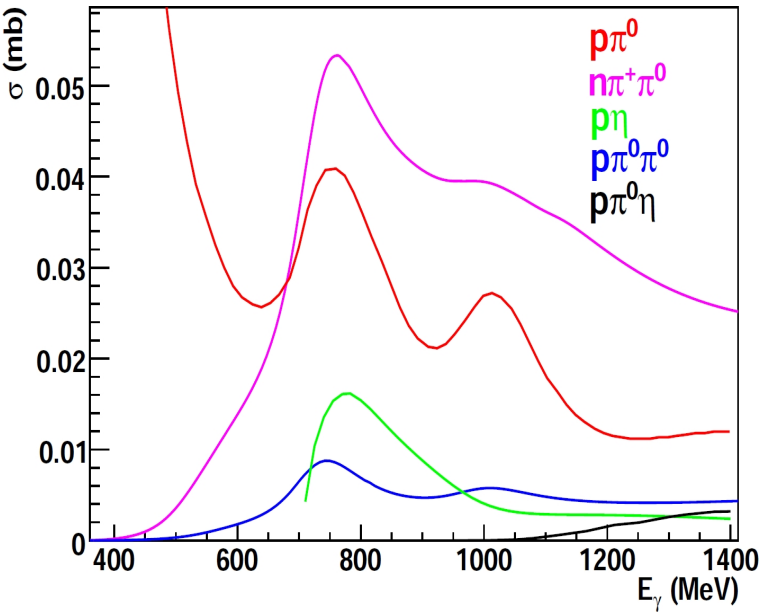

Figure 10.6: The total cross-sections of the relevant photoproduction reactions off the proton, obtained from [93, 99, 100].

of only 0.4%. The contamination from the $\gamma p \rightarrow n\pi^+\pi^0$ reaction is shown as a function of E_γ in Figure 10.7. This ratio never exceeds 3.5% over the entire energy range, indicating the effectiveness of the reaction identification method developed for this analysis.

For η photoproduction, the $\pi^0\pi^0$ and $\pi^0\eta$ channels were investigated. Both were found to contribute <1% to the total event sample.

10.1.4 False Asymmetries Check

Asymmetry measurements must distinguish between asymmetries resulting from the physical mechanism of interest and 'false' asymmetries arising from the instrumentation or mismatches between the experimental setup and the Geant4 simulation. There are two principal sources of potential false asymmetries in the present data. First, an offset in the central axis of the polarimeter away from z=0 will affect the calculation of ϕ_{sc} and distort the asymmetries. Second, the method of extracting C_x by division of a simulated beam helicity asymmetry is sensitive to discrepancies in the ϕ acceptances of the polarimeter and detectors between the simulation and data.

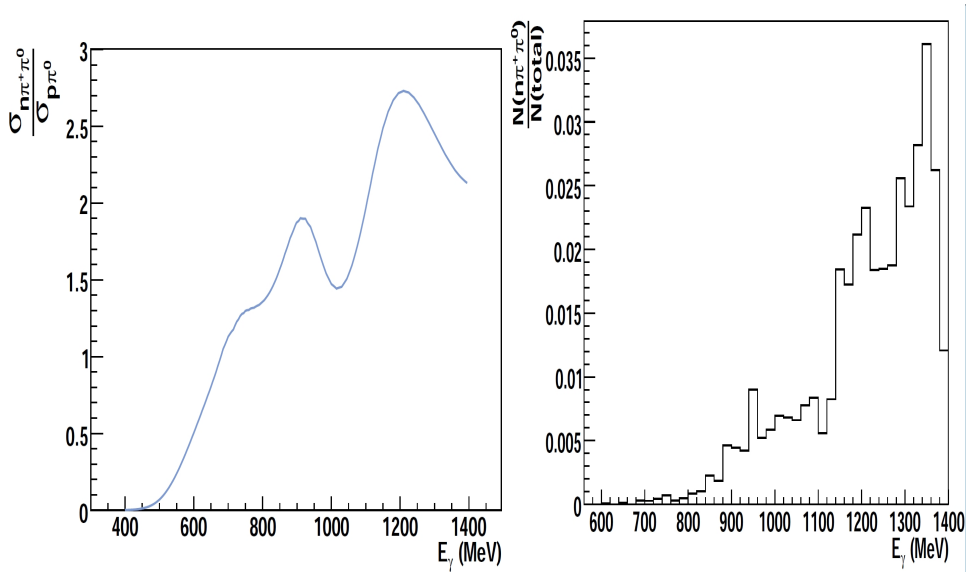

Figure 10.7: On the left, the ratio of the $\gamma p \rightarrow n\pi^+\pi^0$ and $\gamma p \rightarrow p\pi^0$ total cross-sections is shown as a function of E_γ. The plot on the right shows the fraction of accepted $n\pi^+\pi^0$ events in the total event sample, as determined by the simulation.

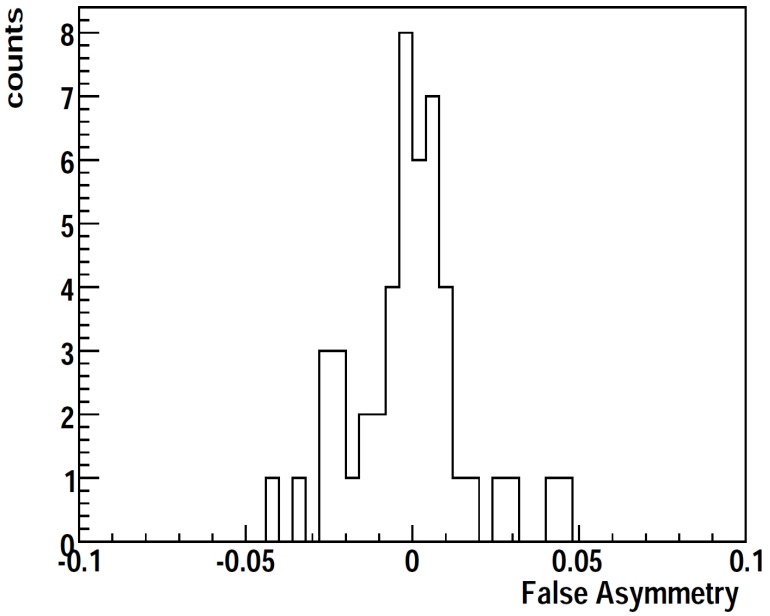

Figure 10.8: Histogram of the measured false asymmetries.

The contribution to the measured beam helicity asymmetries from these effects was quantified by randomly assigning the helicity to each event in the accepted sample of nuclear scatters for both full and empty target data, but not for simulated data. To improve the statistical accuracy, this was repeated 150 times, using a new seed for the random number generator for each iteration. The photon beam polarisation, analysing power, and P were determined and used to extract C_x as described previously in Sections 9.2-9.5. A histogram of the measured false asymmetries is displayed in Figure 10.8. All values are consistent with zero and are below the level of the systematic uncertainty.

10.2 Results

The values of C_x obtained for the $\gamma p \rightarrow p\pi^0$ reaction are shown as a function of photon beam energy E_γ in 6 bins of centre of mass angle θ_{CM} in Figures 10.9-10.11. The results are also displayed as a function of θ_{CM} for different E_γ bins in Figures 10.12-10.16. The existing C_x measurements from Jefferson Lab (orange squares), described in Chapter 4, are overlaid for comparison, as are the current solutions from both the MAID07 (red) and SAID09 (blue) partial wave analyses. Note that the Jefferson Lab measurements were reported in a polarimeter reference frame with the x-axis defined in the opposite direction, so that the sign of these points has been switched for comparison to the current data.

The $1/E_\gamma$ dependence of the bremsstrahlung and π^0 photoproduction cross-sections increases the statistical uncertainty as E_γ increases. Events at centre of mass angles greater than 130°, corresponding to more forward going recoil protons, have the smallest reported uncertainty. This reflects the higher analysing power in this kinematic range and the greater fraction of events detected in TAPS, which has a higher angular resolution and more analysing material than events detected in the Crystal Ball.

The data points are integrated over energy bins 125 MeV wide and 10° wide bins of meson angle in the centre of mass frame. The Jefferson Lab points have been measured at definite energies and angles. Consequently, comparisons between the two data sets are sensitive to the gradient of C_x over the width of the bin. The new MAMI measurements generally agree with the existing Jefferson Lab data points within their statistical and systematic error bars. The agreement

is weakest at higher energies where the systematic uncertainty of the new data is largest.

The present data greatly expand the kinematic coverage for the worldwide data set of C_x measurements and give first measurements in regions of particular physical importance. The new data are the first measurements in the region of the poorly understood $P_{11}(1440)$ Roper resonance around E_γ ~700 MeV. For centre of mass angles in the range 80-120°, the new data clearly favor the MAID solution. Notably, the sign change at ~120° predicted by MAID is reproduced by the data. At more backward centre of mass angles, the solutions tend to converge and agree well with the data.

For E_γ <500 MeV (Figure 10.12), in the tail of the $\Delta(1232)$ resonance, the data give the first confirmation of the positive sign predicted by both partial wave analyses. From 500<E_γ <700 MeV, the C_x measurement distinguishes the positive MAID solution from the negative prediction of SAID up to ~120°. The sign change at ~125° for 600<E_γ <700 MeV predicted by MAID agrees with the present data.

In the energy region 800<E_γ <1050 MeV, C_x shows reasonable agreement with previous measurements. In the three highest beam energy bins, the data closely follow the model solutions. At the most backward centre of mass angle point for all the bins in the range 900<E_γ <1400 MeV, a larger polarisation transfer has been measured than that predicted by MAID and SAID.

There are currently no published double polarisation measurements in η photoproduction. The reaction is only expected to receive contributions from the smaller subset of I=1/2 nucleon resonances ($S_{11}(1535)$, $S_{11}(1650)$, $P_{11}(1710)$, $P_{13}(1720)$, $D_{13}(1520)$, $D_{13}(1700)$, $D_{15}(1675)$, $F_{15}(1680)$) according to MAID. Currently, the MAID and SAID partial wave analysis solutions give inconsistent expectations for C_x, even near the threshold region of the reaction. Any measurement is therefore very valuable to resolving this discrepancy.

As discussed in Section 2.3.1, polarisation observables in η photoproduction are also predicted to be particularly sensitive to a possible new narrow resonance with a mass of 1680 MeV. Inclusion of the new state is predicted to show a sharp jump in C_x at E_γ ~1000 MeV (corresponding to a system energy of 1680 MeV).

The first ever measurements of C_x in the $\gamma p \rightarrow p\eta$ reaction are shown as a function of E_γ in two centre of mass angle bins in Figure 10.17. For θ_{CM} <90

and E_γ >1000 MeV, the data provide the first evidence in support of the SAID solution for C_x. For θ_{CM} >90, a large negative asymmetry has been measured at E_γ ∼1200 MeV. Due to the stastics available in the sample of η events, the present measurement is not able to resolve any narrow structure. However, future production runs at MAMI with an experimental trigger and photon tagger configuration optimised for detecting η events could achieve the statistical accuracy necessary to set limits on the existence of this postulated narrow state.

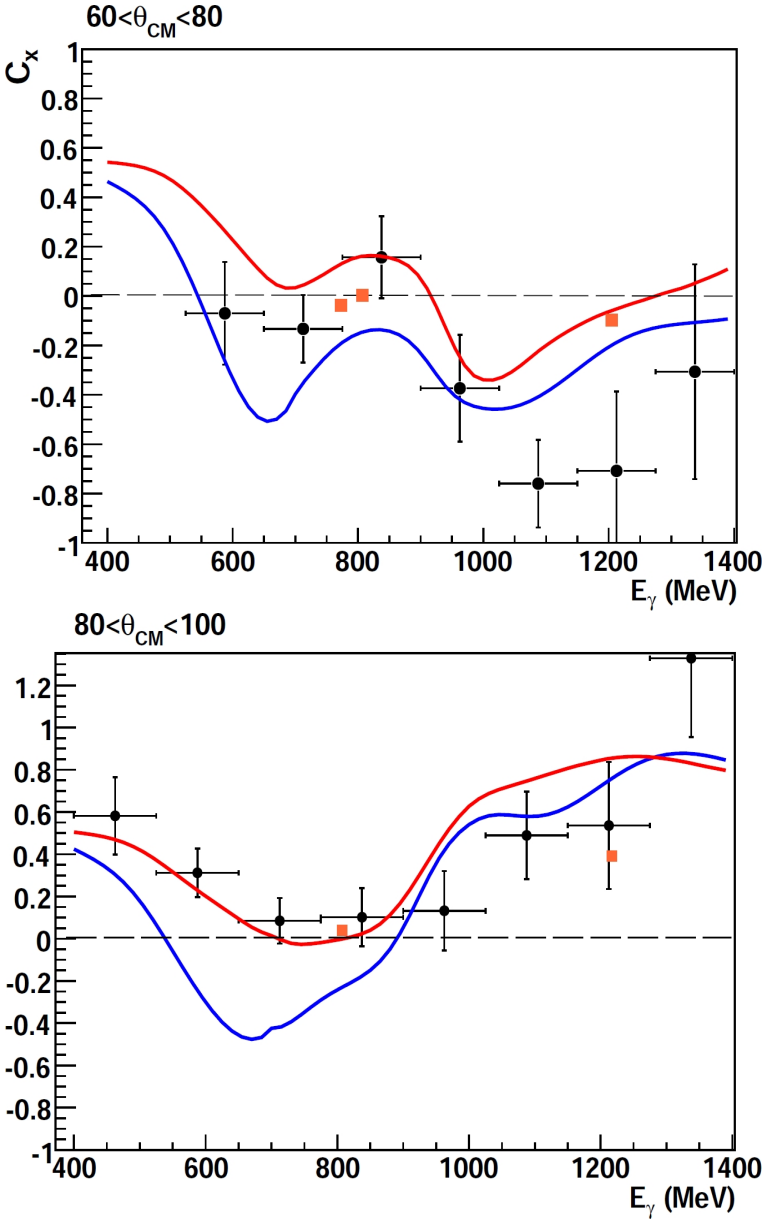

Figure 10.9: C_x as a function of E_γ for the reaction $\gamma p \rightarrow p\pi^0$ reaction for $60< \theta_{CM} <100$, compared with the MAID07 (red) and SAID09 (blue) partial wave analyses.

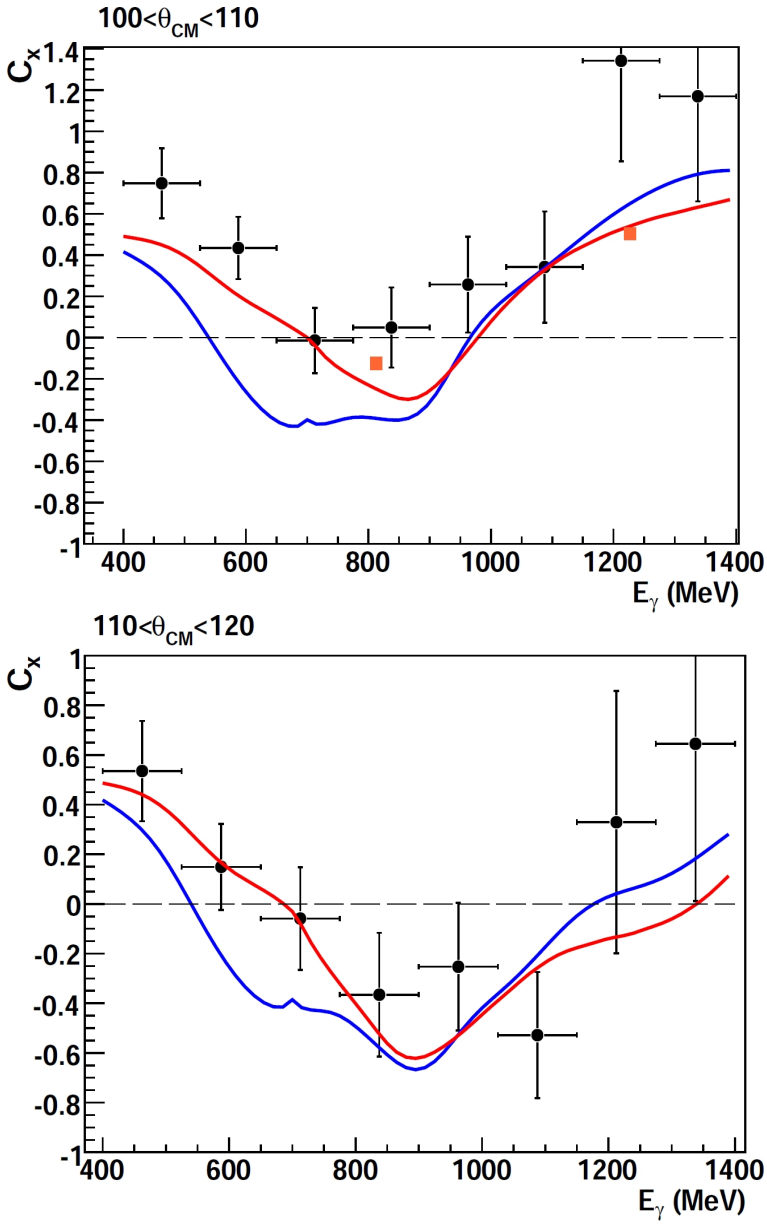

Figure 10.10: C_x as a function of E_γ for the reaction $\gamma p \rightarrow p\pi^0$ reaction for 100< θ_{CM} <120, compared with the MAID07 (red) and SAID09 (blue) partial wave analyses.

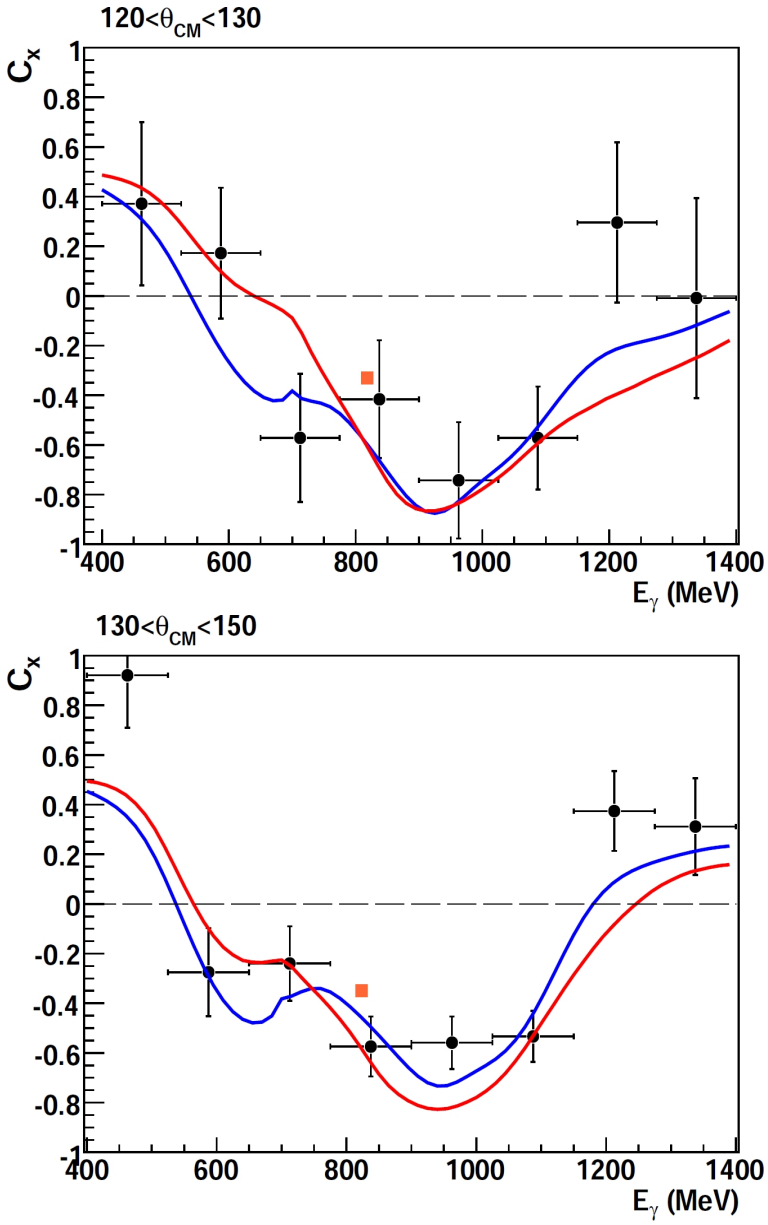

Figure 10.11: C_x as a function of E_γ for the reaction $\gamma p \rightarrow p\pi^0$ reaction for 120< θ_{CM} <150, compared with the MAID07 (red) and SAID09 (blue) partial wave analyses.

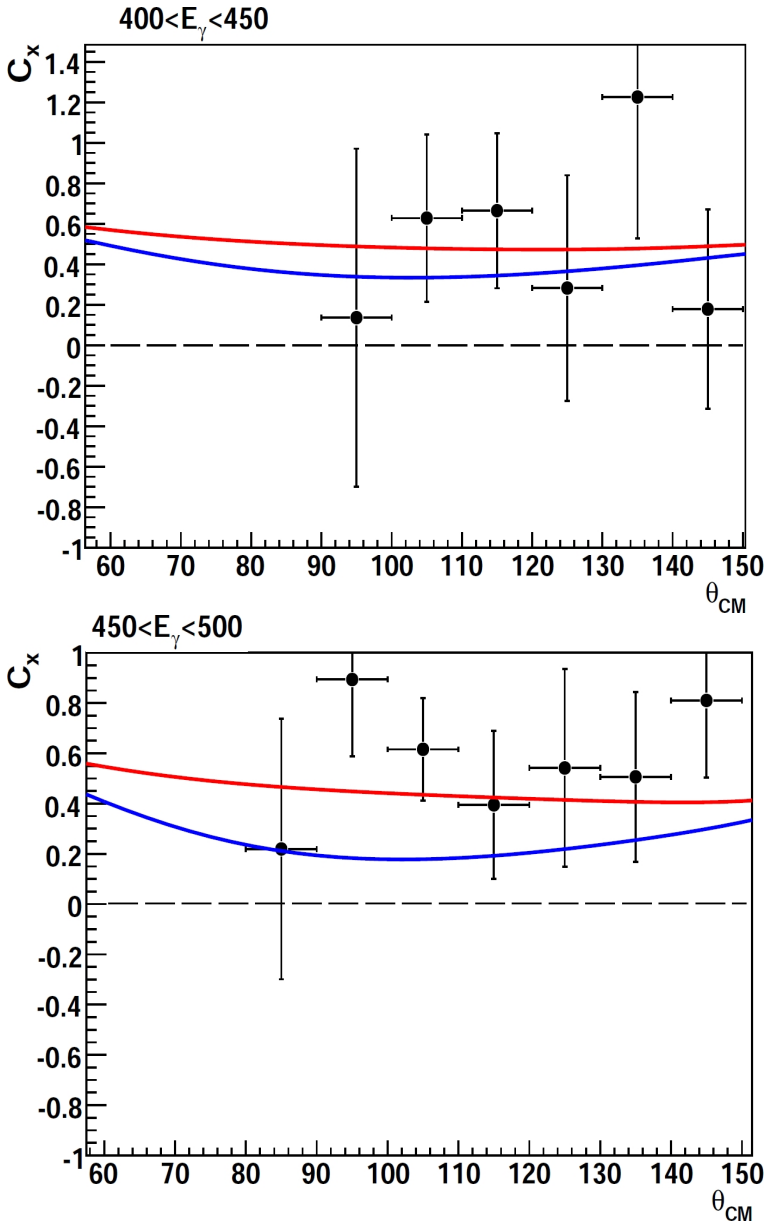

Figure 10.12: C_x as a function of θ_{CM} for the reaction $\gamma p \rightarrow p\pi^0$ reaction for $400 < E_\gamma < 500$, compared with the MAID07 (red) and SAID09 (blue) partial wave analyses.

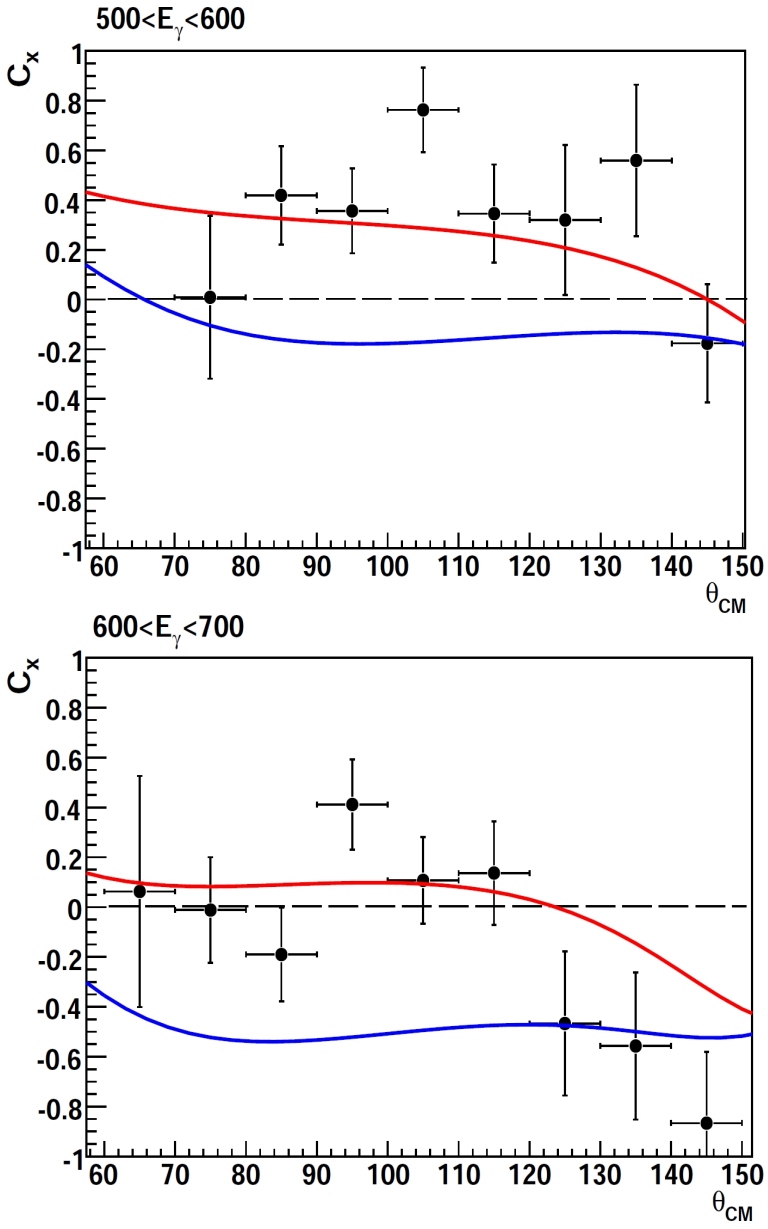

Figure 10.13: C_x as a function of θ_{CM} for the reaction $\gamma p \rightarrow p\pi^0$ reaction for $500 < E_\gamma < 700$, compared with the MAID07 (red) and SAID09 (blue) partial wave analyses.

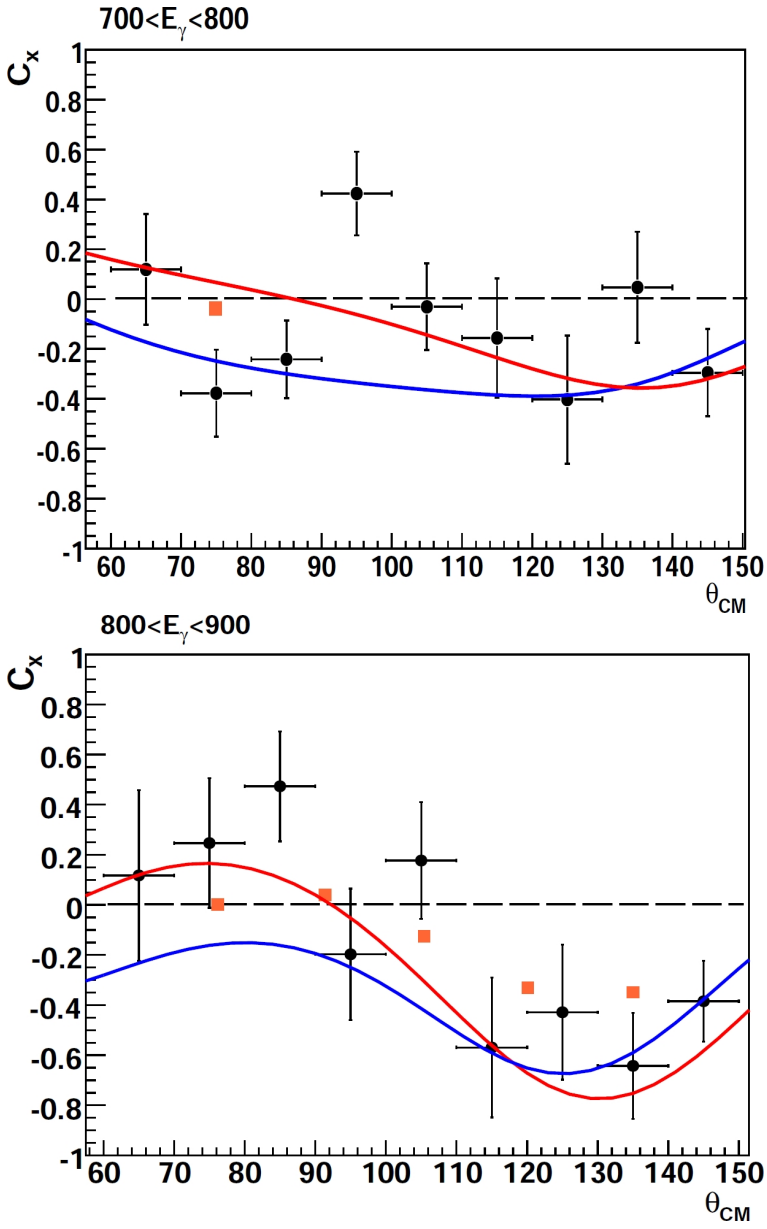

Figure 10.14: C_x as a function of θ_{CM} for the reaction $\gamma p \rightarrow p\pi^0$ reaction for $700 < E_\gamma < 900$, compared with the MAID07 (red) and SAID09 (blue) partial wave analyses.

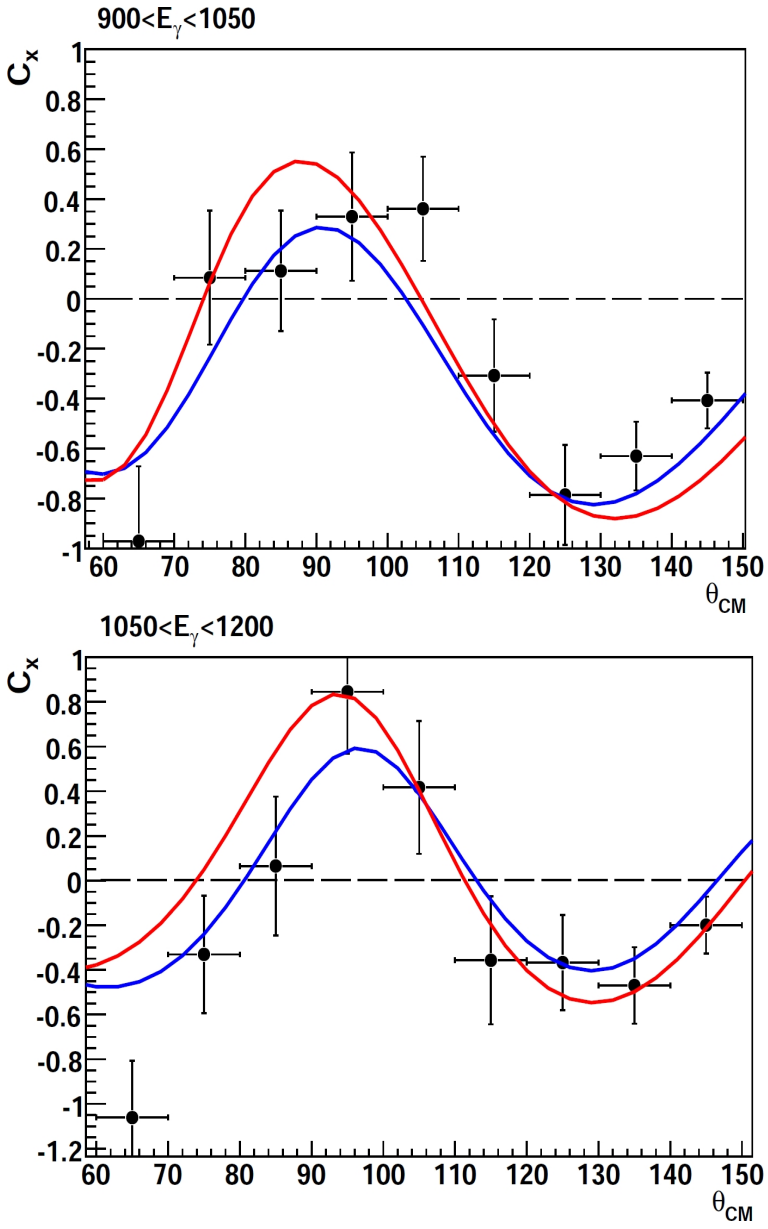

Figure 10.15: C_x as a function of θ_{CM} for the reaction $\gamma p \rightarrow p\pi^0$ reaction for $900 < E_\gamma < 1200$, compared with the MAID07 (red) and SAID09 (blue) partial wave analyses.

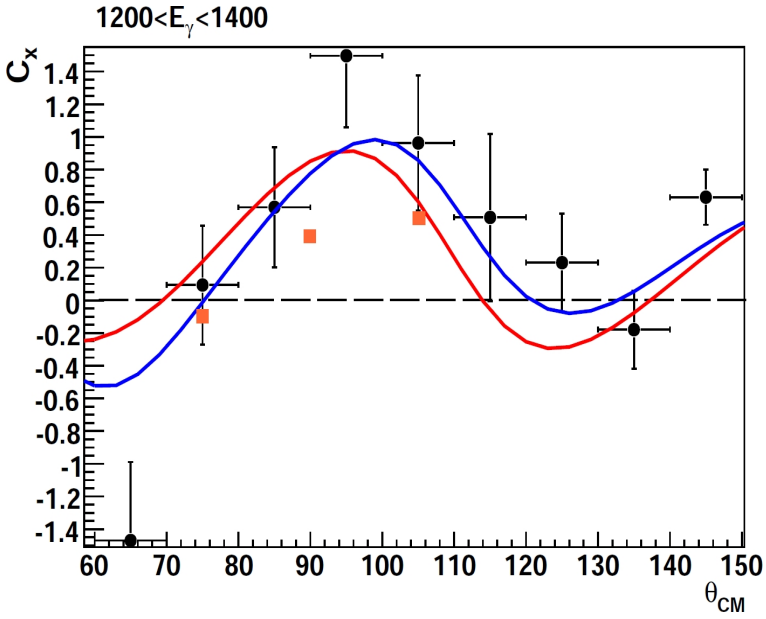

Figure 10.16: C_x as a function of θ_{CM} for the reaction $\gamma p \rightarrow p\pi^0$ reaction for $1200 < E_\gamma < 1400$, compared with the MAID07 (red) and SAID09 (blue) partial wave analyses.

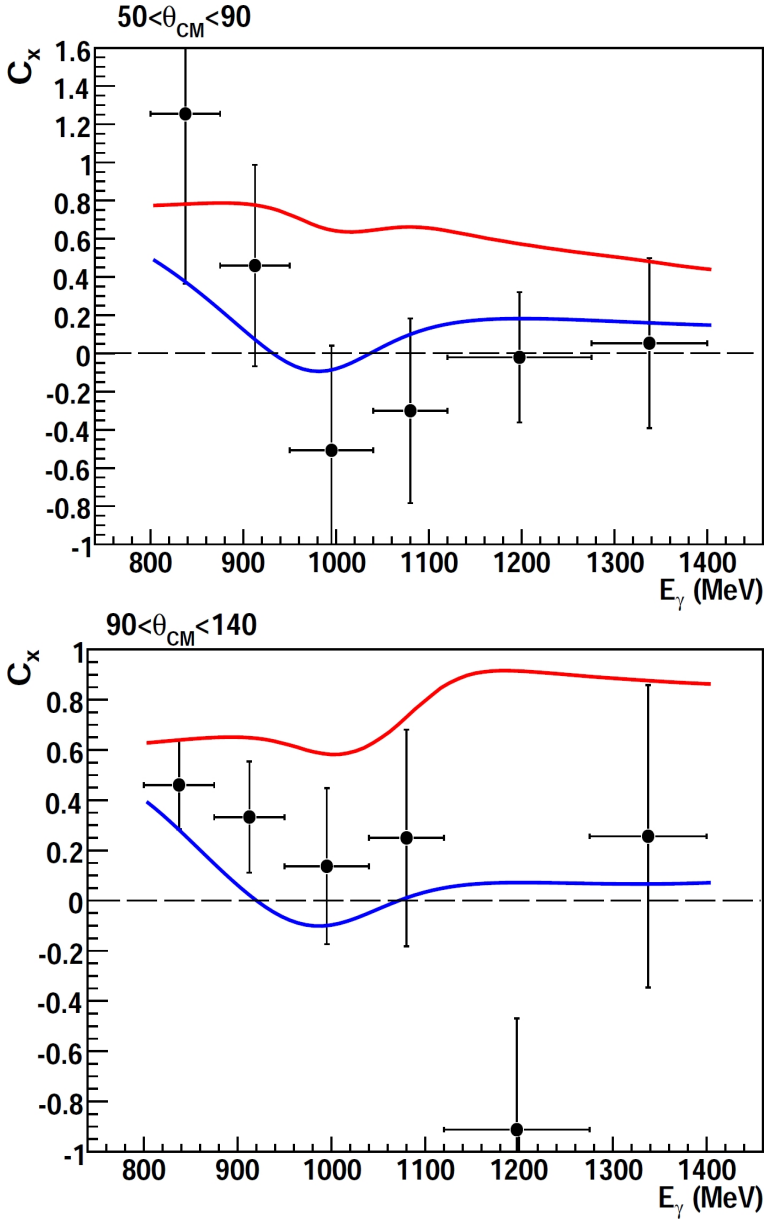

Figure 10.17: C_x as a function of E_γ for the reaction $\gamma p \rightarrow p\eta$ reaction for $50< \theta_{CM} <140$, compared with the MAID07 (red) and SAID09 (blue) partial wave analyses.

Chapter 11

Conclusions

The beam-recoil observable C_x has been measured in the reaction $\gamma p \rightarrow p\pi^0$ for photon energies between 400-1400 MeV, greatly expanding the kinematic coverage of the world data set and providing the first measurement of this observable in the region of the important $P_{11}(1440)$ Roper resonance. The data obtained at MAMI are in broad agreement with the few existing measurements from Jefferson Lab and differentiate between the leading partial wave analyses MAID and SAID. The new data strongly support the former model for the π^0 reaction in this kinematic regime, with χ^2 values of 1.09 and 2.36 per data point respectively [101]. Incorporation of the new data into the SAID database is underway and will lead to modification of the properties of the resonances extracted from this partial wave analysis model. In the future, this data will be used by the wider community of partial wave analyses, including dynamical and coupled channel approaches.

Additionally, a first measurement of C_x has been made in η photoproduction from a proton target. This will be the first published measurement of a double polarisation observable in η photoproduction. The higher energy results favor the current SAID solution, resolving a long standing discrepancy in the predictions of the two most widely used partial wave analyses. The available statistics are insufficient to distinguish a theorised narrow resonance, although the potential to investigate the existence of such a state in future measurements is established. This double polarisation data will provide the first constraints on the phases of the 4 reaction amplitudes for η production and will be an important constraint included in all future partial wave analyses.

This work has proven the concept of large acceptance recoil polarimetry using

segmented calorimeters. The ability to calculate an effective analysing power and to select a sufficiently clean event sample has been established. The next phase in the development of the polarimeter at MAMI has already been rated A by the PAC and will include wire chambers outwith the analysing material. In addition to increasing the scattering angle resolution by providing tracking information, the new setup will enable analysis of recoil neutron polarisation via charge exchange reactions.

The data base of polarisation observables is poised to expand at a rapid rate in the coming years. Nucleon targets with both longitudinal and transverse polarisation have recently become operational at Mainz, Bonn, and Jefferson Lab, allowing access to beam-target polarisation observables. The first results from these experiments are just being published, and a complete or nearly complete set of observables will soon be available for a range of meson photoproduction channels, enabling a model independent analysis of the reaction amplitudes. The current beam-recoil data and future measurements made possible by this pioneering study are a pre-requisite to achieve this. The energy upgrade at Jefferson Lab to photon energies of 12 GeV in the next few years will also offer new opportunities to extend the study of the nucleon resonance spectrum.

Experimental advances in the field of meson photoproduction coincide with the ever improving accuracy achieved by *ab initio* calculations of the nucleon excitation spectrum using lattice QCD. The measurement of polarization observables will continue to play an essential role in the effort to understand the excitation spectrum of the nucleon and thereby establish QCD as the correct theory to describe the confinement processes occuring in bound systems of light quarks.

Appendix A

Group Theory

A *group* is a set G with a binary operation * satisfying the following properties:

- Closure: if $x, y \in G$, then $x * y \in G$
- Identity element: $\exists e \in G$ such that $\forall x \in G$, $e * x = x * e = x$
- Inverse: , $\exists x^{-1} \in G$ such that $x * x^{-1} = x^{-1} * x = e$
- Associativity: , $y, z \in G$, $(x * y) * z = x * (y * z)$

Furthermore, (G,*) is *Abelian* if $\in G$ $x*y = y*x$. Otherwise, it is non-Abelian.

For a subset $S \subseteq G$, $< S >$ is the set of all elements of G which are finite products of the elements of S and their inverses. If the elements of S are linearly independent and $< S >= G$, then the elements of S are the *generators* of G.

A transformation group of a quantum mechanical system maps the members of a group to a set of unitary operators

$$x \rightarrow U(x)$$

where x and $U(x)$ is a unitary operator. If the group operations are preserved after the mapping,

$$\forall x, y,\ U(x) * U(y) = U(x * y)$$

the mapping is called a *representation*. As an example, consider the set of integers with the operation of addition. Then the mapping

$$U(n) = e^{in\theta}$$

is a representation of the group, since for integers x, y

$$e^{ix\theta} * e^{iy\theta} = e^{i(x+y)\theta}$$

In physics applications, representations are usually viewed as matrices.

A square matrix U is unitary if

$$UU^* = I$$

where U^* is the conjugate transpose of U. If, in addition, det$U$=1, then U is called a special unitary matrix. The groups SU(n) of $n \times n$ unitary matrices with the operation of matrix multiplication, play an important role in physics. These are examples of *Lie groups*, where all the elements of the group are characterised by a set of parameters a_α in terms of the N=n^2-1 generators L_α by

$$U = e^{iH} = 1 + iH - \frac{1}{2!}H^2 + ..., \qquad H = \sum_{\alpha=1}^{N} a_\alpha L_\alpha$$

For SU(2), the generators are the Pauli matrices

$$\sigma_1 = \tfrac{1}{2}\begin{pmatrix} 0 & 1 \\ 1 & 0 \end{pmatrix}$$
$$\sigma_2 = \tfrac{1}{2}\begin{pmatrix} 0 & -i \\ i & 0 \end{pmatrix}$$
$$\sigma_3 = \tfrac{1}{2}\begin{pmatrix} 1 & 0 \\ 0 & 1 \end{pmatrix}$$

The generators of SU(3) are the Gell-Mann matrices

$$\lambda_1 = \begin{pmatrix} 0 & 1 & 0 \\ 1 & 0 & 0 \\ 0 & 0 & 0 \end{pmatrix} \qquad \lambda_2 = \begin{pmatrix} 0 & -i & 0 \\ i & 0 & 0 \\ 0 & 0 & 0 \end{pmatrix} \qquad \lambda_3 = \begin{pmatrix} 1 & 0 & 0 \\ 0 & -1 & 0 \\ 0 & 0 & 0 \end{pmatrix}$$
$$\lambda_4 = \begin{pmatrix} 0 & 0 & 1 \\ 0 & 0 & 0 \\ 1 & 0 & 0 \end{pmatrix} \qquad \lambda_5 = \begin{pmatrix} 0 & 0 & -i \\ 0 & 0 & 0 \\ i & 0 & 0 \end{pmatrix} \qquad \lambda_6 = \begin{pmatrix} 0 & 0 & 0 \\ 0 & 0 & 1 \\ 0 & 1 & 0 \end{pmatrix}$$
$$\lambda_7 = \begin{pmatrix} 0 & 0 & 0 \\ 0 & 0 & -i \\ 0 & i & 0 \end{pmatrix} \qquad \lambda_8 = \tfrac{1}{\sqrt{3}}\begin{pmatrix} 1 & 0 & 0 \\ 0 & 1 & 0 \\ 0 & 0 & -2 \end{pmatrix}$$

The commutation relations between the generators

$$[L_i, L_j] = iC_{ijk}L_k$$

where C_{ijk} are structure constants, given by all cyclic permutations of

$$[L_i, [L_j, L_k]] = 0$$

define the algebra of the group. To illustrate how representations of SU(n) are constructed, consider the familiar case of SU(2) which describes the intrinsic spin of a particle. The objective is to find the hermitian representation matrices $\overrightarrow{s}$=(s_1,s_2,s_3) that satisfy

$$[s_i, s_j] = i\epsilon_{ijk}s_k, \qquad \epsilon_{ijk} = \begin{cases} 1, \text{ if } (i,j,k) \text{ is } (1,2,3),(3,1,2),(2,3,1) \\ -1, \text{ if } (i,j,k) \text{ is } (1,3,2),(3,2,1),(2,1,3) \\ 0, \text{ otherwise} \end{cases}$$

For a spin-0 particle, the representation is trivial: $s_i = s_j = s_k$=[0]. The simplest non-trivial, or *fundamental*, representation of SU(2) is the 2-dimensional case of a spin-1/2 particle. There are two basis states

$$|s=1/2,m=1/2> = \begin{pmatrix} 1 \\ 0 \end{pmatrix}, \qquad |s=1/2, m=-1/2> = \begin{pmatrix} 0 \\ 1 \end{pmatrix}$$

corresponding to spin-up and spin-down states. The representation matrices are then the Pauli matrices, the generators of the group. They are expressed as

$$s_z = \begin{pmatrix} 1/2 & 0 \\ 0 & 1/2 \end{pmatrix}$$
$$s_+ = \begin{pmatrix} 0 & 1 \\ 0 & 0 \end{pmatrix}$$
$$s_- = \begin{pmatrix} 0 & 0 \\ 1 & 0 \end{pmatrix}$$

where the raising and lowering operators

$$s_\pm = s_x \pm i s_y$$

have been defined, and particles can be labeled as eigenstates of the diagonal generator s_z. Higher spin particles are described by higher dimensional representations of SU(2). The representation matrices of the 3-dimensional spin-1 system, with basis states

$$|s=1,m=1> = \begin{pmatrix} 1 \\ 0 \\ 0 \end{pmatrix}, \qquad |s=1,m=0> = \begin{pmatrix} 0 \\ 1 \\ 0 \end{pmatrix}, \qquad |s=1,m=-1> = \begin{pmatrix} 0 \\ 0 \\ 1 \end{pmatrix}$$

corresponding to spin projections of m_z=1,0, and -1 respectively, are

$$s_z = \begin{pmatrix} 1 & 0 & 0 \\ 0 & 0 & 0 \\ 0 & 0 & -1 \end{pmatrix}$$
$$s_+ = \begin{pmatrix} 0 & \sqrt{2} & 0 \\ 0 & 0 & \sqrt{2} \\ 0 & 0 & 0 \end{pmatrix}$$
$$s_- = \begin{pmatrix} 0 & 0 & 0 \\ \sqrt{2} & 0 & 0 \\ 0 & \sqrt{2} & 0 \end{pmatrix}$$

Higher dimensional representations are built from the fundamental representation using direct products. Two spin-1/2 particles, combined in the direct product

$$\mathbf{2} \times \mathbf{2} = 3 + 1$$

produce the s=1 triplet described above as well as the s=0 singlet state. Higher occupancy spin multiplets are formed by taking direct products of multiple spin-1/2 particles.

Appendix B

Tabulated Results

The C_x data points for π^0 photoproduction are given in Table B.1 as a function of E_γ and in Table B.2 as a function of θ_{CM}.

The C_x data points for η photoproduction are given in Table B.3 as a function of E_γ.

Table B.1: C_x data points as a function of E_γ for the $\gamma p \rightarrow p\pi^0$ reaction.

θ_{CM}	E_γ (MeV)	C_x	$\sigma_{stat.}$	$\sigma_{syst.}$
60-80	525-650	-0.070	0.208	0.113
60-80	650-775	-0.133	0.137	0.049
60-80	775-900	0.157	0.166	0.109
60-80	900-1025	-0.374	0.216	0.147
60-80	1025-1150	-0.760	0.178	0.145
60-80	1150-1275	-0.708	0.322	0.240
60-80	1275-1400	-0.306	0.435	0.240
80-100	400-525	0.582	0.183	0.124
80-100	525-650	0.312	0.116	0.113
80-100	650-775	0.085	0.108	0.049
80-100	775-900	0.102	0.138	0.109
80-100	900-1025	0.132	0.188	0.147
80-100	1025-1150	0.489	0.208	0.145

Continued on next page

Table B.1 – continued from previous page

θ_{CM}	E_γ (MeV)	C_x	$\sigma_{stat.}$	$\sigma_{syst.}$
80-100	1150-1275	0.536	0.301	0.240
80-100	1150-1275	1.328	0.373	0.240
100-110	400-525	0.748	0.170	0.124
100-110	525-650	0.434	0.150	0.113
100-110	650-775	-0.014	0.158	0.049
100-110	775-900	0.049	0.194	0.109
100-110	900-1025	0.257	0.233	0.147
100-110	1025-1150	0.342	0.269	0.145
100-110	1150-1275	1.342	0.488	0.240
100-110	1275-1400	1.170	0.510	0.240
110-120	400-525	0.535	0.202	0.124
110-120	525-650	0.149	0.173	0.113
110-120	650-775	-0.059	0.207	0.049
110-120	775-900	-0.366	0.249	0.109
110-120	900-1025	-0.253	0.257	0.147
110-120	1025-1150	-0.528	0.254	0.145
110-120	1150-1275	0.329	0.528	0.240
110-120	1275-1400	0.645	0.633	0.240
120-130	400-525	0.371	0.329	0.124
120-130	525-650	0.172	0.264	0.113
120-130	650-775	-0.571	0.258	0.049
120-130	775-900	-0.416	0.237	0.109
120-130	900-1025	-0.742	0.234	0.147
120-130	1025-1150	-0.572	0.208	0.145
120-130	1150-1275	0.295	0.323	0.240
120-130	1275-1400	0.009	0.403	0.240
130-150	400-525	0.920	0.211	0.124
130-150	525-650	-0.275	0.177	0.113

Continued on next page

Table B.1 – continued from previous page

θ_{CM}	E_γ (MeV)	C_x	$\sigma_{stat.}$	$\sigma_{syst.}$
130-150	650-775	-0.240	0.150	0.049
130-150	775-900	-0.574	0.121	0.109
130-150	900-1025	-0.559	0.106	0.147
130-150	1025-1150	-0.533	0.103	0.145
130-150	1150-1275	0.374	0.160	0.240
130-150	1275-1400	0.311	0.195	0.240

Table B.2: C_x as a function of θ_{CM} data points for the $\gamma p \rightarrow p\pi^0$ reaction.

E_γ (MeV)	θ_{CM}	C_x	$\sigma_{stat.}$	$\sigma_{syst.}$
400-450	90-100	0.136	0.835	0.084
400-450	100-110	0.628	0.414	0.084
400-450	110-120	0.665	0.383	0.084
400-450	120-130	0.282	0.557	0.084
400-450	130-140	1.226	0.699	0.084
400-450	140-150	0.178	0.492	0.084
450-500	80-90	0.219	0.519	0.124
450-500	90-100	0.894	0.306	0.124
450-500	100-110	0.616	0.204	0.124
450-500	110-120	0.395	0.295	0.124
450-500	120-130	0.542	0.393	0.124
450-500	130-140	0.506	0.338	0.124
450-500	140-150	0.810	0.308	0.124
500-600	70-80	0.009	0.328	0.113
500-600	80-90	0.419	0.197	0.113
500-600	90-100	0.356	0.171	0.113
500-600	100-110	0.763	0.170	0.113
500-600	110-120	0.346	0.198	0.113

Continued on next page

Table B.2 – continued from previous page

E_γ (MeV)	θ_{CM}	C_x	$\sigma_{stat.}$	$\sigma_{syst.}$
500-600	120-130	0.320	0.302	0.113
500-600	130-140	0.559	0.305	0.113
500-600	140-150	-0.176	0.238	0.113
600-700	60-70	0.063	0.463	0.036
600-700	70-80	-0.012	0.212	0.036
600-700	80-90	-0.190	0.188	0.036
600-700	90-100	0.412	0.181	0.036
600-700	100-110	0.107	0.173	0.036
600-700	110-120	0.137	0.207	0.036
600-700	120-130	-0.467	0.289	0.036
600-700	130-140	-0.557	0.296	0.036
600-700	140-150	-0.867	0.287	0.036
700-800	60-70	0.119	0.222	0.049
700-800	70-80	-0.377	0.174	0.049
700-800	80-90	-0.241	0.155	0.049
700-800	90-100	0.423	0.168	0.049
700-800	100-110	-0.031	0.174	0.049
700-800	110-120	-0.156	0.239	0.049
700-800	120-130	-0.403	0.257	0.049
700-800	130-140	0.047	0.223	0.049
700-800	140-150	0.295	0.175	0.049
800-900	60-70	0.118	0.340	0.109
800-900	70-80	0.247	0.259	0.109
800-900	80-90	0.473	0.219	0.109
800-900	90-100	-0.197	0.262	0.109
800-900	100-110	0.177	0.233	0.109
800-900	110-120	-0.569	0.279	0.109
800-900	120-130	-0.429	0.269	0.109

Continued on next page

Table B.2 – continued from previous page

E_γ (MeV)	θ_{CM}	C_x	$\sigma_{stat.}$	$\sigma_{syst.}$
800-900	130-140	-0.643	0.211	0.109
800-900	140-150	-0.385	0.162	0.109
900-1050	60-70	-0.971	0.300	0.147
900-1050	70-80	0.084	0.268	0.147
900-1050	80-90	0.111	0.242	0.147
900-1050	90-100	0.329	0.257	0.147
900-1050	100-110	0.361	0.209	0.147
900-1050	110-120	-0.308	0.225	0.147
900-1050	120-130	-0.786	0.200	0.147
900-1050	130-140	-0.630	0.138	0.147
900-1050	140-150	-0.408	0.112	0.147
1050-1200	60-70	-1.061	0.254	0.145
1050-1200	70-80	-0.331	0.262	0.145
1050-1200	80-90	0.065	0.311	0.145
1050-1200	90-100	0.845	0.277	0.145
1050-1200	100-110	0.417	0.297	0.145
1050-1200	110-120	0.357	0.286	0.145
1050-1200	120-130	0.367	0.212	0.145
1050-1200	130-140	0.470	0.171	0.145
1050-1200	140-150	0.200	0.127	0.145
1200-1400	60-70	-1.469	0.480	0.240
1200-1400	70-80	0.094	0.363	0.240
1200-1400	80-90	0.569	0.366	0.240
1200-1400	90-100	1.497	0.438	0.240
1200-1400	100-110	0.963	0.413	0.240
1200-1400	110-120	0.508	0.512	0.240
1200-1400	120-130	0.231	0.299	0.240
1200-1400	130-140	-0.179	0.238	0.240

Continued on next page

Table B.2 – continued from previous page

E_γ (MeV)	θ_{CM}	C_x	$\sigma_{stat.}$	$\sigma_{syst.}$
1200-1400	140-150	0.631	0.169	0.240

Table B.3: C_x as a function of E_γ data points for the $\gamma p \rightarrow p\eta$ reaction.

E_γ (MeV)	θ_{CM}	C_x	$\sigma_{stat.}$	$\sigma_{syst.}$
800-875	50-90	1.254	0.889	0.109
875-950	50-90	0.460	0.527	0.147
950-1040	50-90	-0.508	0.547	0.147
1040-1120	50-90	-0.301	0.484	0.145
1120-1275	50-90	-0.021	0.341	0.145
1275-1400	50-90	0.053	0.445	0.240
800-875	90-140	0.461	0.177	0.109
875-950	90-140	0.333	0.222	0.147
950-1040	90-140	0.137	0.311	0.147
1040-1120	90-140	0.250	0.431	0.145
1120-1275	90-140	-0.912	0.443	0.145
1275-1400	90-140	0.256	0.602	0.240

References

[1] E. Rutherford. *Philos. Mag.*, 37:581, 1919.

[2] J. Chadwick. *Nature*, 129:312, 1932.

[3] W. Hesienberg. *Zeitschrift für Physik*, 77:1–11, 1932.

[4] H. Yukawa. *Proc. Phys. Math Soc. Japan*, 17(48), 1935.

[5] D. Griffiths. *Introduction to Elementary Particles*. Wiley, USA, 1987.

[6] A. Pais. *Phys. Rev.*, 86, 1952.

[7] M. Gell-Mann. *Phys. Rev.*, 92(3):833–834, 1953.

[8] T. Nakano, K. Nishijima. *Prog. Theor. Phys.*, 10(5):581–582, 1953.

[9] M. Gell-Mann. *Report CSTL-20*, 1961.

[10] M. Gell-Mann. *Physics Letters*, 8(3), 1964.

[11] M. Breidenbach, J. I. Friedman, H. W. Kendall, E. D. Bloom, D. H. Coward, H. DeStaebler, J. Drees, L. W. Mo, and R. E. Taylor. *Phys. Rev. Lett.*, 23(16):935–939, 1969.

[12] O. W. Greenberg. *Phys. Rev. Lett.*, 13(20):598–602, 1964.

[13] J. Ashman *et. al. Nucl. Phys. B*, 328:1–35, 1989.

[14] M.S. Bhagwat, I.C. Cloët, C.D. Roberts. *arXiv:0710.2059v1 [nucl-th]*.

[15] H. David Politzer. *Phys. Rev. Lett.*, 30(26):1346–1349, 1973.

[16] David J. Gross and Frank Wilczek. *Phys. Rev. Lett.*, 30(26):1343–1346, 1973.

[17] S. Bethke. *Prog. Part. Nucl. Phys.*, 58, 2007.

[18] K.G. Wilson. *Phys. Rev. D*, 10(8):2445–2459, 1974.

[19] The Frontiers of Nuclear Science: a Long Range Plan. http://science.energy.gov/np/nsac, 2007.

[20] M. Creutz, L. Jacobs, C. Rebbi. *Phys. Rev. D*, 20(8):1915–1922, 1979.

[21] S. Dürr *et al. Nature*, 322(5905):1224–1227, 2009.

[22] O. Aharony. *arXiv:hep-th/0212193v3.*

[23] G.F. de Téramond, S.J. Brodsky. *Phys. Rev. Lett.*, 94, 2005.

[24] A.G. Williams C.D. Roberts. *Prog. Part. Nucl. Phys.*, 33:477–575, 1994.

[25] S.M. Schmidt J.C.R. Bloch, C.D. Roberts. *arXiv:nucl-th/9911068v1*, 1999.

[26] T.H.R. Skyrme. *Proceedings of the Royal Society of London*, 247(1249):260–278, 1958.

[27] G.S. Adkins, C.R. Nappi, E. Witten. *Nuclear Physics B*, 228:552–566, 1983.

[28] A. Chodos, R.L. Jaffe, K. Johnson, C.B. Thorn, V.F. Weisskopf. *Phys. Rev. D*, 9(12):3471–3495, 1974.

[29] A. Chodos, R.L. Jaffe, K. Johnson, C.B. Thorn. *Phys. Rev. D*, 10(8):2599–2604, 1974.

[30] S. Théberge, A.W. Thomas. *Phys. Rev. D*, 22(11):2838–2852, 1980.

[31] A. Watson. *The Quantum Quark.* Cambridge University Press, UK, 2004.

[32] D. Faiman, A.W. Hendry. *Phys. Rev.*, 173(5):1720–1729, 1968.

[33] N. Isgur, G. Karl. *Phys. Rev. D*, 20(5):1191–1194, 1979.

[34] G. Karl N. Isgur. *Phys. Rev. D*, 19(9):2653–2677, 1979.

[35] S. Capstick and W. Roberts. *Progress in Particle and Nuclear Physics*, 45(Supplement 2):S241 – S331, 2000.

[36] M. Anselmino, E. Predazzi, S. Ekelin, S. Fredriksson, D.B. Lichtenberg. *Rev. Mod. Phys.*, 65(4):1199–1233, 1993.

[37] E. Santopinto. *Phys. Rev. C*, 72(2):022201, 2005.

[38] Derek B. Leinweber. *Phys. Rev. D*, 47(11):5096–5103, 1993.

[39] C.P. Forsyth and R. E. Cutkosky. *Nuclear Physics B*, 178(1):35 – 44, 1981.

[40] K. Nakamura *et al. Particle Data Group*, 2010.

[41] E. Klempt, J.M. Richard. arXiv:0901.2055 [hep-ph], 2009.

[42] H. Toki A. Hosaka. *Quarks, Baryons, and Chiral Symmetry.* World Scientific, 2001.

[43] D. Diakonov, V. Petrov, M.V. Polyakov. *Zeitschrift für Physik A*, 359:305–314, 1997.

[44] F. Close. *Nature*, 435:287–288, 2005.

[45] R.A. Arndt, Y.I. Azimov, M.V. Polyakov, I.I. Strakovsky, R.L. Workman. *Phys. Rev. C*, 69(035208), 2004.

[46] I. Jaegle, *et al. Phys. Rev. Lett.*, 100(25):252002, 2008.

[47] V. Kuznetsov *et al. Physics Letters B*, 647(1):23–29, 2007.

[48] M. Polyakov V. Kuznetsov. *JETP Letters*, 88(6):347–350, 2008.

[49] S. Drell J. Bjorken. *Relativistic Quantum Mechanics.* McGraw-Hill, 1964.

[50] A. Nagl, V. Devanathan, H. Überall. *Nuclear Pion Photoproduction.* Springer-Verlag, 1991.

[51] G.F. Chew, M.L. Goldberger, F.E. Low, Y. Nambu. *Phys. Rev.*, 106(6):1345–1355, 1957.

[52] R.L. Walker. *Phys. Rev.*, 182(5):1729–1748, 1969.

[53] J.K. Storrow I.S. Barker, A. Donnachie. *Nuclear Physics B*, 79:431–460, 1974.

[54] J.K. Storrow I.S. Barker, A. Donnachie. *Nuclear Physics B*, 95:347–356, 1975.

[55] G. Shaw F. Close, S. Donnachie. *Electromagnetic Interactions and Hadronic Structure*. Cambridge University Press, 2007.

[56] L. Thiator D. Drechsel, S. Kamalov. *Eur. Phys. J. A.*, 34:69–97, 2007.

[57] D. Drechsel, O. Hanstein, S.S. Kamalov, L. Tiator. *Nuclear Physics A*, 645(1):145–174, 1999.

[58] R. Arndt, I. Strakovsky, R. Workman, M. Pavan. *Phys. Rev. C*, 52(4):2120–2130, 1995.

[59] R. Arndt, J. Ford, L. Roper. *Phys. Rev. D*, 32(5):1085–1103, 1985.

[60] K. Wijesooriya *et. al. Phys. Rev. C*, 66(034614), 2002.

[61] J. Alcorn *et. al. Nucl. Instr. Meth. A*, 522:294–346, 2004.

[62] M. McNaughton *et al. Nucl. Instr. Meth. A*, 241(2-3):435–440, 1985.

[63] H. J. Arends. *Nuclear Physics News*, 18(2):5–11, 2008.

[64] T. Walcher. *Prog. Part. Nucl. Phys.*, 34:1–15, 1995.

[65] A. Jankowiak. *Eur. Phys. J. A*, 28:149–160, 2006.

[66] M. A. D. Wilson. *IEEE PAC*, pages 71–75, 1991.

[67] B. E. Norum. *IEEE Transactions on Nuclear Science*, NS-30(4):3250–3251, August 1983.

[68] H. Berghauser, Justus-Liebig-Universität Gießen. PhD thesis, 2010.

[69] H. Herminghaus *et al. Nucl. Instrum. Methods*, 138:1–12, 1976.

[70] K. Aulenbacher *et al. Nucl. Instrum. Meth. A*, 391:498–506, 1997.

[71] S. J. Hall *et al. Nucl. Instrum. Meth. A*, 368:698–708, 1999.

[72] J. C. McGeorge, J. D. Kellie *et al. Eur. Phys. J. A*, 37:129–137, 2008.

[73] Elliot D. Bloom, Charles W. Peck. *Annu. Rev. Nucl. Sci*, 33:143–197, 1983.

[74] M. Oreglia *et al. Phys. Rev. D*, 25(9):2259–2277, 1982.

[75] A. Starostin, B. M. K. Nefkens, *et al. Phys. Rev. C*, 64:055205, 2001.

[76] D. Watts. Crystal Ball Collaboration Meeting, Los Angeles, 2005.

[77] R. Novotny. *IEEE Transactions on Nuclear Science*, 38(2):379–385, 1991.

[78] G. Braun *et al.* arXiv:hep-ex/9810048, 1998.

[79] *et al.* P. Drexler, U. Thoöring. *IEEE Transactions on Nuclear Science*, 50(4):969–973, August 2003.

[80] S. Agostinelli *et al. Nucl. Instr. Meth. A*, 506(3):250–303, 2003.

[81] M. Unverzagt, The University of Mainz. PhD thesis, 2008.

[82] J. Brudvik, The University of California, Los Angeles. PhD thesis, 2007.

[83] R. Wiringa, R. Smith, T. Ainsworth. *Phys. Rev. C*, 29(4):1207–1221, 1984.

[84] R. Wiringa, V. Stoks, R. Schiavilla. *Phys. Rev. C*, 51(1):38–51, 1995.

[85] K. Krane. *Introductory Nuclear Physics.* John Wiley and Sons, 1988.

[86] L. Wolfenstein. *Annu. Rev. Nucl. Sci.*, 6:43–76, 1956.

[87] J. Ashkin L. Wolfenstein. *Phys. Rev.*, 85(6):947–949, 1952.

[88] E. Aprile-Giboni *et al. Nucl. Instr. Meth. A*, 215:147–157, 1983.

[89] G. Waters *et al. Nucl. Instr. Meth. A*, 153:401–408, 1978.

[90] J. Glister *et al. Nucl. Instr. Meth. A*, 606(3):578–584, 2009.

[91] R. Ransome *et al. Nucl. Instr. Meth. A*, 201:315–321, 1982.

[92] M. McNaughton. *Los Alamos National Laboratory Report*, LA-8307-MS, 1980.

[93] http://gwdac.phys.gwu.edu/.

[94] D. Howdle. Private communication, 2011.

[95] V. Tioukine, K. Aulenbacher, E. Riehn. *Review of Scientific Instruments*, 82:033303, 2011.

[96] J.W. Motz *et.al. Rev. Mod. Phys.*, 36(4):881–928, 1964.

[97] T. Wakasa, Y. Hagihara, M. Sasano *et. al. Nucl. Instr. Meth. A*, 547(2-3):569–582, 2005.

[98] T. Pospischil *et. al. Nucl. Instr. Meth. A*, 483(3):713 – 725, 2002.

[99] V. Kashevarov *et. al. The European Physical Journal A - Hadrons and Nuclei*, 42:141–149, 2009.

[100] http://wwwkph.kph.uni-mainz.de/MAID//twopion/.

[101] I. Strakovsky. Private communication, 2011.